Section 5

Development of and studies with regional and smaller-scale atmospheric models, regional ensemble forecasting

Verification of mesoscale forecasts by a high resolution non-hydrostatic model at JMA

Kohei Aranami and Tomonori Segawa
Numerical Prediction Division, 1-3-4 Otemachi, Chiyoda-ku, Tokyo 100-8122, Japan
E-mail: aranami@met.kishou.go.jp, t-segawa@met.kishou.go.jp

1 Introduction

Japan Meteorological Agency (JMA) started operating a mesoscale numerical weather prediction system for disaster prevention in March 2001 using a hydrostatic model (MSM) with a horizontal resolution 10 km. A non-hydrostatic model (JMANHM, Saito et al., 2006, hereafter 10km-NHM) has been operating since September 2004 with the same horizontal resolution. The horizontal resolution is planned to be enhanced to 5 km (5km-NHM) in March 2006 on the new computer system of JMA.

2 Specifications of 5km-NHM

In this section, the specifications which are changed from 10km-NHM are described. See Satio et al.(2006) in detail for the specifications of 10km-NHM. For both 10km-NHM and 5km-NHM, initial and boundary fields are prepared by the JMA mesoscale 4D-Var analysis and the JMA regional spectral model, respectively.

The forecast domain of 5km-NHM covers the Japan Islands and its surrounding areas with grid points 721 $\times$ 577, while 10km-NHM covers the same area with grid points 361 $\times$ 289. The number of vertical layers is also increased from 40 to 50. The frequency of forecast is increased from 4 times a day to 8 times a day. The forecast time is shortened from 18 hours to 15 hours.

The model topographies of 5km-NHM and 10km-NHM are made from GTOPO30 developed by the U.S Geological Survey. The surface parameters, heat capacity and albedo are changed according to land-use information.

The CFL conditions of JMANHM are usually restricted not by the horizontal wind speed but by the vertical wind speeds, therefore the time step for the 5km-NHM is reduced to be 24 seconds from 40 seconds of 10km-NHM. The strength of the fourth-order computational diffusion and the nonlinear damping are increased for stable computation even in a small and intense typhoon case.

The radiation scheme which is used in the JMA global spectral model was implemented. The treatment of the optical characteristic of clouds especially at high altitudes is refined by using this scheme.

The intensity of the turbulence outside the planetary boundary layer is reduced to be half of 10km-NHM. The horizontal mixing length is reduced to the same value of that of vertical.

The Kessler-type conversion threshold from convective condensate to precipitation is increased and life times of deep and shallow convection are changed in the Kain Fritsch cumulus parameterization scheme (Kain and Fritsch, 1993) that affects greatly the accuracy of precipitation forecasts.

3 Verification results

In this section, the performance of 5km-NHM is shown in terms of statistical verification scores in comparison with 10km-NHM for the period of June to July in 2004 and January to February in 2005.

The forecasted precipitation is verified against the radar-rain gauge composite precipitation data. The verifications are carried out for every 20 km square mesh over land and over sea near the coast. Figure 1 shows the bias and threat scores for three hour precipitation by 5km-NHM and 10km-NHM. The threat scores of 5km-NHM are better than those of 10km-NHM at all threshold in summer, while they are almost comparable in winter. The bias scores of 5km-NHM are much improved to be almost flat.

Figure 2 shows the mean errors of the surface temperature and surface wind by 5km-NHM and 10km-NHM against the data collected by a mesonetwork of JMA. The number of observation points which are used for verifications is about 1000 points. The mean errors of surface temperature and surface wind are reduced in nighttime both in summer and winter by 5km-NHM.

4 Concluding Remarks

5km-NHM will be in operational use in March 2006. We are planning to extend the forecast time of this operational MSM up to 33 hours for 4 of 8 times a day in 2007. It is also planned to develop a high resolution mesoscale mode with grid spacing around 2 km for the aviation weather forecast and the urban weather forecast. Furthers developments of dynamical and physical process are continued.

References

[1] Saito, K., T. Fujita, Y. Yamada, J. Ishida, Y. Kumagai, K. Aranami, S. Ohomori, R. Nagasawa, S. Kumagai, C. Muroi, T. Kato, H. Eito

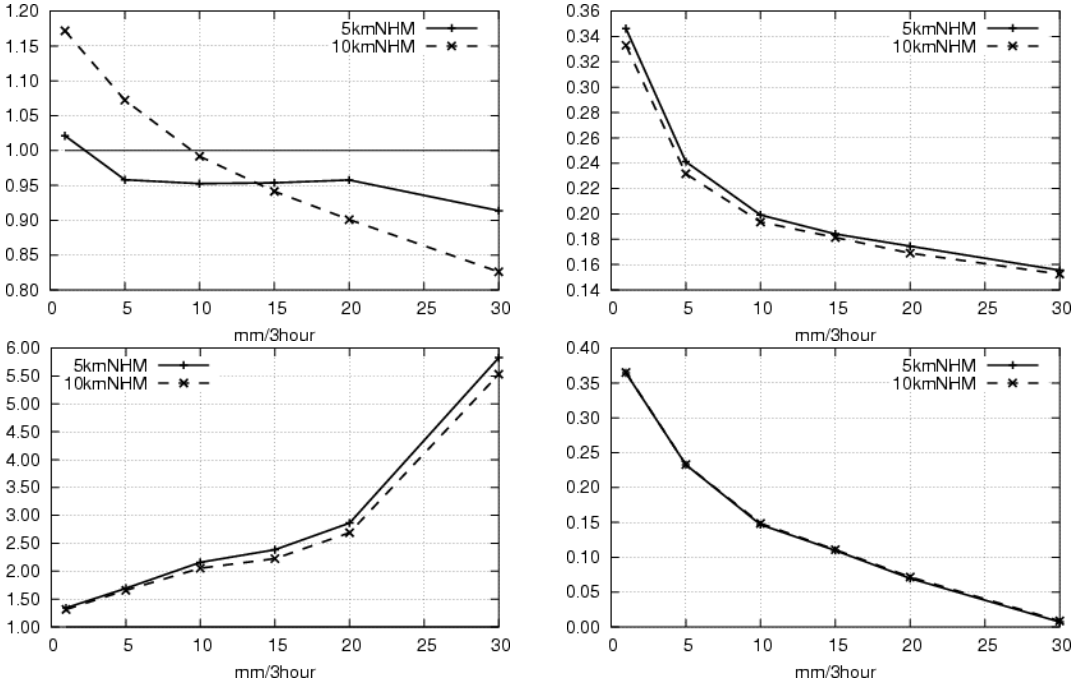

Figure 1: The bias and threat scores of precipitation forecast against radar-rain gauge composite rain data. The solid line indicates 5km-NHM and the dashed line indicates 10km-NHM. left:bias score, right:threat score, upper:in summer, lower:in winter.

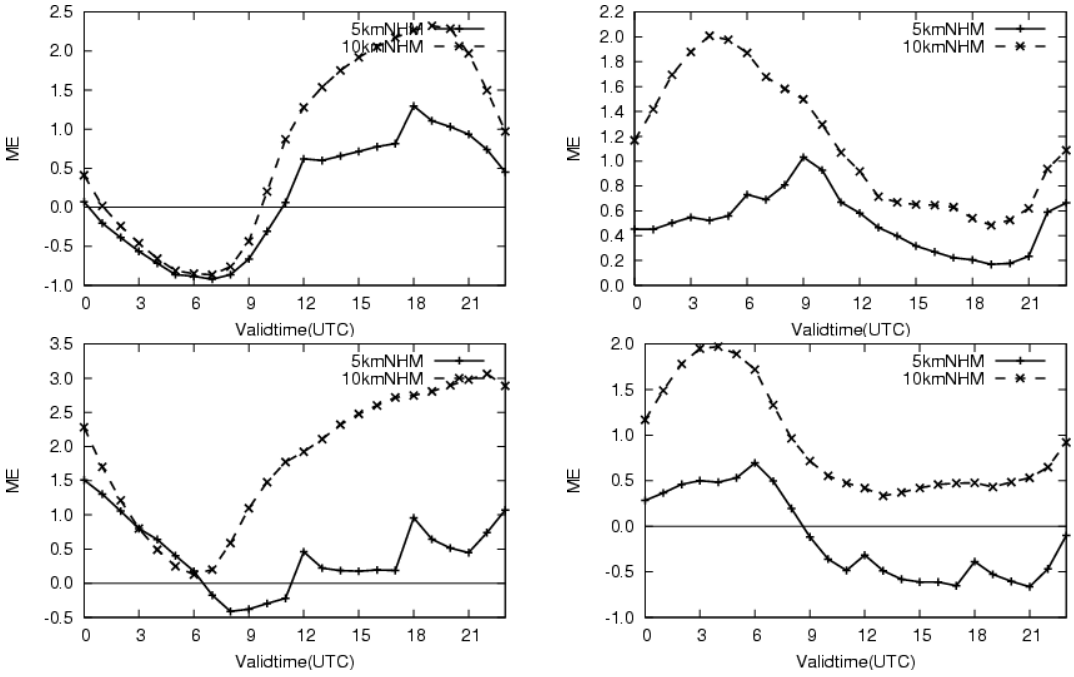

Figure 2: Diurnal change of mean errors of temperature and wind speed (03 UTC is noon and 15 UTC is midnight at local time). The solid line indicates 5km-NHM and the dashed line indicates 10km-NHM. left:temperature, right:wind speed, upper:in summer, lower:in winter.

and Y. Yamazaki, 20056 The operational JMA Non-hydrostatic Mesoscale Model. *Mon. Wea. Rev.* in press.

[2] Kain J. and J. Fritsch, 1993: Convective parameterization for mesoscale models, The Kain-Fritsch scheme. The Representation of Cumulus Convection in Numerical Models, Meteor. Monogr., **24**, 165-170.

A first Case Study of 3-Dimensional Turbulence with full Metrics in the Very Short Range Forecast Model LMK

Michael Baldauf
Deutscher Wetterdienst, Kaiserleistraße 42, 63067 Offenbach am Main
E-mail: michael.baldauf@dwd.de

1 Introduction

At the Deutscher Wetterdienst the numerical weather forecast model LMK (LM-Kürzestfrist) is currently under development. It is based on the LM (Lokal-Modell) and will be used for very short range forecasts (up to 18 hours) and with a resolution on the meso-γ-scale (about 2.8 km). The development tasks cover the areas of data assimilation, numerics, physical parameterisations, and new verification approaches.

In Baldauf (2005a) the formulation of the turbulent fluxes and flux divergences in terrain following coordinates and for spherical base vectors was derived. The result for the scalar flux divergence is

$$\rho\frac{\partial s}{\partial t} = \underbrace{-\frac{1}{r\cos\phi}\frac{\partial H^{*1}}{\partial\lambda}}_{(a)} \underbrace{-\frac{J_\lambda}{\sqrt{G}}\frac{1}{r\cos\phi}\frac{\partial H^{*1}}{\partial\zeta}}_{(b)} \underbrace{-\frac{1}{r}\frac{\partial H^{*2}}{\partial\phi}}_{(c)} \underbrace{-\frac{J_\phi}{\sqrt{G}}\frac{1}{r}\frac{\partial H^{*2}}{\partial\zeta}}_{(d)} \underbrace{+\frac{1}{\sqrt{G}}\frac{\partial H^{*3}}{\partial\zeta}}_{(e)} \underbrace{-\frac{2}{r}H^{*3}}_{(f)} \underbrace{+\frac{\tan\phi}{r}H^{*2}}_{(g)}, \quad (1)$$

and for scalar fluxes:

$$H^{*1} = -\rho K_s \frac{1}{r\cos\phi}\left(\frac{\partial s}{\partial\lambda} + \frac{J_\lambda}{\sqrt{G}}\frac{\partial s}{\partial\zeta}\right), \quad H^{*2} = -\rho K_s \frac{1}{r}\left(\frac{\partial s}{\partial\phi} + \frac{J_\phi}{\sqrt{G}}\frac{\partial s}{\partial\zeta}\right), \quad H^{*3} = +\rho K_s \frac{1}{\sqrt{G}}\frac{\partial s}{\partial\zeta}. \quad (2)$$

(Analogous expressions for the 'vectorial' diffusion of u, v and w). The terms (a), (c) and (e) in equation (1) describe the cartesian components of the flux divergence and are already contained in the 3D-turbulence scheme of the Litfass-LM (Herzog et al., 2002), which was implemented into the LMK code (Förstner et al., 2004). The (new) metric terms (b) and (d) describe corrections due to the terrain following coordinate. The terms (f) and (g) are due to the earth curvature and can be neglected with good approximation.

2 Implementation and test of the metric terms

The horizontal cartesian terms (a) and (c) are discretised explicitely whereas the vertical cartesian term (e) is in implicit form to consider the fact that the stability criterion can be violated in the case of small vertical level distance or large diffusion coefficients. The metric terms (b) and (d) are some sort of horizontal correction due to the terrain following coordinate system and therefore the first attempt for their discretisation is also in explicit form. For the upper and lower boundaries all the centered differences were replaced by one-sided differences (for fluxes and flux divergences).

The correct discretisation of the 3D-turbulence and especially the metric terms was tested by the analytically well known isotropic diffusion of a Gaussian inital tracer distribution and with a constant diffusion coefficient. A comparison with the simulation of such a tracer cloud in the terrain-following grid, which is destorted by orography, showed the correct implementation of all the metric terms (Baldauf, 2005b).

3 A real case study

To inspect the importance of 3D-turbulence and especially the metric terms a first real case study was performed. The simulation was started at the 12. August 2004, 12 UTC and lasted 18 h. This was a strong convective situation with the development of a squall line. Three cases: (1) only 1D (vertical) turbulence, (2) 3D-diffusion without metric terms, and (3) 3D-diffusion with metric terms, were carried out. The simulations were performed with the 'standard' LMK horizontal resolution of 2.8 km and a time step of 30 sec. As in the idealized diffusion test, the explicit discretisation of the metric terms did not generate any stability problems.

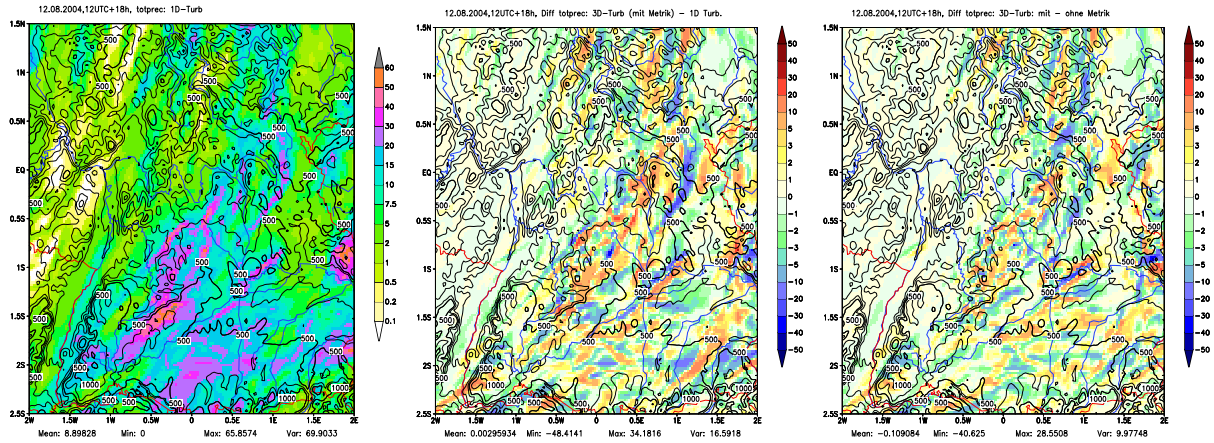

Figure 1: Left: Total precipitation sum over 18h for the 12.08.2004, 12 UTC run with the currently used 1D turbulence. Differences of the 18h precipitation sum between 3D-turb. with metric terms and 1D-turb. (middle), and between 3D-turb. with and without metric terms (right).

Figure 1 (left) shows the precipitation sum after 18 h simulation time over Southern Germany. This area was chosen, because during the simulation time the precipitation event travelled completely over this area and lied outside of it at the end of the simulation. Therefore in the following difference plots, we can be sure, that the differences do not alter because of new precipitation events. Figure 1 (middle) shows a difference plot between case 3 (complete 3D-turbulence) and case 1 (only vertical turbulence). The differences can reach maximum and minimum values nearly at the same order as the precipitation sum itself. But the mean value shows, that the 3D-turbulence has almost no influence to the total amount of precipitation. This seems to be reasonable, as turbulence occurs mostly in the boundary layer, whereas the most part of precipitation is generated above. But the transport of precipitation (especially with the prognostic precipitation scheme, which is unconditionally necessary at this resolution) is heavily influenced by the boundary layer flow. The 18h-precipitation sum is a marker of all these integrated flow changes due to 3D-turbulence. These effects can lead to shifts of the precipitation areas up to 20-30 km, which is a non-neglectable effect e.g. for hydrological applications. Of course further work has to be done to inspect if this influence can be seen also in other weather situations.

The effect of the metric terms themselves is shown in Figure 1 (right), the difference between case 3 (with metric terms) and case 2 (without metric terms). The maxima and minima are slightly smaller, but obviously they cannot be neglected in comparison to case 2 (this was already theoretically derived in Baldauf, 2005a). The mean value of the difference 'case 1 - case 3' is even smaller as in the difference 'case 2 - case 3'. If one accepts the statement, that 3D-turbulence does not alter the total amount of precipitation, then the metric terms obviously have a positive impact on the conservation of total precipitation amount, too.

References

Baldauf, M. (2005a): The Coordinate Transformations of the 3-dimensional Turbulent Diffusion in LMK, *COSMO-Newsletter*, No. 5, 132-140

Baldauf, M. (2005b): Implementation of the 3D-turbulence metric terms in LMK, *COSMO-Newsletter*, No. 6

Förstner, J., H.-J. Herzog and G. Vogel (2004): Implementation of a 3D-Turbulence Parameterisation for the Very Short Range Forecast Model LMK, *WGNE Blue Book*, http://www.cmc.ec.gc.ca/rpn/wgne/

Herzog, H.J., G. Vogel and U. Schubert (2002): LLM - a nonhydrostatic model applied to high-resolving simulations of turbulent fluxes over heterogeneous terrain, *Theor. Appl. Climatol.*, 73, 67-86

HEAT WAVES IN THE MEDITERRANEAN REGION:
ANALYSIS AND MODEL RESULTS

Marina Baldi, Massimiliano Pasqui, Francesco Cesarone, Giovanna De Chiara*
Institute of Biometeorology - CNR, Rome, Italy
*Corresponding Author: m.baldi@ibimet.cnr.it

Using the Regional Atmospheric Modelling System (RAMS) and the NCEP-NCAR reanalysis, Baldi et al. (2004) have demonstrated that a latitudinal northward shift of the West African monsoon is related to observed SST anomalies in the Gulf of Guinea. In an idealized simulation, Baldi et al. (2004) perturbed the climatological SST in the first half of the summer, specifically in May-June, introducing a colder dipole in the Gulf of Guinea which in turn favoured a deeper inland northward penetration of the oceanic moisture, while warm SSTAs, in the second half of the summer, provided additional moisture which enhanced the strength of the monsoon, which, through its thermodynamics and the dynamics, resulted in stronger subsidence over the Mediterranean Sea. Figure 1 shows the effect of colder SST in the Guinea Gulf on the Geopotential height at 500hPa, simulated by RAMS, obtained forcing the whole system by introducing a cold SST anomaly.

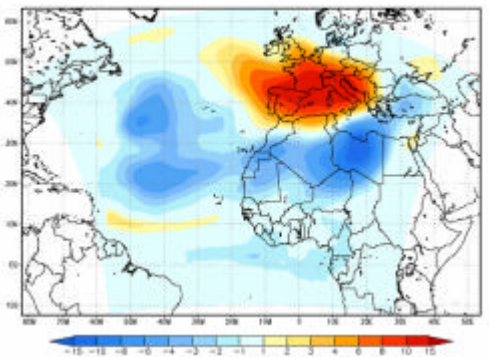

Figure 1: Effects of cold June SSTAs in the Gulf of New Guinea on the Geopotential Height at 500 mb in August (RAMS sensitivity run).

The simulation, started on April 1st 2003, lasted until end of September 2003, in order to capture the main features of the exceptionally long heat wave of summer 2003. The domain extends from central Europe to the Gulf of Guinea and, longitudinally, it includes the Atlantic Ocean, the whole Mediterranean Basin and it extends eastward to the Balkans. The SST has been updated weekly during the whole period, while a monthly average is used for the soil moisture. Results of the simulation, in terms of Geopotential field at 850 and 500 hPa and the air Temperature at 850 hPa are well reproducing the corresponding maps obtained from the NCEP/NCAR reanalysis. In particular, the use of weekly SST, instead of monthly mean, increases the performance of the model in reproducing the weather patterns.

As first shown by model results, a key role is certainly played by a positive feedback on the temperatures, by a low convective rainfall activity, and by the large soil moisture deficits, accrued in the region due to an exceptionally early and warm spring, which may have intensified most of the subsequent summer heat waves. Moreover the use of weekly versus monthly SST in the whole domain indeed improved the performance of the model, as well as more accurate soil moisture data at finer resolution can certainly do (results under investigation).

The Guinea Gulf SST, and, thus, the West African Monsoon, contribute significantly to the hot episodes triggering, and to the inter-annual variability of the central-western Mediterranean summer climate (Baldi et al., 2004).

The analysis performed and the simulation results are a major starting point for a better understanding of the physical mechanisms yielding to such severe events, and will improve the forecast of these phenomenon (expected to occur more frequently in the course of the 21st century, as suggested by regional climate scenarios, see Beniston, 2004), as needed for an efficient early warning systems. In particular, through numerical simulations, it is possible to distinguish the role played by each of the different physical processes (soil moisture depletion, positive feedback on summer temperatures, and lack of convective rainfall) characterizing severe episodes such as the summer 2003.

Contribution of temperature, precipitation, and solar radiation from dynamically downscaled global climate model to predicting peanut yields in the SE USA.

Bellow, J.G.[1] ,Shin, D.,W.[1], Schoof, J.[1], Jones, J.W.[2], O'Brien, J.J.[1]
bellow@coaps.fsu.edu; Florida State University[1], University of Florida[2]

The impact of the El Niño-Southern Oscillation (ENSO) on the seasonal climate in Alabama, Florida, and Georgia has been well documented for temperature and precipitation and can influence the yields of a variety of field crops grown in the region. The use of ENSO climatology to drive a process based crop model such has those found in the DSSAT 4.0 cropping system models provides the state-of-the-art means to forecast crop yields. However, the ENSO signal in the southeast is weak during the critical period JJAS and ENSO climatology based yield forecasts have more variability than is desirable.

Improvements in numerical climate models at both the global (GCM) and regional (RCM) scales suggest an opportunity to enhance yield forecasts. The CROPGRO CSM model was parameterized for Georgia Green peanut with a 24 Apr planting date, rainfed conditions, and local soil profiles. Sensitivity analyses were made for the period 1994 through 2003 at nine sites across AL, FL, and GA. Two convection schemes were employed, the SAS (Simplified Arakawa-Schubert, Pan and Wu 1994) scheme from NCEP and the RAS (Relaxed Arakawa-Schubert) scheme from NRL (Rosmond 1992). The RCM daily output was bias corrected as described by Wood et al. (2002) and consists of remapping the exceedence probabilities (percentiles) of the predicted data to those of the observed data. This step is particularly important for precipitation, because the regional climate model tends to produce a large number of wet days with small precipitation amounts. For each site and year, peanut growth and development were simulated using observed weather conditions, the conditions forecast by the FSU RCM, a synthetic forecast comprised of both observed conditions and FSU RCM output for temperature, precipitation, and solar radiation, and the conditions associated with ENSO phases.

The results indicate that the temperature and solar radiation fields contributed least to errors (RMSE) in peanut yield forecasts (kg ha^{-1}). Yield prediction errors from these two fields exhibited low temporal and spatial variability with little impact attributable to convection schema. Yield prediction errors from precipitation were larger and were more temporally and spatially variable (Figures 1 & 2). Overall, the RCM with RAS convection had the lowest RMSE peanut yield across all years and sites. For temporal variability, the RCM SAS was comparable to ENSO climatology in some years and superior in 1994, 1997, 1998 (Fig 3). The effect of bias correction on forecast error in peanut yields was small for all climate fields. These results suggest that application of RCM forecasts have the greatest immediate potential for use in crop developmental models that are most sensitive to temperature. Better bias correction approaches and the implementation of ensemble yield forecasts may improve the reliability of RCM forecasts when applied to crop yield forecasts. More forecast years may allow better resolution of conditions where RCM forecasts are superior to ENSO climatology

Acknowledgments: This research was supported by the Applied Research Center, NOAA Office of Global Programs and the USDA through the Cooperative State Research, Education, and Extension Service.

References:

Rosmond, T. E., 1992. The design and testing of the Navy operational global atmospheric system. Weather Forecast. 7: 262-272.
Pan, H.L., and Wu, W.S., 1994. Implementing a mass flux convection parameterization scheme for the NMC Medium-Range forecast model. Tenth Conference on Numerical Weather Prediction, Am. Meteorol. Soc., Portland, Oreg.
Wood, A.W., Maurer, E.P., Kumar, A., Lettenmaier, D.P., 2002. Long-range experimental hydrologic forecasting for the eastern United States J. Geophys. Res. Atmosp. 107: D20.

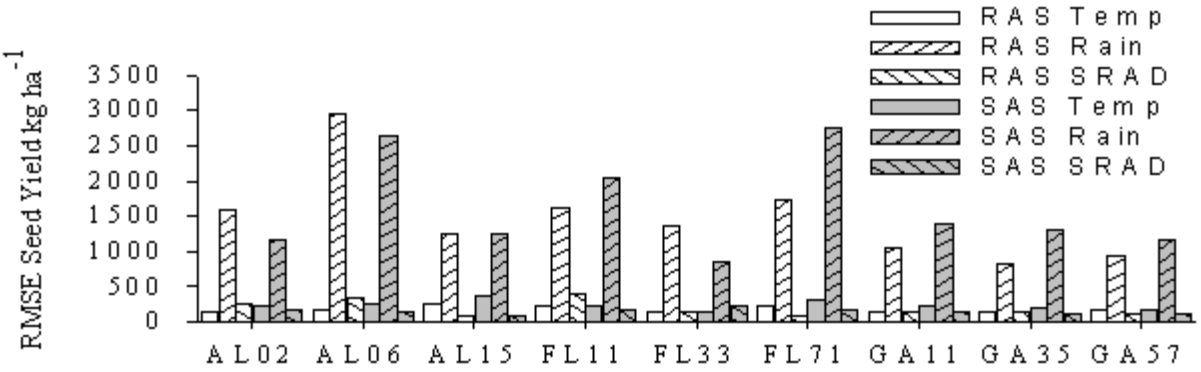

Fig 1. Contribution of FSU RCM RAS-SAS climate fields to mean error in dry peanut seed yield at nine SE sites.

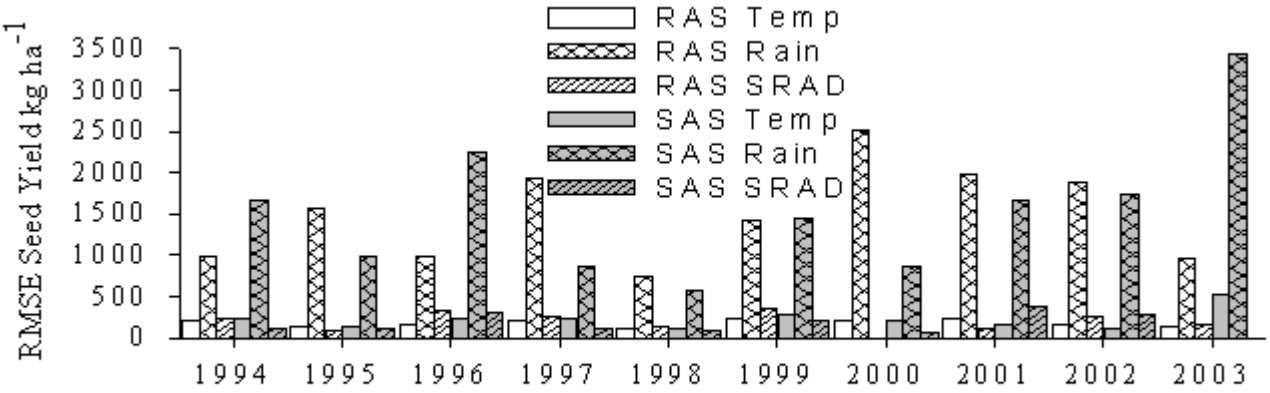

Fig 2. Contribution of FSU RCM RAS-SAS fields to mean error in dry peanut yield 1994-2003

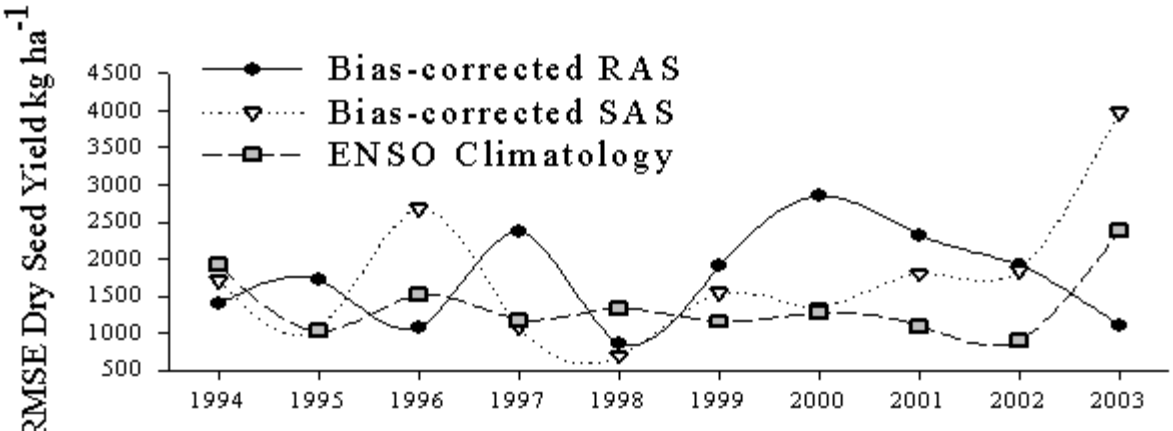

Fig 3. Error in dry peanut yield in FSU RCM RAS-SAS forecasts compared to yield forecasts using historical ENSO Climatology

Forecast of strong precipitation for locations of the European territory of Russia

L.V. Berkovich, Yu.V. Tkacheva

Hydrometeorological Research Center of Russia
9-13 Bol'shoy Predtechenskiy Lane, 123242, Moscow-242, Russia
E-mail: lberkov@mecom.ru

The Hemisphere Forecast Model (HFM) for forecasting meteorological fields in the free atmosphere and in the boundary layer of the atmosphere (BLA) is used in the Hydrometeorological Center of Russia. The HFM constitutes also the basis for forecasting meteorological quantities and weather characteristics for locations of the European territory of Russia (air temperature and humidity, wind speed and direction, wind gusts, three layer cloudiness, widespread and convective precipitation, fogs, snowstorms, glaze ice etc.) [1- 3]. The forecast of strong precipitation (more than 7 mm per 12 h) is of particular importance among the mentioned characteristics.

The accuracy of the initial data on temperature and humidity is the most important for forecasting strong precipitation. The comparison of these meteorological quantities (especially humidity) at different levels of the atmosphere exhibits a considerable difference between these fields in the data of different meteorological centers in GRIB code.

Prolonged experience of hydrodynamic forecast of elements and characteristics of weather (including precipitation) at various geographical locations enabled to accumulate considerable experience in this area in the course of operational forecasts in the Hydrometeorological Center of Russia.

This concerns: the resolution of the prognostic model and the completeness of physical processes, the accuracy of the initial data for different meteorological quantities, the type of precipitation: widespread, convective and mixed, and, finally, the conditions when the processes of condensation and precipitation intensify.

This if one of the conceivable reasons why differ the prognostic quantities of precipitation calculated in the principal forecast centers (Exeter, NCEP et al.).

Using a more powerful computer, now available in the operational prediction group, we implemented the variant of the model with a resolution of 30 km with adaptation of physical processes, and we did all the preparatory work for the output of operational prognostic data.

Numerical experiments on strong precipitation prediction with alternation of horizontal resolution were carried out in the Hydrometeorological Center of Russia using the HFM. Three variants of resolution (grid steps) were obtained: 150 km, 75 km and 30 km. Table 1 shows the calculation results for strong precipitation cases for various points of the European territory of Russia. The number of examples ensures the plausibility of the statistics enabling to judge how successful are strong precipitation forecasts.

REFERENCES

1. Berkovich L.V., Belousov S.L., Kalugina G.Yu, Tkacheva Yu.V. Short-range hydrodynamic forecasting of the local weather patterns. – Res.Act. in Atmos. And Oceanic Modeling, 2000, No.30, 5.1-5.2.

2. Belousov S.L., Berkovich L.V., V.A.Shnaydman. Short-range forecasting of meteorological variables and weather patterns. – Res.Act. in Atmos. And Oceanic Modeling, 2001, No.31, 5.1-5.2.

3. Berkovich L., Tkacheva Yu., The hydrodynamic short-range of local weather forecasting . Research Activity in Atmospheric and Oceanic Modeling, 2003,No 33, 5.1-5.2.

Table 1

DATE	LOCATIONS	PRESIPITATIONS (мм/day)				
		FORECASTS			REAL	ERRORS OF FORECASTS: STEP 30 KM
		150 км	75 км	30 км		- REAL
02.12.2005	KRASNODAR	10.0	10.7	12.6	26.0	-15.4
	ROSTOV	11.0	12.1	13.3	23.0	-10.0
	STAVROPOL	12.0	13.6	19.2	19.0	0.2
03.12.2005	KRASNODAR	7.0	6.8	20.8	18.0	2.8
	ROSTOV	7.0	9.4	14.6	35.0	-20.4
	STAVROPOL	6.0	6.3	13.4	24.0	-10.6
05.12.2005	KRASNODAR	4.0	6.1	6.2	18.0	-11.8
	ROSTOV	4.0	4.9	7.4	22.0	-14.6
07.12.2005	BELGOROD	6.0	5.8	8.3	13.0	-4.7
08.12.2005	MOSCOW	5.8	6.8	8.5	10.0	-1.5
	BELGOROD	5.2	6.6	16.4	23.0	-6.6
	VORONEJ	4.9	6.4	19.3	19.0	0.3
	KURSK	6.5	7.9	11.5	20.0	-8.5
	TAMBOV	6.3	7.1	17.5	19.0	-1.5
	TULA	8.4	9.2	9.7	11.0	-1.3
09.12.2005	MOSCOW	3.0	7.4	9.0	11.0	-2.0
	IVANOVO	5.6	7.3	8.5	21.0	-12.5
	KOSTROMA	4.0	5.4	7.2	21.0	-13.8
	RJAZAN	6.0	8.7	10.7	20.0	-9.3
	TAMBOV	6.3	9.6	9.0	11.0	-2.0
	TULA	3.8	6.8	7.3	16.0	-8.7
10.12.2005	KOSTROMA	1.0	2.3	1.9	12.0	-10.1
11.12.2005	MOSCOW	2.4	3.3	7.0	7.0	0.0
	KALUGA	3.1	1.9	10.7	11.0	-0.3
12.12.2005	S.-PETERBURG	4.6	6.3	8.5	29.0	-20.5
	TVER	5.2	6.7	8.6	13.0	- 4.4
20.12.2005	MOSCOW	2.4	6.2	12.6	14.9	-2.3
12.05.2005	MOSCOW	5.8	8.7	18.2	19.8	-1.6
20.05.2005	MOSCOW	5.0	6.7	12.3	14.9	-2.6
25.05.2005	MOSCOW	3.2	4.1	8.7	9.0	-0.3
13.06.2005	MOSCOW	3.5	5.5	12.3	12.5	-0.2
14.06.2005	MOSCOW	7.9	9.0	9.3	9.6	-0.3
18.03.2005	MOSCOW	2.6	4.2	11.0	8.3	2.7
SUM OF 33 FORECASTS		176.0	230.6	367.6	562.1	193.4
PERSENTAGES		31.3	40.9	65.4	100.0	34.6

Progress of the AROME mesoscale NWP project

F. Bouttier, G. Hello, Y. Seity, S. Malardel

affiliation: Météo-France/CNRM, 42 Av. Coriolis, 31057 Toulouse cedex
corresponding author: bouttier@meteo.fr

1. The model

Launched in 2000, AROME (Applications of Research to Operations at Mesoscale) aims to develop an original mesoscale model and data assimilation system for operational NWP and the scientific community. AROME builds upon ECMWF's IFS software (a global NWP system that was extended by the ALADIN cooperation into a limited area model (LAM) and data assimilation system, and non-hydrostatic (NH) dynamics), and the Méso-NH software, which provides most of AROME's physical parameterizations. The IFS framework ensures good computer optimization on a variety of architectures, and quick pull-through of R&D on data assimilation algorithms and use of satellite data. The link to Méso-NH provides excellent scientific expertise and development workforce from the mesoscale atmospheric research community and universities.

Namely, the AROME model core is a NH LAM with a semi-Lagrangian advection scheme and a spectral (bi-Fourier) semi-implicit solver, that allows e.g. using a timestep of 1 minute with an horizontal resolution of 2km, with perfect stability and very good accuracy. The AROME model physical parametrizations are: a prognostic TKE turbulent mixing scheme, a prognostic cloud microphysics scheme with 5 condensed water species (cloud water and ice, precipitating water and ice, graupel), a tiling surface flux parametrization (with subgrid tiles for soil/vegetation [ISBA scheme] hydrology, town [TEB scheme], lake and sea prognostic mixing layer, multilayer snow), the ECMWF RRTM-IR/FM radiation scheme, a subgrid mass-flux shallow convection scheme, an optional interactive chemistry/aerosol scheme. The model has coupling facilities for mesoscale 3D ocean models and hydrology/flood models. The AROME physical parametrizations are the subject of intense research and development.

After initial validation on selected academic and real test cases, the AROME model has been producing daily real-time 24-hour runs in dynamical adaptation from the French ALADIN model, since June 2005. Real-time testing has been very satisfactory and some results are shown below. AROME has also been configured for local experimentation by the meteorological services of Hungary, Slovenia, Denmark, Sweden, Finland, Norway, and the Czech Republic. Dedicated real-time AROME runs are planned in support of the AMMA (African Monsoon in Western Africa, summer 2006), COPS (Convection in Southwestern Germany, summer 2007), and MAP D-PHASE (MAP hydrology demonstration on the Alps, summer 2007). Exploitation of AROME for operational NWP is scheduled for 2008 in Météo-France (possibly earlier in other institutes).

2. The data assimilation

The AROME data assimilation system is still being built. The development tool is the ALADIN 3D-Var assimilation (the subject of another article in this volume), which is operational. The ALADIN 3D-Var differs from the target AROME assimilation by three aspects: ALADIN is a simpler model (hydrostatic with cruder physics), its horizontal resolution is lower (of the order of dx=10km whereas AROME will use dx=1 to 3km), and the ALADIN 3DVar does not yet observe, analyze or initialize variables such as cloud or precipitating species, which are likely to be useful control variables for AROME. In other respects, the ALADIN 3D-Var is an ideal mesoscale assimilation tool thanks to its low numerical cost. It has been extensively tested in 2005 on a 3000km-wide domain on Western Europe, with the same observations and algorithms (except from the use of 3D-Var instead of 4D-Var, and the horizontal geometry) as the global 4D-Var ARPEGE data assimilation (operational at Météo-France), plus regional low-level observations of temperature and humidity, and cloud-cleared radiances from the SEVIRI imager of the Meteosat-8 (MSG series) satellite. The additional observations noticeably improve the humidity analysis, which in turn improves short-range forecasts of (mainly) precipitation and wind at lead times from 2 to 12 hours, for the time being. This system was declared operational in August 2005 and used since then to provide the initial state to the ALADIN forecasts over Western Europe (and, incidentally, to the AROME 2.5-km daily trial runs over France, which were found to be improved by the ALADIN 10-km assimilation as well)

3. Results so far

The AROME 2.5-km model has been run for several months over 400km-wide domains, usually on SW and SE France, and for some case studies over Paris or Brittany, which included convective systems, orographic

and coastal effects, synoptic storms and fronts, mediterranean, temperate and cold wintertime weather. The AROME performance was assessed with reference to in-situ routine data, radar and satellite imagery, and human forecasters. It is significant, both in absolute terms and relatively to the lower-resolution ALADIN model. The added value is very clear on low-level wind and temperature forecasts, thanks to the dynamical adaptation to complex orography and physiography. The sensible depiction of urban heat effects was a good surprise. The most spectacular improvements were experienced in convective situations, where AROME was able to depict realistic details (anvils, gust fronts, texture and maximum of the precipitation field) of the weather which are completely absent from lower resolution models. The positioning of convective cells is still imprecise due to the lack of a fine-scale assimilation, and the added value is mostly in the information on the probabilistic distribution of weather features at scales of the order of 50km, i.e. much larger than the actual model grid size. In some situations, the location and timing of rain and convective cells are spectacularly precise, presumably because they are the result of orographically-driven wind circulations, which are highly predictable when the model has sufficient resolution.
A 3-day Mediterranean flooding case occurred close to Marseilles in September 2005. Such events are characterized by synoptically-driven convective cells in warm, moist air, that keep regenerating for many hours in a row over coastal orographic features. In this particular case, large-scale models (global models from ECMWF and Météo-France) gave a good depiction of the synoptic context, and AROME improved the quantitative precipitation forecast on scales of the order of 20 to 50km. Interestingly, AROME also improved larger-scale aspects of the precipitation forecasts, compared to ALADIN, presumably because of feedback from the convective cloud microphysics and small-scale turbulence to the generation of cold pools (by rain evaporation), to the triggering of precipitation, and to the humidity and vorticity fields on larger scales.

4. Conclusions

The future work will concentrate on adapting the ALADIN 3DVar analysis system to the higher resolution of AROME and to using radar and satellite data. Benefits will need to be assessed not just in terms of the analysis algorithm itself, but also in terms of the interpolay of model and observations during assimilation cycles. On the model side, the known weaknesses of the current AROME version are being adressed:

- the representation of non-convective, non-frontal clouds is very poor, which is very harmful in anticyclonic wintertime weather. The introduction of a subgrid shallow convection scheme is expected to improve cloud cover and its feedback with radiation.
- the forecasts are adversely affected by lateral boundary effects at up to 80km of the border. The numerics of the lateral boundary coupling are being revisited.
- the specification of surface conditions e.g. town heating source term, soil moisture, coastal physiographies, need to be improved.
- the diffusion along terrain-following model surfaces is inappropriate in narrow valleys, in stably stratified atmospheres, which are more horizontal in nature. A case-sensitive formulation of the diffusion is being developed, that plays with the diffusive nature of the semi-Lagrangian advection.

References: see http://www.cnrm.meteo.fr/arome/

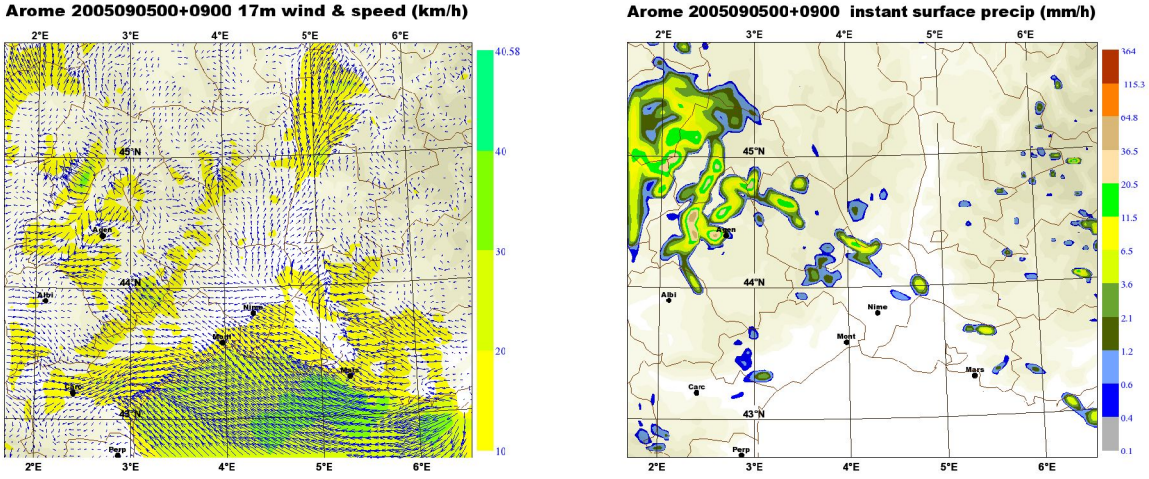

Examples of fields forecast by the AROME 2.5km model: low-level wind vectors (color shading according to speed), and precipitation field, on the SouthEast of France.

The impact of lateral boundary data errors on the simulated climate of a nested Regional Climate Model

Emilia Paula Diaconescu and René Laprise
Département des Sciences de la Terre et de l'Atmosphère, Université du Québec à Montréal, Canada
e-mail : diacones@sca.uqam.ca

1. Introduction

The primary tools to study anticipated climate changes are the coupled global and nested regional climate models. General Circulation Models (GCMs) provide a global-scale view of projected climate at typically coarse horizontal resolution and hence cannot be used directly by most impacts studies that require grid scales of 10 to 100 km or finer. Information at regional scales can be simulated with limited-area, high-resolution Regional Climate Models (RCMs) driven by the large-scale information from GCMs. But the GCM–simulated data are not perfect; they contain errors due to model imperfections. In this study, we investigate the response of a Regional Climate Model (RCM) to errors in the atmospheric data used as lateral boundary conditions (LBC) using a perfect-model framework nick-named the "Big-Brother Experiment" (BBE).

2. The "Big-Brother Experiment"

The BBE has been designed by Denis et al. (2002b) and it permits to evaluate the errors due to the nesting process excluding other model errors. First, a high-resolution (45 km) RCM simulation is made over a large domain. This simulation, called the Perfect Big Brother (PBB), is driven by reanalysis from the National Centres for Environmental Prediction (NCEP); it serves as reference virtual-reality climate to which other RCM runs will be compared. Errors of adjustable magnitude are introduced by performing RCM simulations with increasingly larger domains at lower horizontal resolution (90 km); such simulations are called the Imperfect Big-Brother (IBB) simulations and they are used, after removing small scales in order to achieve low-resolution typical of today's General Circulation Models (GCM), as LBCs for smaller domain high-resolution RCM runs. These small-domain high-resolution simulations are called Little Brother (LB) simulations. The climate statistics of the LB are compared to those of the PBB in order to estimate the errors resulting solely from nesting with imperfect LBCs, while the difference between the climate statistics of the IBB and those of PBB simulations mimic errors of the nesting model.

The simulations are performed over the East Coast of North America for five consecutive February months (from 1990 to 1994) using the Canadian RCM. To facilitate calculations, display and intercomparison between the fields, the simulations are interpolated onto a common 45-km resolution 100 x 100 polarstereographic grid, excluding the sponge zone, for the statistical analysis. A spatial decomposition is applied to separate fields into their large-scale and small-scale components using a 2-D discrete cosine transform filtering technique, suitable for non-periodic data (Denis et al. 2002a). A temporal decomposition of fields is also performed to separate stationary and transient components, and the Taylor diagrams (Denis et al. 2003, Taylor 2001) are used to analyse the errors in the IBB and LB fields, relative to the PBB reference, for each of the four components of the fields.

3. Results and discussion

The results for the precipitation rate field are summarized in figure 1.

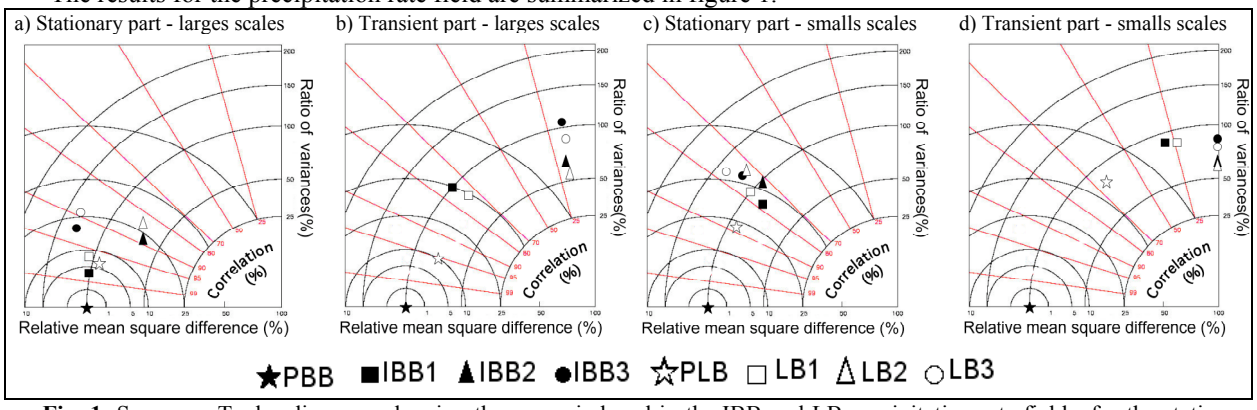

Fig. 1. Summary Taylor diagrams showing the errors induced in the IBB and LB precipitation rate fields, for the stationary and transient parts of the large- and small-scale components of the field.

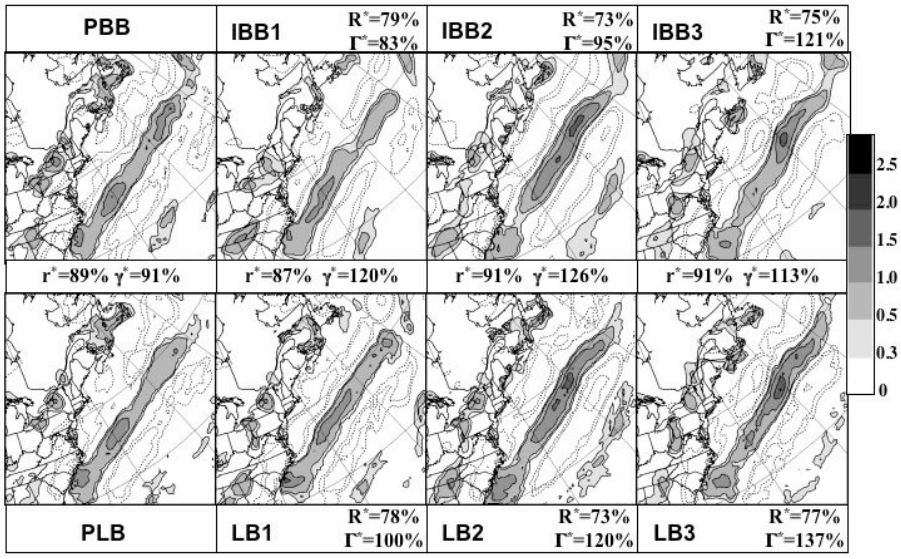

Fig. 2. Time-average small-scale precipitation rate fields (mm/day) for PBB and IBBs are shown in the top panels and that for the LBs in the bottom panels. Negative contours are shown dotted. Spatial correlation coefficients (R^*) and ratio of spatial variances (Γ^*) between PBB and IBBs are given in the subtitles. Spatial correlation coefficients (r^*) and ratio of spatial variances (γ^*) between each IBB and corresponding LB are indicated between the top and bottom panels.

Errors are present in both stationary and transient parts for the IBB simulations, but the transient components of the field exhibit the largest errors due to rather weak temporal correlation. The points corresponding to the LB fields are close to those corresponding to the driving IBBs for all four components of the fields, indicating the presence of similar errors in the precipitation rate fields of LBs to those contained in the corresponding fields of IBBs. For the stationary component of the large scales (Fig.1. a), LBs have almost the same ratio of spatial variances as the IBBs and a slightly smaller spatial correlation coefficient. In general, the LB reproduces the amplitude of its IBB precipitation rate and the shape of LB field is closer to that of the corresponding IBB than to the reference field (figure not shown). However, the spatial extent is found to be smaller for all LBs. This feature is noted in the PLB too and is due to the fact that, at the boundaries, the vertical velocity is set to zero in CRCM. This setting hinders the development of precipitations in the south-west part of the domain and delays the onset of precipitation, pushing the maximum further North. In spite of this the correlation coefficient between the LB and its IBB are approximately the same for all LBs, irrespective of the errors of its corresponding IBBs. This suggests that most part of stationary large-scale errors of the IBBs are reproduced by the corresponding LBs. For the stationary small scales (Fig. 1c), the LB fields are characterised by spatial correlation coefficients that are similar to the corresponding IBB fields and there is a little increase in the LB spatial variability in comparison with corresponding IBBs, irrespective of the spatial variance of the IBB fields. Fig. 2 shows the stationary small-scale part of the precipitation rate fields. The LBs represent better the small-scale features over the Great Lakes and the Maritimes regions through its finer horizontal resolution, which permits better representation of the coastline and the orographic features. But for the ocean region, where the small scales are mostly located, LB develops small scales that are closer to those of the IBB that drives it than those of the reference field. The spatial correlation coefficient between LB and its IBB is almost the same for all four cases. Therefore, irrespective of LBC errors, LB reproduces a great part of the stationary small-scale field of its IBB. This result suggests that the large scales precondition the small scales and therefore it is necessary to provide the accurate large-scale circulation at the lateral boundary of RCM in order to obtain accurate small scales. Similar results were observed for the mean sea level pressure and temperature at 850 hPa fields (Diaconescu et al. 2005).

In conclusion, the study indicates that the quality of lateral boundary data plays a critical role in regional climate modelling for the winter period, highlighting the need for good LBCs and hence the necessity for a credible GCM.

References

Denis B, Côté J, Laprise R (2002a) Spectral decomposition of two-dimensional atmospheric fields on limited-area domains using the discrete cosine transform (DCT). Mon Wea Rev 130: 1812-1829

Denis B, Laprise R, Caya D (2003) Sensitivity of a regional climate model to the lateral boundary conditions. Climate Dyn 20: 107-126

Denis B, Laprise R, Caya D, Côté J (2002b) Downscaling ability of one-way nested regional climate models: the Big-Brother experiment. Climate Dyn 18: 627-646

Diaconescu EP, Laprise R, Sushama L (2005) The impact of lateral boundary data errors on the simulated climate of a nested Regional Climate Model (Submitted to Climate Dynamics)

Taylor KE (2001) Summarizing multiple aspects of model performance in single diagram. J Geophys Res 106: 7183-7192

New Dimension of NCEP Short-Range Ensemble Forecasting (SREF) System: Inclusion of WRF Members

Jun Du*, Jeff McQueen, Geoff DiMego, Dusan Jovic, Xiaoxue Wang, Binbin Zhou, Hui-Ya Chuang, Matt Pyle, George Gayno, Eric Rogers, Tom Black, Zavisa Janjic, Brad Ferrier, Geoffrey Manikin, Zoltan Toth and Jimy Dudhia

EMC/NCEP/NOAA, SAIC and NCAR/UCAR, Washington DC, U.S.A.

1 Introduction

A 10-member Short-Range Ensemble Forecasting (SREF) system was operationally implemented and used at NCEP in May 2001 (Du and Tracton, 2001), which was the first real-time, operational regional ensemble prediction system in the world. From the very beginning of its development stage, NCEP SREF system has been emphasizing on **both** initial condition (IC) and model physics uncertainties at the same time by using multi-analysis (edas and gdas), multi-LBCs (using NCEP global ensemble members), multi-model (Eta and RSM) and perturbing ICs (breeding method) mixed approaches (Tracton et. al. 1998). In September 2003, another set of 5 Eta members but with a different version of convective scheme (Kain-Fritch) was added (make a total of 15 members) to further address physics uncertainty (Du et. al. 2003). The date of August 17, 2004 marks a new level of addressing physics diversity by implementing a total of 6 various convective schemes to the syetem besides perturbing ICs in 12 out of its 15 members (Du et. al. 2004; McQueen et. al. 2005).

This paper describes another important milestone which was achieved recently at NCEP. Six Weather-Research-Forecast (WRF) model based members were operationally implemented as part of the NCEP SREF system on December 6, 2005. Three members use NCEP NMM core, while other 3 members use NCAR EM core (Table 1). Now, there are a total of 21 members in NCEP SREF system in each cycle (two cycles per day to 87 hours, holizontal resolution varies among members from 32 to 45 km). This implementation marks the transition of NCEP SREF into WRF era. For the NCEP SREF products, please go to http://wwwt.emc.ncep.noaa.gov/mmb/SREF/SREF.html.

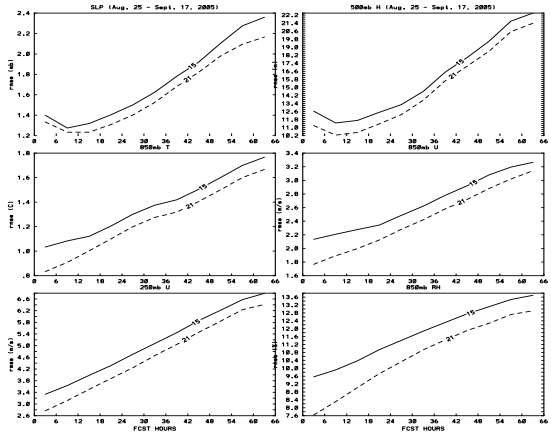

Figure 1: RMSE of the 21-member based ensemble mean forecast is largely reduced over that of the 15-member based for six selected fields: SLP, 500mb H, 850mb T, 850mb U, 250mb U and 850mb RH.

2 Results

Reader is referred to the captions of Figures 1-6 for the description of results. All results are evaluated against the NCEP global analysis (GDAS) and averaged over the 212 AWIPS grid domain (40km CONUS) and the period of Aug. 25 to Sept. 17, 2005.

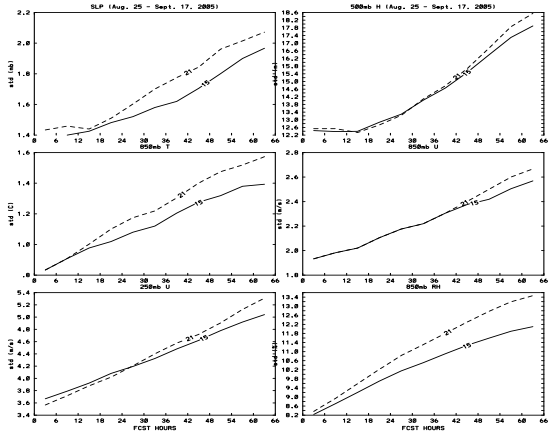

Figure 2: The ensemble spread is increased from the 15-member based to the 21-member based SREF system with a larger growth rate too!

3 Looking Forward

Bias correction is an immediate need for this 21-member system to be more robust (Fig. 6). It's also desired to investigate if WRF-member only SREF system will have similar quality comparing to the current multi-model based system, i.e. comparable accuracy in both ensemble mean and probabilistic forecasts and similarly large and good spread. For references, please see the NCEP SREF web.

* *Corresponding author address:* Dr. Jun Du, Environmental Modeling Center/NCEP, 5200 Auth Road, Camp Springs, MD 20746, USA; e-mail <Jun.Du@noaa.gov>

Dyn Core	Physics	Hor-Res	Configuration	Membership	IC	LBC	LSM
NCEP NMM	Eta/BMJ-based	40km	N America/non-hydro	3 (1 ctl, 2 bred)	GDAS	MREF	NOAH
NCAR EM	MM5/KF-based	45km	N America/non-hydro	3 (1 ctl, 2 bred)	GDAS	MREF	NOAH

Table 1: Configuration of how 6 WRF members are setup.

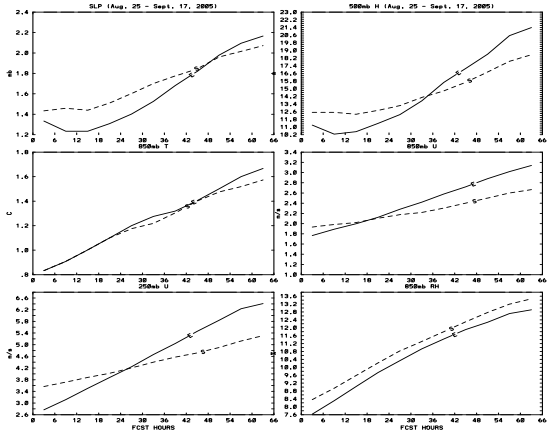

Figure 3: Due to the reduction of forecast error and the increase of ensemble spread, the spread-skill relationship is improved, i.e. the ensemble spread (lable "S") is now closer to the error of ensemble mean forecast (labled "E") for an originally underdispersive ensemble system.

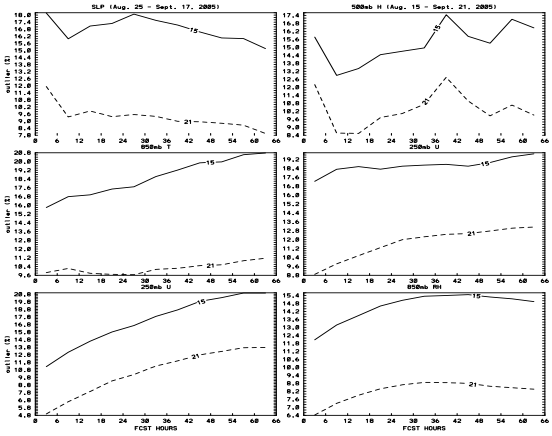

Figure 5: Outlier is decreased, i.e., the chance that truth to be left outside a forecast range predicted by the ensemble becomes much less after the 6 WRF members are added.

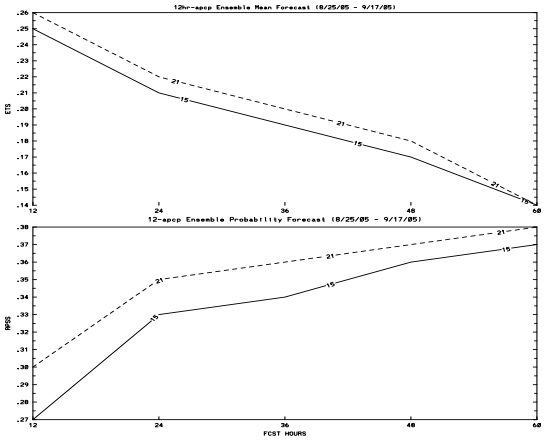

Figure 4: Similar improvements are also seen for ensemble mean precipitation forecasts in terms of Equitable Threat Score (upper panel) and for probabilistic precipitation forecasts measured by Ranked Probability Skill Score (here, the accuracy of 12km-NAM forecast is used as a reference in calculating the skill) (lower panel).

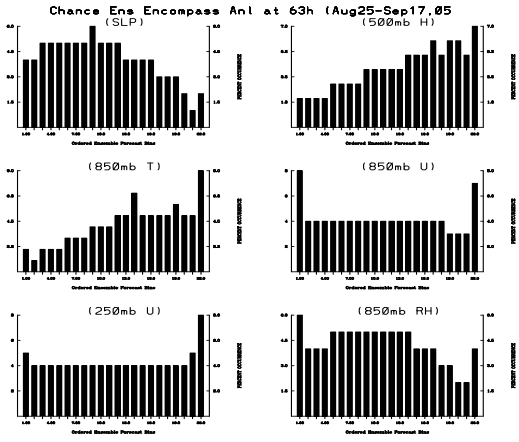

Figure 6: Talagrand Distribution or Rank Histogram shows that bias error is obviously possessed particularly for mass fields in the 21-member NCEP SREF system.

High-resolution and urbanised LM simulations applied to air pollution forecasts for selected air pollution episodes

Barbara Fay, Lina Neunhäuserer, Hubert Glaab
Deutscher Wetterdienst, P.O.Box 106465, D-63004 Offenbach am Main, Germany

Very high-resolution meteorological input data (1km resolution and below) are requested for air quality and dispersion modelling in emergency preparedness and information systems. With a growing part of the world population living in conurbations, NWP data are increasingly demanded and applied for the urban environment as well. The central task in air pollution modelling at the DWD is providing forecasts for the national nuclear emergency systems but scientific studies and operational customer demands are also carried out. DWD developed a trajectory model (TM), a Lagrangian particle dispersion model (LPDM) and a mixing height (MH) pre-processor using output of DWD's NWP models Globalmodell and Lokalmodell. In the European FP5 project FUMAPEX (Integrated Systems for Forecasting Urban Meteorology, Air Pollution and Population Exposure), Lokalmodell (LM) forecasts were scaled down to 1.1km by triple LM nesting and evaluated and inter-compared for air pollution episodes in Helsinki, Oslo, Valencia and Bologna (Fay and Neunhäuserer, 2005b; Fay et al., 2004, 2005). First LM urbanisation steps of urbanised physiographic parameters and an added anthropogenic heat source (without adapting or urbanising the LM turbulence scheme itself) were successfully applied to the April 2002 Helsinki episode (Neunhäuserer et al., 2006).

The trajectory model (TM), the Lagrangian particle dispersion model (LPDM) and the mixing height (MH) scheme use direct model output of the NWP models without interfaces and were adapted for high resolution of 2.8 and 1.1km with 45 vertical layers (operational 7km/35 layers). They were tested for air pollution episodes in Helsinki and Oslo, the TM and MH also for Valencia, and for the urbanised LM Helsinki simulations. In mountainous Valencia and Oslo, TM and LPDM simulations are very sensitive to grid resolution: 1.1 km simulations generally show improved topographic influence (channelling, blocking, much more localised mesoscale re-circulations in Valencia, Fig. 1) compared to the 7 km forecasts (Fay et al., 2005, Ødegård et al., 2005).

The MH scheme uses a gradient Richardson number approach based on the LM turbulent kinetic energy scheme and investigates the stability of individual NWP model layers (Fay et al., 1997). The results (Fay and Neunhäuserer, 2005a) show a very distinct influence of improved topography leading to enhanced structure of MH fields and a correct general decrease of MHs due to higher topography in mountainous areas. As validated previously for lower resolution, the non-urbanised and highly-resolved MH scheme generally performs well for daytime mixing heights for the FUMAPEX episodes in different climates and seasons. In cases of multiple inversion layers, an extension of the scheme to incorporate several vertically staggered boundary heights is needed. The scheme does, however, fail (like other schemes) for the strong stability and extremely strong and shallow (100 to 200m) Helsinki inversions persisting even during the day in the Helsinki Dec 1995 episode. These are approximated e.g. by LM vertical profiles of potential temperature and TKE but the MH scheme must intrinsically fail due to the strong continuous stability in all layers up to at least 1000m. This confirms the need for improvements in the scheme and its default values for the night-time and especially for stable (not only nocturnal) conditions.
The influence of the LM urbanisation measures is just visible in the near-surface trajectory paths for the Helsinki spring episode. As trajectories are determined from grid-scale winds they are much less sensitive to the thermal and sub-grid scale urbanisation effects than LPDM and MH. Increased turbulence and vertical velocity enlarge the general dimensions of the LPDM plume, show the effect of the increased land-sea circulation (Fig.2, left section) and partially large local impacts of urbanisation measures on the concentration distribution. The qualities of the MH scheme and the LM itself are also clearly shown in the successful simulation of a comprehensive heat island effect in LM parameters and fluxes (Neunhäuserer et al., 2006) leading to distinctly increased mixing heights above the city and its lee away from the coast, but even many kilometres downwind for the Helsinki 2002 episode (Fig.2, right section).
These episode and sensitivity studies show that the dispersion models are consistently formulated without the need of intermediate interface modules to the NWP models. Increased resolution and

initial urbanisation measures in the LM, thus, directly lead to distinctly improved and urbanised results including an urban heat island effect in all dispersion models.

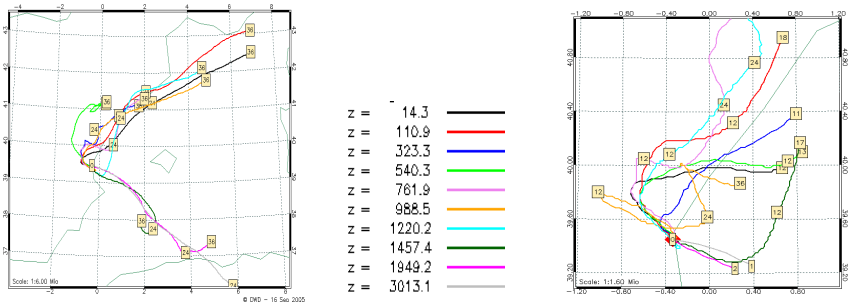

Fig. 1: LM trajectories starting at identical station at height z [m] on Valencia coast, Spain, 28 Sep 1999, 11UTC. Left: 7km, right: 1.1km resol. with improved local re-circulation leading to increased pollution levels.

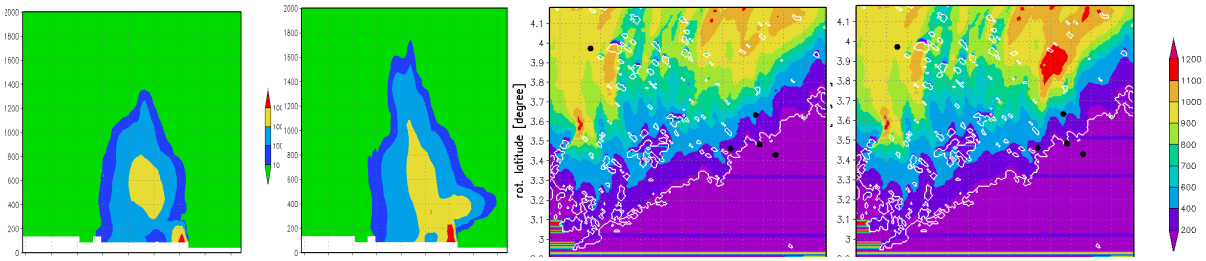

Fig. 2. Heat island above Helsinki for LPDM (left section) and MH (right section), 1.1km resolution, each comparing non-urbanised operational version (left) with urbanised version (urbanis. physiographic param. and anthropog. heat source of 60W/m² (right). LPDM: vertical cross-section of plume above Helsinki with increased sea breeze effect, 10 Apr 2002,00UTC+15h. MH: higher urban MH away from coast and drifted downwind from city (4 black dots are city obs stations), in [m] above model orography, 10 Apr 2002, 00UTC +36h.

Acknowledgements

This study is part of the EU FP5 project FUMAPEX (Integrated Systems for Forecasting Urban Meteorology, Air Pollution and Population Exposure), 2002-2005, funded by the EU under contract no. EVK4-CT-2002-00097. The authors thank their DWD colleagues in NWP modelling for valuable discussions and support.

References

Fay, B., Schrodin, R., Jacobsen, I., Engelbart, D. (1997) Validation of mixing heights derived from the operational NWP models at the German Weather Service., in: The determination of the mixing height – current progress and problems, EURASAP workshop proceedings, Risoe National Lab, 55-58.

Fay, B., L. Neunhäuserer, J.L. Palau, J.J. Dieguez, V. Oedegaard, N. Bjergene, M. Sofiev, M. Rantamäki, I.Valkama, J. Kukkonen, A. Rasmussen, A. Baklanov (2004) Model simulations and preliminary analysis for three air pollution episodes in Helsinki. FUMAPEX Report D3.3, DWD, Offenbach, Germany, 60pp.

Fay, B., L. Neunhäuserer, J.L. Palau, G. Perez-Landa, J.J. Dieguez, V. Oedegaard, G. Bonafe, S. Jongen, A. Rasmussen, B. Amstrup, A. Baklanov, U. Damrath (2005) Evaluation and inter-comparison of operational mesoscale models for FUMAPEX target cities. FUMAPEX Report D3.4, DWD, Offenbach, Germany, 110pp.

Fay, B., Neunhäuserer, L., Glaab, H. (2005). Results of first urbanisation steps in LM and application of very high-resolution LM simulations to air pollution models in selected air pollution episodes. In J. Steppeler (editor):6th Int. SRNWP-workshop on non-hydrostatic modelling abstracts (Bad Orb 31 Oct-2Nov 2005), DWD, Offenbach.

Fay, B. and L. Neunhäuserer (2005a) Performance of DWD Mixing Height Scheme for LM applications on the urban scale. In Finardi S. (editor), FUMAPEX report D5.4, ARIANET, Milano, Italy, pp 1-14.

Fay, B. and L. Neunhäuserer (2005b) Evaluation of very high-resolution simulations with the non-hydrostatic numerical weather prediction model Lokalmodell for urban air pollution episodes in Helsinki, Oslo and Valencia. Atm. Chem. and Phys. Discussions, 5, 8233-8284, 2005, www.atmos-chem-phys.org/acpd/5/8233/

Neunhäuserer, L., Fay, B., Raschendorfer, M. (2006) Towards urbanisation of the non-hydrostatic numerical weather prediction model Lokalmodell (LM). Submitted to Bound. Layer Met, Jan 2006.

Ødegård, V. (editor), A. D'Allura, A. Baklanov, J. J. Diéguez, B. Fay, S. Finardi, H. Glaab, S.C. Hoe, M. Millán, A. Mahura, L. Neunhäuserer, J.L. Palau, G. Perez, L.H. Slørdal, A. Stein, J.H. Sørensen (2005) Study of the sensitivity of UAP forecasts to meteorological input. FUMAPEX Report for D6.2, Oslo, Met.no, 101 p.

Wind Forecast Model Intercomparison for Wind Energy

Juan Ferreira*, Alfredo Rocha, José Castanheira, Carlos Marques and Paulo Melo-Gonçalves
Departament of Physics, University of Aveiro, Campus Universitário de Santiago, 3810-193 Aveiro, Portugal
*juan@fis.ua.pt

Introduction

The main purpose of this project is to predict wind speed in a region were it is settled an eolic power plant. In the University of Aveiro there are two models (MM5 and WRF), one of them (WRF) with three different configurations, running in operational mode for Portugal and Iberian Peninsula weather prediction. Wind speed of these models were extracted and compared with observations of an automatic meteorological station.

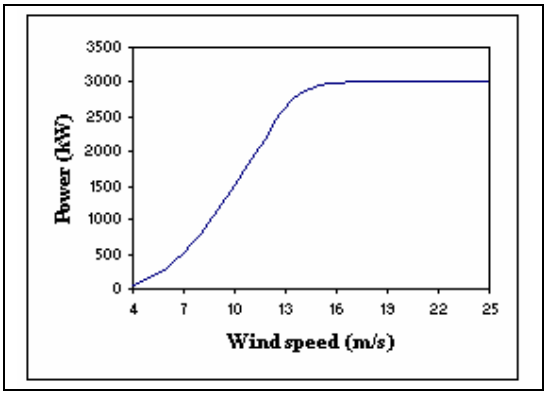

Figure 1- Power curve of an eolic generator

The use of this kind of information is very useful for the Portuguese company of electricity distribution, once, by law, they are obligated to buy all the electric energy that is produced by means of renewable sources. The previous knowledge of the amount of power produced by eolic source permits to manage the amount of energy to buy to the non-renewable power plants.

One of the problems in predicting wind for eolic power plants arises from the location were they are settled, usually in very complex orography regions. Hence, high spatial resolution models are needed to better represent the orographic effects in the results. Other problem comes from the characteristics of the eolic generators. The power produced depends non-linearly on the wind speed, in a wide range of wind speed values (an example of this dependence is shown in figure 1).

Methodology and Results

To evaluate the better way to forecast wind speed in the power plant location, the results of the models and configurations that were already in use for weather prediction at Portugal were considered. Additionally, the WRF model was configured to run with a higher spatial resolution than the operational models. A description of the characteristics of each model is summarized in table 1.

Table 1- Used models

Designation	Model	Version	Finest Grid Resolution (Km)
wrf1	WRF	1.0	20
wrf2	WRF	2.0	10
wrf3	WRF	2.1	3
wrf4	WRF	2.1	12
mm5	MM5	3.0	9

The simulations were carried out in the period between 13th to 17th October of 2005, in 48 hours forecasts.

Wind observations from the automatic meteorological station located at Aveiro were used to assess the quality of the forecasts.

The results shown in figure 2 are comparisons of three 48 hours forecasts of each model in table 1 with observations. The color code of figure 2 is the following: wrf1 – blue, wrf2 – green, wrf3 – red, wrf4 – magenta, mm5 – light blue, mean of the models – black line with

open circles, observations – blue line with open circles.

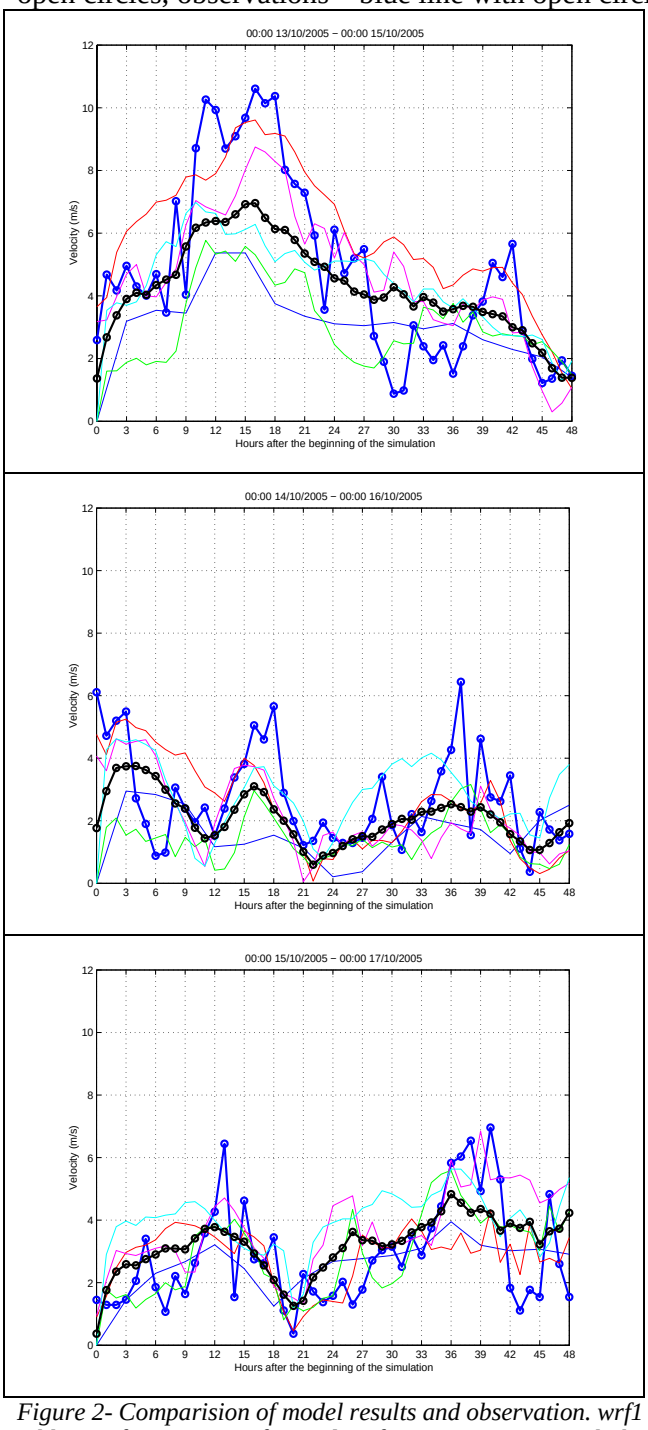

Figure 2- Comparision of model results and observation. wrf1 – blue, wrf2 – green, wrf3 – red, wrf4 – magenta, mm5 – light blue, mean of the models – black line with open circles, observations – blue line with open circles

These initial results suggest the following remarks:

- All models seems to reproduce the general behaviour of the observations.
- It appears that the most recent version of the WRF model has the best performance.
- Forecasts are worst for low wind speed values. However, the eolic potential is negligible for low wind speed.

From the dispersion of these forecasts, it seems preferably the use of an ensemble approach, which would permit to build confidence intervals for the electric power forecast production.

Aknwolodgments

The authors would like to aknwoledge Dr. Yoshihiro Yamazaki for the results of the wrf1, wrf4 and mm5 models and Dr. Maria Manzo Orgaz for the wind observation data at Aveiro.

Sensitivity of Leaf Area Index in Florida to Temperature Simulation by FSURSM

Yoshie Goto, D.W. Shin and James J. O'Brien
Center for Ocean-Atmospheric Prediction Studies, Florida State University, Tallahassee, FL, USA
(yoshie@coaps.fsu.edu)

Land surface simulation is an important factor for atmospheric models, while precise estimates of land-use and vegetation are still in progress. This research is to investigate the sensitivity of leaf area index (LAI) in the southeast United States to FSURSM (Florida State University Regional Spectral Model) (Cocke and LaRow, 2000) coupled with CLM2 (Community Land Model 2.0) and improvement of the model with a new dataset of LAI in 2001 based on satellite observation by MODIS (Moderate Resolution Imaging Spectroradiometer) (Myneni et al., 2002).

According to a previous study, the FSURSM coupled with CLM2 in the domain of southeast U.S. has a cold bias of about 2 ℃ in the Florida region, although it was highly improved from the original FSURSM without CLM2 especially in the inland part of the domain (Shin et al., 2006). The CLM2 is mainly built for global models, although the FSURSM uses CLM2 to calculate land surface condition of a smaller domain at a higher resolution. Therefore, the vegetation data (0.5° grid) in CLM2 which is interpolated from 200km grid data accumulated by 1km data to make the data spatially smooth could cause a significant error for regional models. Figure 1 shows (a) monthly climatological LAI of the CLM2 in August and (b) monthly LAI of MODIS in August 2001. The LAI in CLM2 has lower values in Florida peninsula than that of the MODIS LAI. Since larger LAI leads lower albedo which can result in more absorption of solar energy, the model has a possibility to have higher temperatures, when the original LAI is substituted with the new observation. Another problem of the low LAI is that vegetated area in CLM2 is obtained as area where is neither lake nor wetland and vegetation in wetland are not counted for vegetation. According to the prescribed land-use data in CLM2, more than 30% of the southern part of Florida is wetland without vegetation. Thus, the effect of LAI in CLM2 appears essentially less in the southern Florida.

For the experiment, the southeast US region at 20km resolution in March to September, 2001 is simulated using FSURSM with the adjusted LAI by MODIS. Atmospheric boundary conditions are provided from simulation by FSUGSM (Florida State University Global Spectral Model). The new LAI dataset is adjusted with the ratio of vegetated area based on the land-use data in CLM2, and difference between the prescribed monthly CLM2 LAI at 20km resolution and monthly MODIS LAI at 0.25° resolution is distributed to the original prescribed LAI of deciduous trees and grass. Although CLM2 changes LAI dependent on snow depth, no snow cover in Southeast U.S. was assumed for the adjustment of the new LAI because our main interest is in Florida where snow depth is negligible. While the prescribed monthly LAI in CLM2 is based on NDVI (Normalized Difference Vegetation Index) by AVHRR (Advanced Very High Resolution Radiometer) from 1981 to 1991 (Bonan et al., 2002) and the MODIS started in 2000, changes in land-use are ignored in the new dataset, because the original low LAI values in southern Florida implies that lower vegetation was already estimated in the region.

A possible problem about the substitution is inconsistency of land-use data and new LAI. The prescribed LAI data at each grid in CLM2 is divided into up to four categories by the largest four PFT (Plant Functional Type) categories, while the MODIS LAI have only one value for each grid. However, since newer land-use and vegetation data was not available yet, the original data in CLM2 are used.

Figure 2 shows discrepancy between new and original models on (a) minimum temperature and (b) maximum temperature. In the southern Florida, results show higher values in both minimum and maximum temperature throughout the period (Not shown). The discrepancy of temperature between the observation and the modeled value is not fully compensated yet, but this result suggests that low LAI in prescribed data was one of the causes of the cold bias in Florida peninsula. For this experiment, relatively new LAI is used under the original land-use and PFT type data, which are possible to be inconsistent with the new LAI observation. For the future research, new LAI dataset based on newer land-use data and substitution of other surface data will be necessary to improve the model.

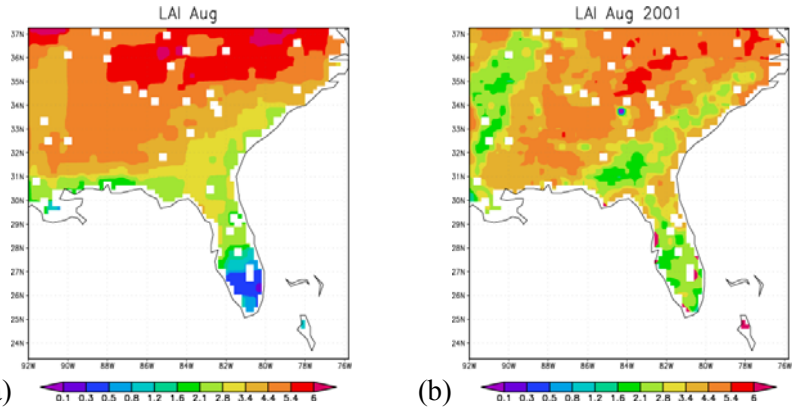

Fig 1. LAI in Southeast United States: (a) prescribed LAI of CLM2 in August and (b) MODIS observed LAI in August, 2001.

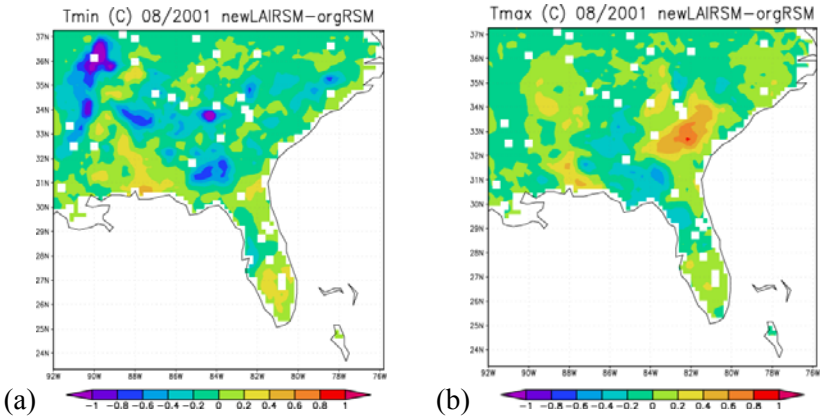

Fig 2. Difference between calculated temperatures by FSURSM coupled with CLM2 with prescribed LAI and that with MODIS LAI in August, 2001 in southeast United States: (a) minimum temperature and (b) maximum temperature.

Acknowledgement

The computations were performed on the IBM SP4 at Florida State University. COAPS receives its support from Applied Research Center, funded by NOAA office of Global Programs awarded to Dr. James J. O'Brien.

References

Bonan, Gordon B., Keith W. Oleson, Mariana Vertenstein, Samuel Levis, Xubin Zeng, Yongjiu Dai, Robert E. Dickinson and Zong-Liang Yang, 2002: The Land Surface Climatology of the Community Land Model Coupled to the NCAR Community Climate Model. *Journal of Climate*: Vol. 15, No. 22, pp. 3123–3149.

Cocke, S and T. E. LaRow. 2000: Seasonal Predictions Using a Regional Spectral Model Embedded within a Coupled Ocean–Atmosphere Model. *Monthly Weather Review*, 128, 689–708.

Myneni, R. B., et al. 2002: Global products of vegetation leaf area and fraction absorbed PAR from year one of MODIS data, *Remote Sens. Environ.*, 83, 214– 231.

Shin, D. W., J. G. Bellow, T. E. Larow, S. Cocke, and J. J. O'Brien, 2006: The Role of an Advanced Land Model in Seasonal Dynamical Downscaling for Crop Model Application. *J. Appl. Meteor.* (in press)

The impact of model resolution on hurricane forecasts

Glenn Greed (Met Office, UK)
Contact: glenn.greed@metoffice.gov.uk

The resolution of operational global NWP forecast models continues to increase alongside the availability of computer resources. In this report we consider the impact of further enhanced model resolution on forecasting extreme weather events such as hurricanes.

Prior to the start of the 2005 Atlantic hurricane season, a North American limited area model (NAM) was built to investigate whether a 17km, 38 level version of the Unified Model could provide improved forecast tracks and depths of hurricanes. By comparison the UK Met Office global model at the time was of resolution 0.83°x0.55°[1]; approximately 90km in the tropics and 60km in mid-latitudes with 38 levels. The NAM includes data assimilation (3DVAR) of all appropriate observations: Satellite, Sonde, Surface and Aireps, while the operational global model uses a superior 4DVAR scheme. Bogus observations applied to the UK Met Office global model are also applied to the NAM.

The NAM was run in real-time for the periods 24th-30th Aug 2005 and 21st-25th September 2005 during Hurricanes Katrina and Rita. Two 36-hour forecasts per day were produced, at 00z and 12z. *Resource availability prohibited NAM from running for the entire hurricane season.*

Table 1 presents the mean forecast track error from a sample of 17 forecast runs[2]. Overall, an enhanced resolution of 17km does not improve the forecast track.

Table 1: Average forecast tack error from observed track.

	T+0	T+12	T+24	T+36
Global	25km	51km	85km	117km
NAM	26km	45km	90km	121km

The track errors are similar; however there are some noticeable differences in the forecast tracks depicted in **figure 1**. For example, the global model tended to recurve Katrina too soon. Tracks from the NAM were generally to the left of those from the global model. Once Katrina became established in the Gulf of Mexico both models provided good guidance.

Unsurprisingly where enhanced resolution has a clear positive impact is in its ability to resolve deeper central pressures and stronger sustained wind speeds. For example, at 12z 29th Aug Katrina's observed pressure, near landfall, was 923mb with 110kt winds. The previous NAM forecasts valid at this time were fairly consistent: T+36 (959mb, 60kts), T+24 (962mb, 60kts) and T+12 (958mb, 62kts) **figure 2**. The corresponding global forecasts gave: T+36 (986mb, 40kts), T+24 (986mb, 39kts) and T+12 (979mb, 46kts). Observations of Rita, near landfall, at 00z 24th Sep, gave 931mb with 105kt winds. At this time the validating NAM forecasts were: T+36 (967mb, 61kts), T+24 (958mb, 68kts) and T+12 (974mb, 51kts), while the global model yielded: T+36 (990mb, 41kts), T+24 (988mb, 41kts) and T+12 (985mb, 41kts).

Enhanced resolution also yields higher precipitation totals and begins to resolve rain bands within the hurricanes matching better qualitatively with satellite and radar imagery. When Katrina made landfall, the NAM, 12z 29th Aug T+0 to T+3, forecast further intensified rainfall accumulations (**figure 3**) exceeding 128mm for the 3 hour period 12z-15z, highlighting a major rainfall event. Available station observations do not support such extreme totals in a 3hr period. For example, Newton MS, further inland, saw rain rates >25mm/hr for 3 consecutive hours later in the day, but these totalled less than 100mm. *Aside: The New Orleans Radar at 13z was registering reflectivity's between 45-50DBZ. This corresponds to rain rates of between 50 and 150mm/hr, with the Rosenfeld Tropical Z-R relationship.*

[1] The UK Met Office global model resolution was recently increased to 0.56°x 0.37° x 50 levels, on 13th Dec 2005.
[2] Forecast sample includes 00z 25th-12z 29th Aug and 00z 21st-00z 24th Sep 2005 inclusive.

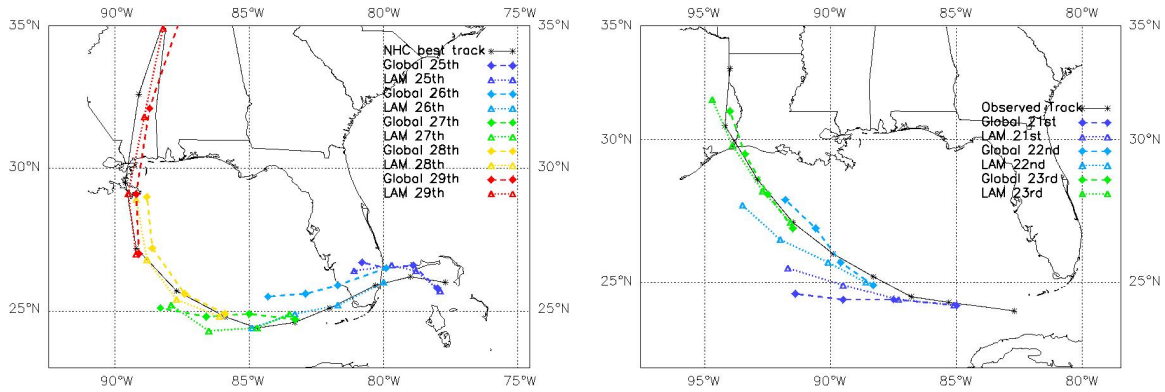

Figure 1: Daily short range T+0→T+36 forecast tracks of Katrina, 00z forecasts (left) and Rita 12z forecasts (right), comparing the global model (dashed lines) and NAM (dotted lines) with the NHC best track (solid line).

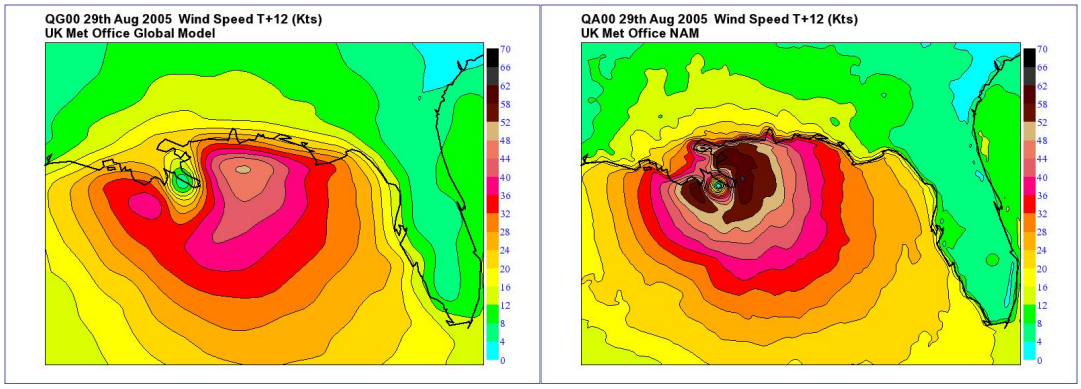

Figure 2: 00z 29th Aug 2005 T+12 forecast wind speed, global (left) and NAM (right). Observed max was 150kts.

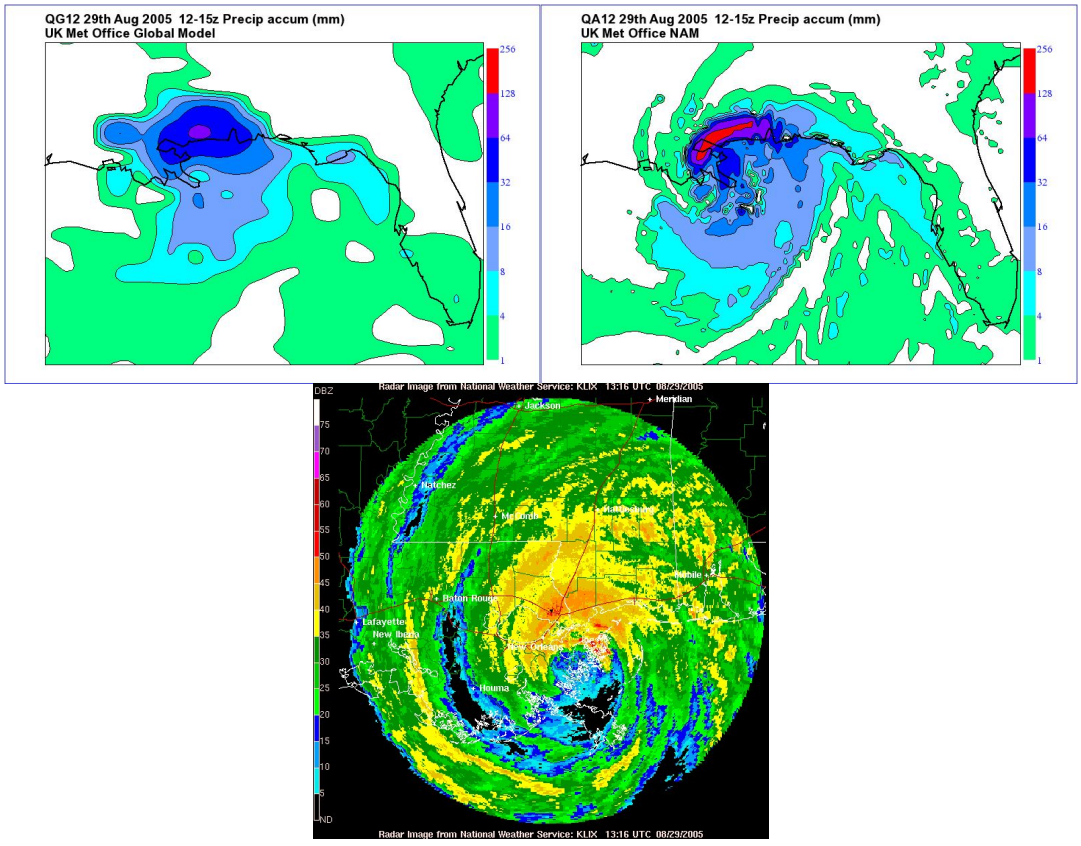

Figure 3: 3hr Precipitation accumulations 12z-15z 29Aug 2005, global (top left) max 67mm, NAM (top right) max 187mm and the New Orleans radar (c/o NOAA NWS, bottom) at 13z.

Budget analysis of absolute vorticity, simulated by a nonhydrostatic model, for the maintenance mechanisms of the intensity of Typhoon SONGDA (T0418) under traveling over the Sea of Japan

Teruyuki KATO*

*Meteorological Research Institute / Japan Meteorological Agency, 1-1 Nagamine, Tsukuba, Ibaraki 305-0052, Japan

In 2004, ten typhoons landed on the Japan Islands. Among them, Typhoon SONGA (T0418) maintained its strong winds until approaching Hokkaido Island through the Sea of Japan, and caused serious disasters there. Warm sea surface temperature (*SST*) is necessary for the maintenance of the intensity of typhoons. However, when typhoons travel over the northern Sea of Japan with the cool *SST* (< 24 ^{o}C), the supply of water vapor from the sea rapidly decreases and consequently typhoons cannot maintain their intensity. On the other hands, some typhoons receive such an influence of westerly waves as the baroclinic instability and the inflow of upper-level high potential vorticity (*PV)*, and redevelop as an extratropical cyclone. In this study, the maintenance mechanisms of the intensity of T0418 under traveling over the Sea of Japan are examined from the budget analysis of absolute vorticity ζ_a, by using the Japan-Meteorological-Agency (JMA) nonhydrostatic model with a horizontal grid of 5km (5km-NHM) and focusing on the inflow of upper-level high PV.

The 345K-isentropic*PV* field (Fig. 1) shows that the high *PV* lager then 8 PVU is found around the center of T0418 that traveled over the Sea of Japan. Another anomaly of high *PV* (2-4 PVU) flowed from the southwest toward the center of T0418. This area corresponded to the dark region with high brightness temperature in the infrared image observed by meteorological satellite, and it also corresponded to the down-motion region because the height shown in Fig. 1 deceases toward T0418. The inflow of high *PV* was found remarkably at the height of 7-9 km. Therefore, this high PV inflow could exert an influence on the maintenance of the intensity of T0418.

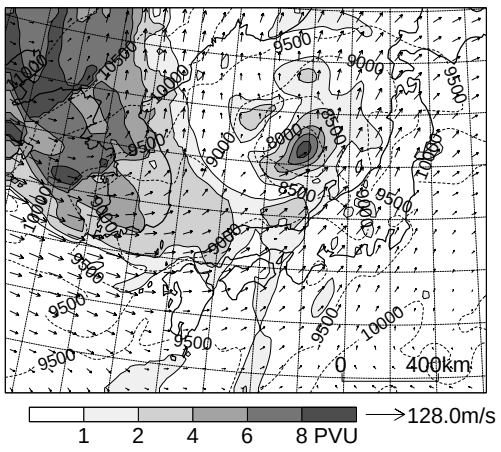

Fig. 1 345K-isentropic potential vorticity and wind vector field depicted by the JMA regional analysis at 21JST 07 September 2004. Broken lines show the heights.

The initial conditions of 5km-NHM are produced from the JMA regional and mesoscale analyses (ranal and manal) at 21 JST (= UTC + 9 h) on 07 September, and its boundaries are given from the forecast of the JMA regional spectral model. Bulk-type microphysics with the ice phase are used in conjunction with the Kain-Fritsch convective parameterization scheme. The increase of the central pressure of T0418, analyzed by the JMA, is not found in the simulation results (Fig. 2a). The simulations indicate that T0418 approached Hokkaido Island maintaining its intensity. Hereafter, the results from the ranal are used, because the simulated Typhoon Track is closer to the JMA analysis (Fig. 2b).

A sensitive experiment without precipitation

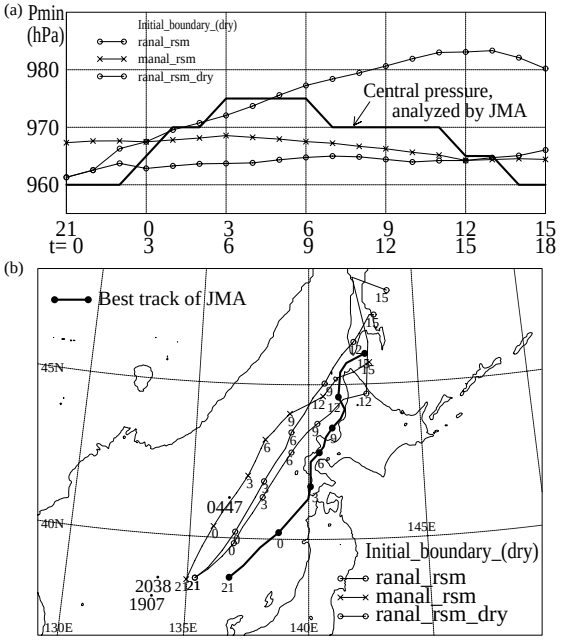

Fig.2 (a) Minimum sea-surface pressure and (b) analyzed and simulated central position of T0418. The dots with 4 numbers (time) show the potions of the center of T0418 estimated by satellite data.

process (*DRY*) is conducted to examine the effect of moist convection on the maintenance of the intensity of T0418. The results (Fig. 2a) show that the intensity of T0418 continuously decays, and its central pressure increases by about 20 hPa in comparison with that of *CNTL*. This indicates that convective activities are necessary for the maintenance of the intensity of T0418 even under the effect of westerly waves.

ζ_a is defined as

$$\zeta_a = \frac{\partial v}{\partial x} - \frac{\partial u}{\partial y} + f \quad , \qquad (1)$$

where f is Coriolis parameter. The time difference of ζ_a is obtained from (1) as

$$\frac{\partial \zeta_a}{\partial t} = -\mathbf{v}_h \nabla_h \zeta_a - w\frac{\partial \zeta_a}{\partial z} - \zeta_a\left(\frac{\partial u}{\partial x} + \frac{\partial v}{\partial y}\right) - \left(\frac{\partial w}{\partial x}\frac{\partial v}{\partial z} - \frac{\partial w}{\partial y}\frac{\partial u}{\partial z}\right) \quad . \qquad (2)$$

Here, the 1st , 2nd, 3rd and 4th terms of the right hand side (*RHS*) of (2) mean the horizontal and vertical advections, divergence and tilting, respectively. The divergence and tilting terms present the extension / pressure of vertical vorticity in a vertical direction, and the change from horizontal vorticity to vertical one, respectively. The budget of (2) calculated from the results of 5km-NHM are analyzed. Noted that they are averaged in the horizontal scale of 400 km to exclude the influence of vorticity with the convective scale.

The vertical profile of the time change of ζ_a around the center of T0418 (Fig. 3a) shows that the maximum of ζ_a, located at a height of 2 km in the initial condition, slightly decreases until t = 2 h, and then it increases with the 1-km drop of its height. This indicates that, since the vertical structure of T0418 considerably changes within t = 4 h, T0418 decays as a typhoon but develops as an extratropical cyclone. In the *DRY* experiment (Fig. 3b), the maximum of ζ_a monotonously decreases until t = 15 h. This corresponds to the decay of the intensity of T0418 in the case without precipitation process.

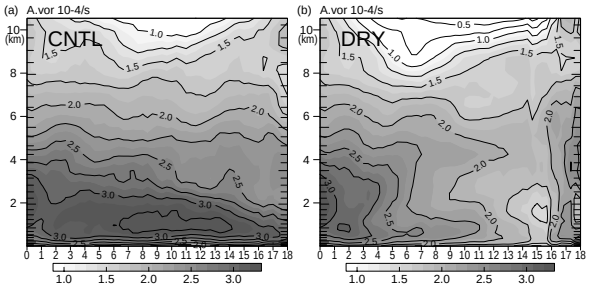

Fig. 3 Time-height cross section of absolute vorticity around the center of T0418, averaged in the horizontal scale of 400km, simulated by 5km-NHM in (a) *CNTL* and (b) *DRY* experiments.

The budget analyses of ζ_a, averaged for 3 hours around the period when the structure of T0418 changes, are shown in Fig. 4. Before the structure of T0418 changes (Fig. 4a), the amplitudes of all terms in the *RHS* of (2) are very small above a height of 6 km. Below that height, the divergence and vertical advection terms cancel each other out, and the intensity of ζ_a is maintained almost by these two terms. The divergence term is rewritten in the use of continuity equation as

$$-\zeta_a\left(\frac{\partial u}{\partial x} + \frac{\partial v}{\partial y}\right) = \zeta_a \frac{\partial w}{\partial z} \quad . \qquad (3)$$

Therefore, both the divergence and vertical advection terms can be estimated by one-dimensional (vertical) profile of ζ_a and w. This means that the vertical structure of T0418 is determined mainly by convective activities, which produce vertical motions in typhoons, before it changes.

After the structure of T0418 changes (Fig. 4b), the profile of each term of the *RHS* of (2) becomes complicated, and its amplitude increases above a height of 6 km, but for the horizontal advection term. This shows that upper-level atmosphere exert a significant influence on the maintenance of the intensity of T0418, in addition to convective activities.

Vorticity in a high *PV* air that flows into T0418 is extended vertically, and consequently ζ_a is enhanced around the height of 5 - 9 km. This enhancement cancels out the decrease of ζ_a that is caused by weaken convective activities due to cool *SST*, and it maintains the intensity of T0418.

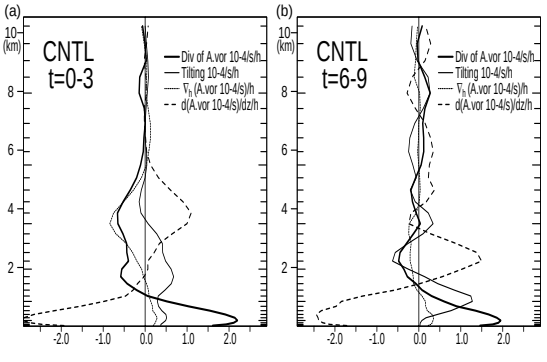

Fig. 4 Budget analyses of absolute vorticity averaged during (a) t = 0 - 3 h and (c) t = 6 - 9 h, simulated by 5km-NHM. Bold, thin, dotted and broken lines denote the horizontal and vertical advection, divergence and tilting terms, respectively

Coupling of WRF and AERMOD for Air Quality Modeling over Pune city

Amit Kesarkar*[1], Mohit Dalvi[1], Ajay Ojha[2], A. Venkatram[3], A. Cimorelli[4], Akshara Kaginalkar[1]

1) Centre for Development of Advanced Computing (C-DAC), Pune, India
2) Air Quality Management Cell, Pune Municipal Corporation (PMC), Pune, India
3) Dept. of Mechanical Engg., University of California at Riverside, CA, USA
4) EPA (Region –III) Office, Philadelphia, PA, USA

Introduction: Air Quality Modeling is an essential component of any urban air quality management program and is responsible for design and implementation of control strategies. Indian Ministry of Environment & Forests and the United States Environment Protection Agency (USEPA) along with Pune city's local government body have initiated urban air quality improvement initiatives. These initiatives include air quality monitoring, emission data generation and development of air quality modeling system. Gaussian air pollutant dispersion model AERMOD of USEPA is used for a simplistic demonstration of this system. AERMOD requires hourly surface and upper air meteorological observations. In the absence of meteorological observations at an hourly interval, the use of regional model derived meteorological parameters is well suited. Weather Research and Forecasting model (WRF) Version 2.0.3.1 developed by National Centre for Atmospheric Research (NCAR) has been used to obtain the micro-meteorological parameters necessary for AERMOD to simulate dispersion of PM10 over Pune city.

Experiments: The AQM system is used for a test case simulation dispersion of PM10 over Pune city. The emissions data and air quality monitoring data for the duration of 14 – 17 April 2005 is used The computational domain of 89 X 123 X 31 grid points with the horizontal resolution of 10 km is chosen for the WRF model so as to cover the south-western part of India, ranging from 72^0 E to 78^0 E in longitude and 8^0 N to 20^0 N in latitudes. The model is initialized by NCAR-NCEP's Final Analysis (FNL) data. A coupler for WRF-AERMOD linkage is developed for carrying out this simulation. The coupler derives planetary boundary layer parameters for given location from WRF model output and creates the direct AERMOD meteorological input file without the use of AERMET (AERMOD preprocessor) and thus making provision for observational data requirement.

Results and Discussions: The comparison of WRF model output and surface meteorological observations derived from NCAR's ADP dataset for Pune are presented in Figures 1 & 2. The angular distribution of wind directions simulated by WRF is consistent with the observations. Since observational data has recorded wind directions in 8 sectors, it represents southerly and easterly winds. The comparison of simulated and observed surface temperatures at Pune are in phase and having maximum deviation (Fig 2) of about 2^0 C. Comparison of AERMOD output with monitored air quality values at two different locations in Pune city are depicted in Figure-4. The output of AERMOD does not include the 'background' concentrations (i.e. basic levels in absence of any emissions) and hence accurate comparison is not possible at this stage. However, the simulated daily variations in the ambient AQ values seem to be fairly well reproduced by the model. Currently, to improve the predictability of this system, emission inventory input along with sensitivity analysis of AERMOD to different WRF settings is being modified.

* Corresponding Author. Email: akesarkar@cdac.in

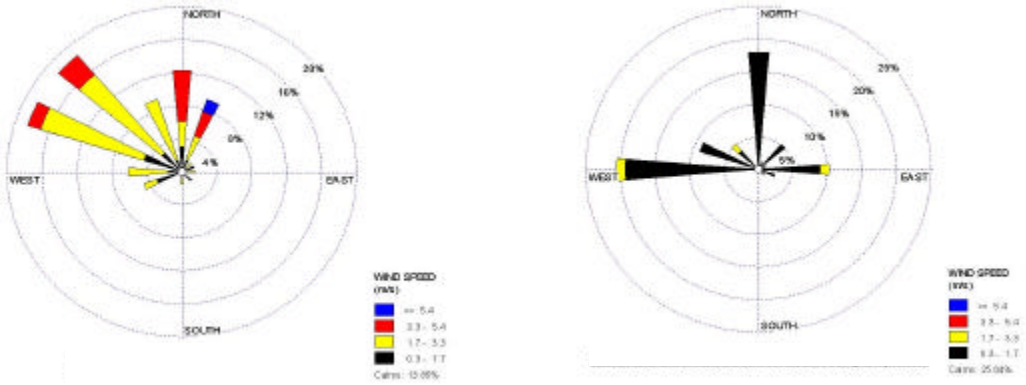

Figure-1: Wind roses derived from WRF output (left) and NCAR ADP data for Pune (10-19th April 2005).

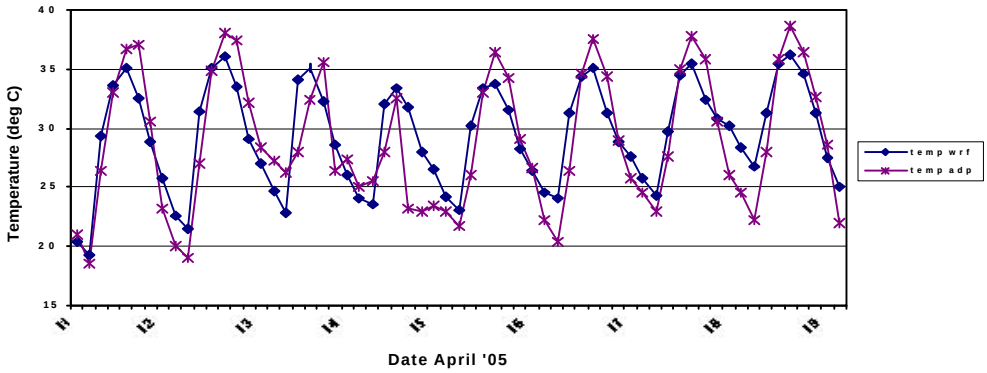

Figure-2: Comparison of Temperatures at surface (^{0}C) from WRF output (blue line) and observations from NCAR-ADP data (pink) for Pune city at IMD observatory location during 10-19th April 2005

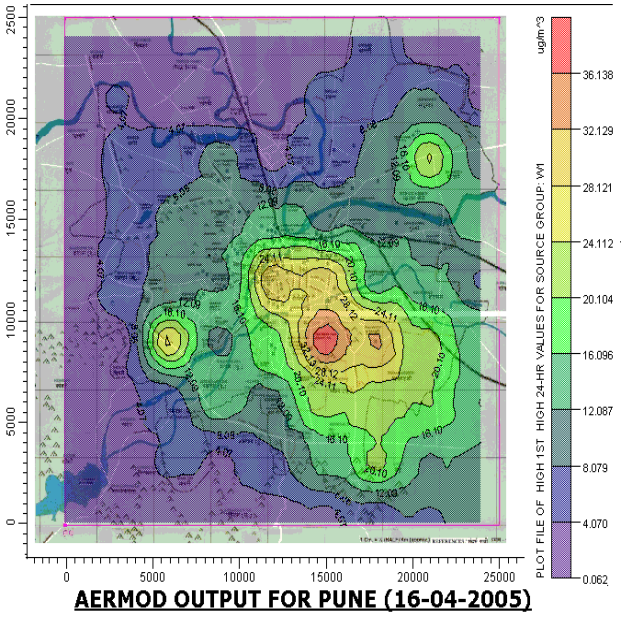

Figure-3 : Sample output from AERMOD simulation for PM10 over Pune city (14-17th April 2005)

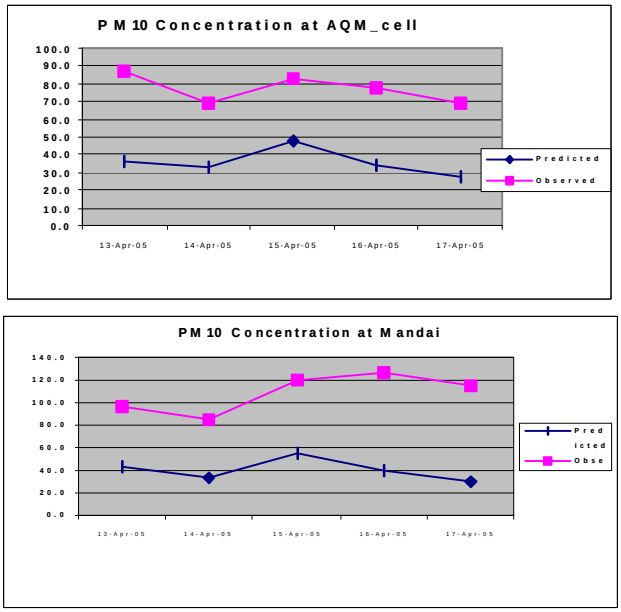

Figure-4: Comparison of Daily Model outputs (blue) with observed values at two locations in Pune city

Prototype of Real Time Weather System at C-DAC

Amit P Kesarkar and Akshara Kaginalkar
CAS, SECG, C-DAC, Pune University Campus, Ganesh Khind, Pune 411007, India
e-mail: akesarkar@cdac.in

Introduction: The complexity in the observed hazardous weather such as flash flooding due to mesoscale cyclones, evolution of tropical cyclones and urban pollution require high-resolution model simulations. This in turn leads to increase in the complexity in the formulation of the atmospheric models and data assimilation systems. The study of mesoscale convective systems, evolution of deep convection in maritime atmosphere, need temporal integration of atmospheric models for longer durations with finer temporal resolutions. To forecast real time weather at mesoscale resolution require sophisticated end to end computational workflow and forecast dissemination system.

Real Time Weather System: Real Time Weather System (RTWS) presented in this paper addresses the demands of research and operational scientists through a fully automated, flexible, portable; standalone/ web based service-oriented architecture capable of predicting weather events and assisting in research. The computational workflow endorses plug-in-play type of system portable on any Unix flavored platforms. The automated workflow is designed with the objective of providing a real time weather forecasting environment facilitating the user with data handling, data query, data analysis, perform need based modeling, model output post-processing, model output statistics and data visualization services through a Graphical User Interface (API) / Web Interface. The user can select combination of General Circulation Models (GCM), the regional model, platform to execute the models, data format types and visualization software. The multi layer web service architecture provides the user access to Meta data catalog system and query system for meteorological data and parameters. In this case study, based on the software architecture as described in Fig (1) and (2), computational workflow is developed using NCEP GCM (T170 / T254) and WRF model using C-DAC's supercomputer PARAM PADMA. The table 1 describe model configuration and initialization.

Daily 72 hrs NWP Forecast Products:

- Surface: Precipitation Rate(mm hr^{-1}), Daily Precipitation at 0300 UTC (mm day^{-1}), Sea level Pressure (Pa);
- Upper air
  at Surface, 1000, 0850, 0700, 0500, 0300 and 0200 hPa: Pressure Level Height (m), Dry Bulb Temperature (^oC), Dew Point Depression (^oC), Potential Temperature (^oC), Horizontal Winds (Kts), Vertical Velocity of Wind (meter s^{-1}), Vorticity (s^{-1}), Relative Humidity (%)
  at 0500, 0300, 0200hPa: Upper tropospheric Divergence (s^{-1})

Further Improvements and Developments:

- Incorporation of
  global model: Community Atmosphere Model, Portable Unified Model
  regional atmospheric models: MM5, RAMS, Eta, RSM
- Tailor made approach in model simulations and data visualization for different categories of user communities such as aviation community, agricultural community
- Grid computing for real time forecast, data grid and model coupling using application grid

Table 1: Present model Configuration and Initialization

Model Settings	**Specifications**
Domain	Indian Subcontinent, 40 E – 100 E / 10 S – 45 N; 278 X 255 X 42 grid
Resolution	24 km grid length, 42 vertical levels, 60 sec time step
Initialization and computation of lateral boundary conditions	3 hourly boundary conditions using NCEP GFS system forecast (00Z analysis) 3 hourly boundary conditions using T170 L 42 forecasts (70 km X 70 km) (18 Z NCEP operational analysis)
Objective Analysis	3D Var, FSL-RAOB data / can be made available using GTS data (irregular observations) (Assimilation cycle 6 hourly)
Physics Options Regional Model: WRF version 2.1.1.1 (presently used)	Microphysics: Purdue Lin Scheme Cumulus Parameterization: Kain Fritsch (new, KF-eta) Surface Layer: Similarity (Janjic, 2002) Land Surface Model: Noah LSM Planetary Boundary Layer: Yonsei University Radiation: long wave: RRTM Radiation: short wave: Dudhia
Forecast Duration	72 hours, hourly output
Validation	NCAR FNL Analysis and actual observations

Fig. 1

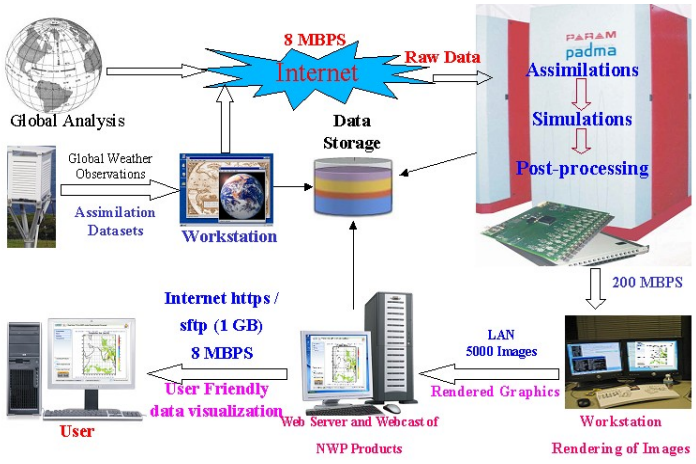

Fig. 2

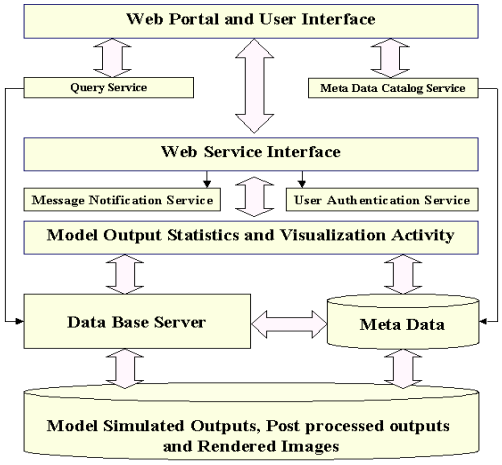

Fig. 3

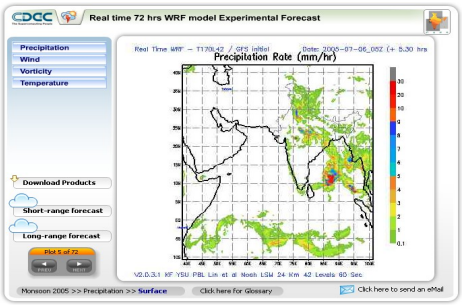

Fig 1: System architecture of RTWS

Fig 2: Web Service Architecture of RTWS

Fig 3:Screen shot of web portal prototype of RTWS using WRF

Physical initialization for mesoscale weather prediction

T.N. Krishnamurti, D.V. Bhaskar Rao and S. Pattnaik
Department of Meteorology
Florida State University, Tallahassee, FL., 32306, USA
Email :<tnk@io.met.fsu.edu>,<brao@met.fsu.edu>,<spt@met.fsu.edu>

A method of physical initialization for large scale models was proposed by Krishnamurti et al (1991) and its impact on the weather prediction was well established. Based on this concept, a method of physical initialization for mesoscale models is proposed. The bases for this procedure is that the rainfall predicted through a cumulus parameterization scheme used in the model is sensitive to moist static stability and so the vertical humidity distribution and the initial humidity vertical profiles have uncertainty and could be calibrated to have a close match between the model rain and the observations. The rain rate initialization is implemented for a pre-forecast period of 24 hours. Satellite rainfall estimates are collected for this period and interpolated to each grid point of the model domain and for each time step of the model integration. The model vertical humidity profile at a grid point is perturbed with a factor, depending on a sloping angle, in the atmospheric layer from surface to about 500 hPa. The induced perturbations will be such that they are positive (negative) in the lower half and negative (positive) in the upper half. The model produces rain rates through the cumulus scheme corresponding to each of the perturbations profiles and a vertical humidity profile which matches best with the observations is taken to continue further with the model process. Implementation of this procedure at each time of the model integration for a period of 24 hours show marked improvement in the prediction up to 48 hours.

The results from a monsoon rainfall prediction experiment with the rain rate physical initialization procedure are presented here (Figures 1 and 2). The results show significant improvements during the period of physical initialization and forecast period up to 48 hours. The model rainfall at Day0 (i.e.) end of the 24 hour pre-forecast physical initialization period is compared with the model rainfall without physical initialization and the TRMM estimates. The results clearly illustrate a better estimate of the model rains through implementation of physical initialization with a tendency towards observations where as uninitialized experiment show large deficiencies with underestimation of rainfall over most of the region (Fig. 1a, b and c), as evident from the equitable threat scores (Fig.1d). A 2-day forecast is carried out with the model initial conditions derived from the physical initialization and another without any initialization in the observations. A comparison of the predicted rainfall after 48 hours (Figure 2), illustrate that the model rainfall prediction with physical initialization is far improved as evident from the rainfall distributions (Fig. 2b and c) and the equitable threat scores (Fig. 2d). However, it is also noted that the impact of the physical initialization is marked for rainfall rates below 7-8 mm/hr, which is due to the implementation of the procedure for the cumulus parameterization part alone and not for the explicit rain process. Further studies towards the inclusion of explicit processes and nudging of atmospheric variables are under progress.

References:

Krishnamurti, T.N., J. Xue, H.S. Bedi, K. Ingles and D. Oosterhof, 1991: Physical initialization for numerical weather prediction over the tropics. *Tellus*, **43**, 53-81.

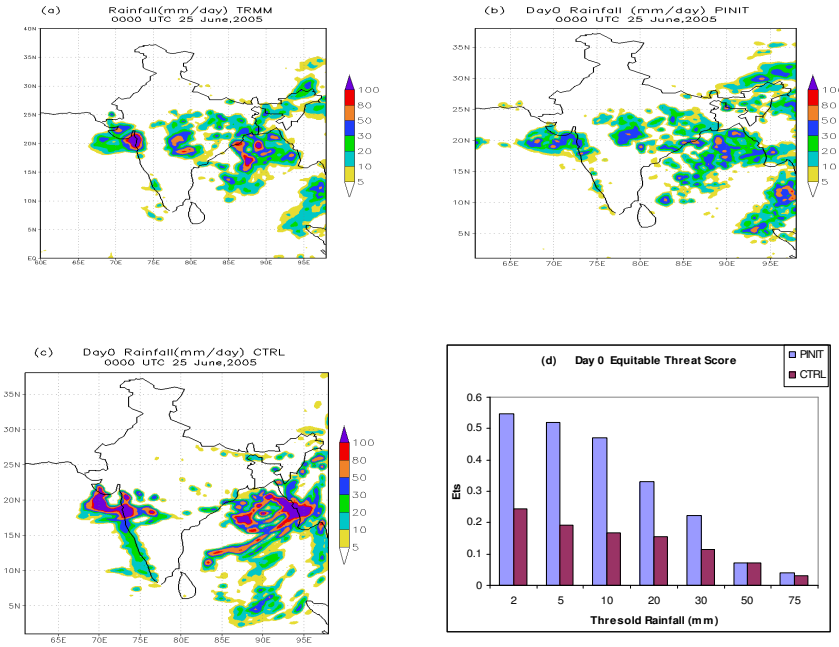

Figure 1 (a through d): Rainfall (mm/day) at Day0 (0000 UTC 25 June 2005) corresponding to (a)TRMM (b) Experiment with physical initialization (PINIT) (c) Control experiment without physical initialization (CTRL) and (d) Equitable threat scores for CTRL and PINIT experiments.

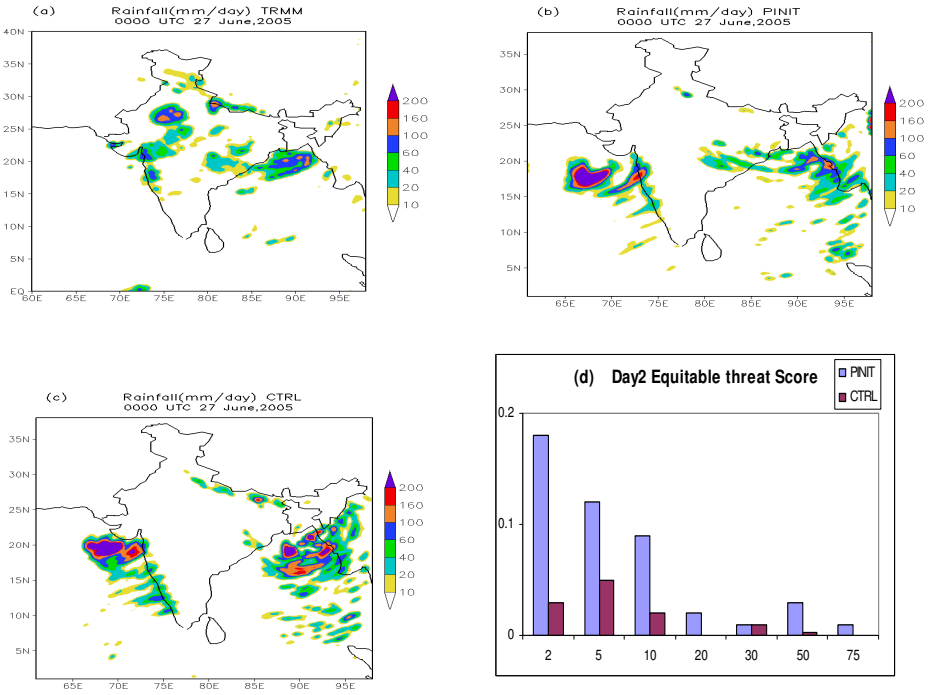

Figure 2 (a through d): Rainfall (mm/day) at Day2 (0000 UTC 27 June 2005) corresponding to (a) TRMM (b) Experiment with physical initialization (PINIT) (c) Control experiment without physical initialization (CTRL) and (d) Equitable threat scores for CTRL and PINIT experiments.

Statistical downscaling of the FSUGSM temperature over the southeast United States

Young-Kwon Lim, T. E. LaRow, James J. O'Brien, and D. W. Shin
Center for Ocean-Atmospheric Prediction Studies, Florida State University, Tallahassee, FL 32306-2840
(lim@coaps.fsu.edu)

The recent studies require the simulation of regional climate change scenarios with finer spatial and temporal resolution. Smaller scale prediction is very important in that the local climate significantly determines the consequences for many natural systems and human activities such as vegetation, ecology, hydrology, agriculture, economy, and urban development. Downscaling techniques have emerged as a means of providing this local climate change scenarios from coarsely resolved simulations that the current climate models are able to provide (Wilby and Wigley 1997; Huth and Kysely 2000). In addition, biases unveiled from the model result can be significantly reduced by the application of ideal downscaling technique. The present study has been motivated by this request. This study has focused on downscaling temperature of FSUGSM (Florida State University Global Spectral Model) (T63) seasonal forecasts, along with their bias-correction.

Five-day averaged maximum and minimum temperature data obtained from FSUGSM (~1.8° lon.-lat.) have been statistically downscaled to local spatial scale of 0.2°×0.2° (~20 km) for the southeast US region, covering Florida, Georgia, and Alabama. About 90 grid points are created by downscaling per FSUGSM grid box. Downscaling technique in this study comprises 1) CSFOF analysis (Kim and North 1997) between observation and FSUGSM output for the training period, 2) Regression between the dominant lower modes of each dataset. Observation is specified as predictand whereas the model result the predictor. 3) Generation of CSEOF principal component time series for forecast period on the basis of relationship identified from the first two steps. 4) Reconstruction of local scale data for the forecast domain from the generated principal component time series and the eigenfunctions obtained from training. 5) Repetition of this procedure by withholding a particular year as a forecast period in order to conduct this downscaling under the cross-validation framework. Figure 1 illustrates the basic downscaling procedure applied in the present study.

Downscaled results, FSUGSM simulations, and bias-corrected FSURSM (regional spectral model) are compared together with observations. 10 years from 1994 through 2003 have been used to compare those datasets and the time series of the last two years (2002 & 2003) are shown in Figs. 2 and 3. Time series show that statistically downscaled results are generally closer to observation than FSUGSM results are. This downscaling technique also corrects the bias which is included in FSUGSM. (e.g., Figs. 2c,d,e, Figs. 3a,b). However, statistically downscaled results look comparable to the dynamically downscaled RSM results, as their temporal fluctuations are shown in Figs. 2 and 3.

RMSE maps are provided here to compare the downscaling performance with RSM (Fig. 4). RMSE reveals that statistically downscaled results are moderately better than RSM results over Georgia and Alabama. However, Local climate in Florida is better captured by RSM simulation than statistical downscaling. We expect that the improved forecast skill with higher spatial grids will be very helpful for the near-surface local climate forecasts associated with anthropogenic urban impacts, agriculture and hydrology, and the geographical vegetation characteristics.

Acknowledgement
COAPS receives its base support from the Applied Research Center, funded by NOAA Office of Global Programs awarded to Dr. James J. O'Brien.

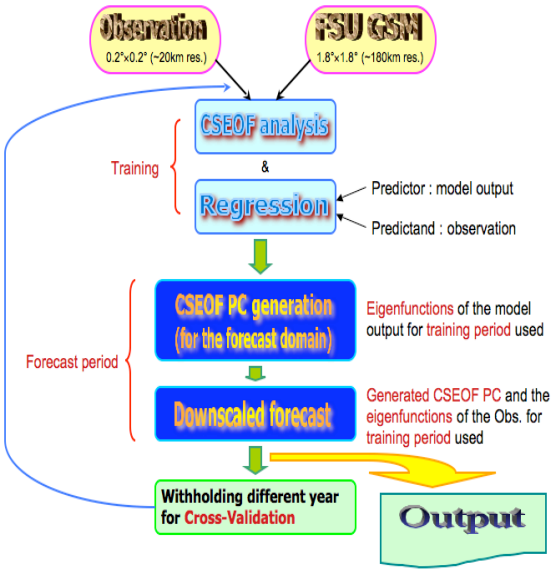

Fig. 1. Schematic diagram of the downscaling procedure in the present study

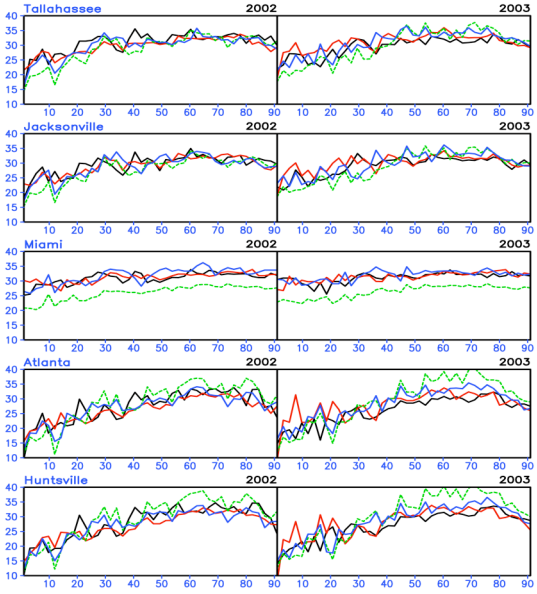

Fig. 2. 5-day mean surface T_{max} time series from downscaling (red), bias-corrected FSURSM (blue), FSUGSM (green-dashed), and observation (black).

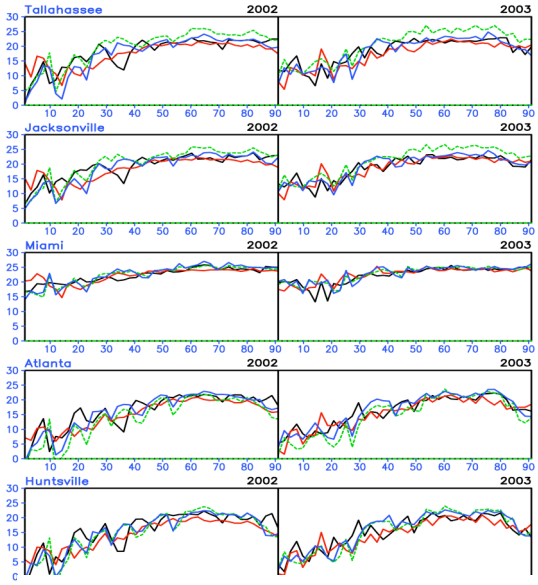

Fig. 3. Same as Fig. 2 but for T_{min}.

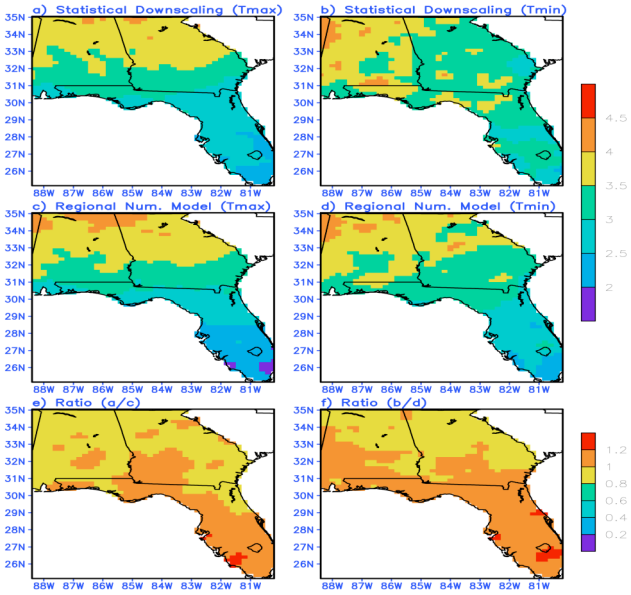

Fig. 4. RMSE maps for statistical downscaling (top) and RSM (middle). Bottom panel represents their RMSE ratio (downscaling/RSM). Left and right panels, respectively, indicate the map for T_{max} and T_{min}.

References

Kim, K.-Y., and G. North, 1997: EOFs of harmonizable cyclostationary processes. *J. Atmos. Sci.*, **54**, 2416-2427.

Wilby, R. L., and T. M. L. Wigley, 1997: Downscaling general circulation model output: a review of methods and limitations. *Progress in Physical Geography*, **21**, 530-548.

Huth, R., and J. Kysely, 2000: Constructing site-specific climate change scenarios on a monthly scale using statistical downscaling. *Theor. Appl. Climatol.*, **66**, 13-27.

High-resolution simulation of wind structure in the inner-core of Typhoon MA-ON (2004) and sensitivity experiments of horizontal resolution

Wataru Mashiko
Meteorological Research Institute, JMA, 1-1 Nagamine, Tsukuba, Ibaraki 305-0052, Japan
(E-mail : wmashiko@mri-jma.go.jp)

1. Introduction

The record-breaking number 10 of tropical cyclones made landfall on Japan in 2004 and caused a lot of damage throughout Japan due to strong winds, severe flooding, and storm surges. Among them, Typhoon MA-ON (2004) was characterized that it had strong winds in the left-rear quadrant during its passage over the southern portion of Kanto Plain. The primary purpose of the present study is to elucidate the structure and the generation mechanism of strong winds by using the high-resolution cloud resolving model. Moreover, sensitivity tests were conducted to study the impact of horizontal resolution of the numerical model on this event.

2. Characteristics of the strong winds observed during the passage of Typhoon MA-ON in the southern part of Kanto plain occupied by cold air at the low-level

On 9 October 2004, a strong typhoon MA-ON hit Izu peninsula in Eastern Japan and passed through the southern Kanto region. When MA-ON landed, the central pressure was 950 hPa. A strong wind in the left-rear quadrant near the inner-core characterized MA-ON. In the Kanto Plain, about 20 ms^{-1} northerly sustained winds (10-min average) were observed at the north and the west side of the typhoon (Figure 2). Moreover, maximum instantaneous wind of 39.9 ms^{-1} was observed at Yokohama local meteorological observatory after the center of the typhoon passed by (Figure 3), and 1-minute averaged wind of 38.4 ms^{-1} was recorded at the coast of Hiratuka City. Another noteworthy characteristics of MA-ON are as follows. Kanto plain was broadly occupied by cold air at the low-level which was sustained during the passage of MA-ON. The wind directions in the cold air mass under the translating cyclone were quite different from the general feature of tropical cyclones swirling around the typhoon center with some inflow angle.

3. Numerical model and description

Numerical reproduction of the strong wind events in the southern Kanto plain was attempted using a two-way double-nested model (Mashiko and Muroi 2003). This model is based on Meteorological Research Institute/Numerical Prediction Division unified nonhydrostatic model of JMA (MRI/NPD-NHM; Saito et al. 2001). The model domain of the outer mesh with a 6 km horizontal grid size is 3000 km x 2400 km. The inner domain with a 2 km horizontal grid size is designed to explicitly resolve the inner core of the Typhoon and strong wind structure. The vertical grid of both models contains 50 levels with variable grid intervals of 40 m (near the surface) to 904 m (at the top of the domain), and the model top is located at 22.7 km. The initial and boundary conditions were produced from the MANAL and forecasts of the JMA Regional Spectral Model, respectively. In both domains, microphysics with the ice phase is used as precipitation processes, and no convective parameterization scheme is used. The initial time of the outer domain was 21 JST 08 October 2004. The inner domain was initialized at 6-hour forecast by interpolating output from the outer domain, and it was integrated for 18 hours. The sensitivity tests were also conducted by using the single domain run (6 km horizontal resolution) and the triple nested run (0.667 km horizontal resolution in the innermost mesh).

4. Results

Strong winds observed in a narrow area in the left-rear quadrant of MA-ON during its passage over the southern portion of the Kanto Plain were simulated fairly well. Figure 4 shows the simulation result of the equivalent potential temperature at a height of 250 m from the inner domain. The typhoon with high equivalent temperature moved over the cold air mass at the low-level in the Kanto plain. The flow of the cold air mass at the low-level formed just like ‘gap flow’ between the typhoon center and the mountains in the west of the Kanto plain. A strong wind area greater than 60 ms^{-1} is seen over Sagami Bay, where is corresponding to the gap outflow region. The cold air mass flow decreased in depth in the left-rear quadrant of Typhoon. Trajectory analysis from the model output shows that the parcels associated with the strong winds descended with diffluent flows and accelerated. Figure 5a and 5b show the vertical

cross-sections of equivalent potential temperature and horizontal wind, respectively. They show that the strong wind area can be seen only at the low level on the western side of the storm and it corresponds to the cold air mass quite well. This feature of the strong winds was not observed before the landfall. The experiment eliminating the mountains on the western side of the Kanto plain shows that the strong winds of the left-rear quadrant decreased by about 25 ms^{-1} (not shown).

Figure 6 shows the result of the single run with a horizontal grid length 6 km. The strong winds in the left-rear quadrant of the storm were not well reproduced. This experiment was conducted with the same topography as the double nested run, therefore it indicates that the inner core of the typhoon need to be resolved enough in this event. The triple nested run could resolve the detailed structure well, such as the disturbances on the shear line of the cold air mass flow, but the feature of the strong winds in the left-rear quadrant were not so different from those of the double nested run (not shown).

REFERENCES

Mashiko, W. and C. Muroi, 2003: Development of a two-way multiply-nested movable mesh typhoon model using the cloud resolving nonhydrostatic model. CAS/JSC WGNE No.33, 5.22-5.23.

Saito, K., T. Kato, H. Eito and C. Muroi, 2001: Documentation of the Meteorological Research Institute / Numerical Predic-tion Division Unified Nonhydrostatic Model. Technical Re-ports of the MRI, 42, 133pp

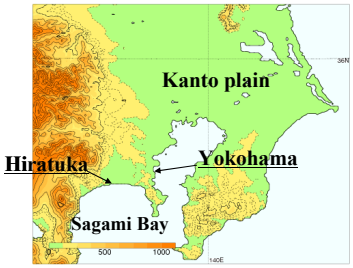

Fig. 1. Geographical map around Kanto plain.

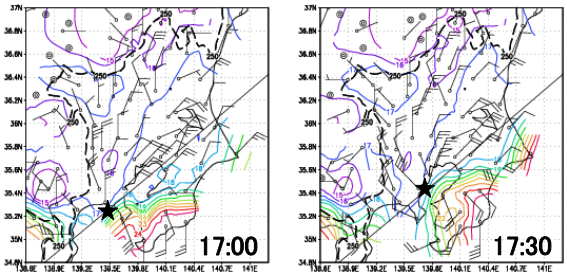

Fig. 2. Distribution of surface winds and temperature from AMeDAS stations (a) at 1700 JST and (b) at 1730 JST 9 Oct. Wind barb and flag represent 5ms^{-1} and 25ms^{-1}, respectively. Solid line shows the track of MA-ON with the estimated center of the storm.

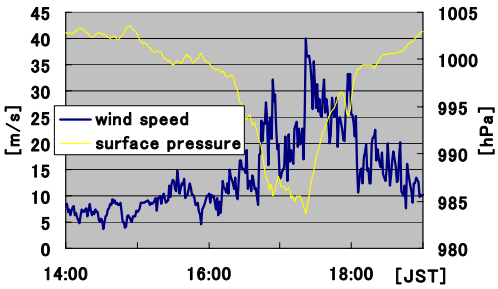

Fig. 3. Time sequence of instantaneous wind speed, sea surface pressure at Yokohama local meteorological observatory between 1400 and 1900 JST.

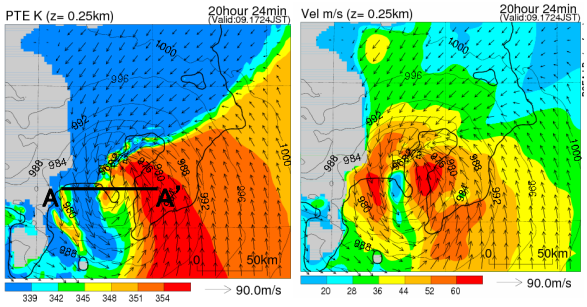

Fig.4. Horizontal distribution of (a) equivalent potential temperature and (b) wind speed at a height of 250 m. Vectors denote the horizontal winds. The area above 250 m height is masked with the gray color.

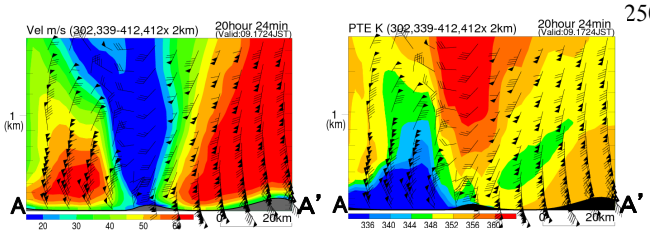

Fig.5. The east-west vertical cross sections of (a) the equivalent potential temperature and (b) the wind speed along the line A-A' in Fig.4a. Full wind barb and flag indicate the horizontal wind speed of 5 ms^{-1} and 25 ms^{-1}, respectively.

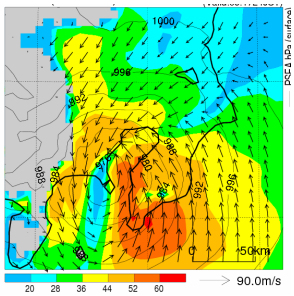

Fig.6. Same as Fig 3a, but the single run with a 6 km horizontal grid length.

A Cloud-resolving Numerical Simulation for Orographic Rainfall Associated with Typhoon Meari (2004)

Akihiko MURATA

Meteorological Research Institute / Japan Meteorological Agency, Tsukuba, Ibaraki 305-0052, Japan

1. Introduction

Heavy rainfall in a mountainous area in Japan caused by typhoon Meari (2004) was investigated using a cloud-resolving model. The targeted area was the east coast of the mountainous Kii peninsula, located at 34N, 136E (see Fig. 1). The typhoon initially tracked northwestward as it gradually intensified and reached its lowest minimum sea-level pressure. The typhoon recurved to the northeast in the East China Sea and made landfall in Kyushu, Japan, at 0830 Japan Standard Time (JST) on 29 September. The storm moved almost parallel to the mountainous spine of Honshu, the mainland of Japan.

Before the typhoon landfall, heavy rainfall in the eastern part of the Kii Peninsula started. From the 12-hour accumulated rainfall amount, ranging between 6 h before and 6 h after the landfall, it is found that the amounts are considerable in the eastern part of the Kii Peninsula (Fig. 1). In particular, the precipitation is more than 400 mm around Owase, located at the middle part of the east coast of the peninsula.

A marked characteristic of this heavy rainfall is that the area of precipitation is far from the storm center: more than 500 km. The goal of this study is to clarify the mechanism of the characteristic rainfall.

2. Numerical model and experimental design

The numerical model we used is the Japan Meteorological Agency Nonhydrostatic Model (JMANHM; Saito et al., 2006) with the horizontal grid spacing of 5 km and 1 km (referred to 5 km-NHM and 1 km-NHM, respectively). We adopt a grid-nesting strategy for the lateral boundary conditions: double nested JMANHM. The nesting procedure is as follows: The initial (2200 JST 28 September 2004) and lateral boundary data for 1 km-NHM (501×501×50 grid points) are obtained from forecasts produced by 5 km-NHM (719×575×50 grid points). The initial (2100 JST 28 September 2004) and lateral boundary data for 5 km-NHM are obtained from the JMA mesoscale analysis data produced with a four-dimensional variational assimilation technique. Kain-Fritsch convection scheme is included in 5 km-NHM in addition to a bulk cloud microphysical scheme.

3. Partitioning heavy rainfall into three precipitation systems

From radar observations, it was found that the precipitation systems were categorized as follows: A) the stationary system observed around Owase, B) the moving system to the southwest of the system A, and C) the band-like moving system to the southeast of the system B. The categorized precipitation

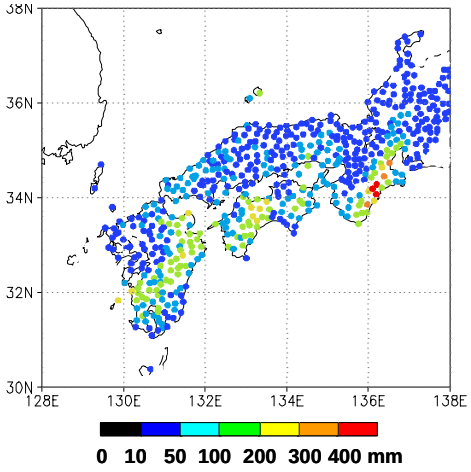

Fig. 1 Horizontal distribution of 12-hour accumulated (from 0300 JST to 1500 JST on 29 September 2004) rainfall amount measured by the JMA rain-gauge network.

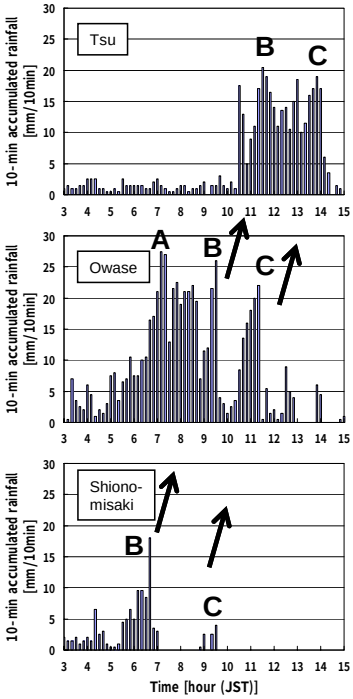

Fig. 2 Time series of 10-minute accumulated rainfall amount observed at three stations located along the east coast of the Kii Peninsula. The location of each observation point is shown in Fig. 3. The peaks corresponding to the precipitation systems A, B, and C are also shown.

systems were also observed in the time evolution of 10-min accumulated rainfall amount measured with rain gauges located along the coast. In the time series of each observation point, a couple of peaks are found (Fig. 2). The peaks move along the coast from southwest to northeast. The movement seems to be forced by flow in middle troposphere.

The simulation of typhoon Meari using 1 km-NHM is successfully reproduced the heavy rainfall (Fig. 3). The simulated precipitation patterns are favorably compared with the analyzed precipitation, based on radar reflectivity and rainfall amounts measured by rain gauges. The simulation well represents the three precipitation systems mentioned above. Detailed examination of the model fields reveals that the predominant processes for the formation and maintenance of each precipitation system is as follows: system A) Vertical instability in the low-level humid easterly on the slope of mountains located along the east coast of the Kii Peninsula, system B) Horizontal wind shear along the boundary between low-level easterly and south-easterly flow, and system C) Cold pool along the edge of the system and low-level inflow into the system like a tropical cyclone spiral rainband.

4. Sensitivity of topography and moisture

To investigate the effect of topography on each precipitation system, we conduct a sensitivity experiment in which model topography over the Kii Peninsula is removed. The simulated precipitation is shown in Fig. 4. The most significant difference in the horizontal pattern is that the precipitation system A shown in Fig. 3 disappears in Fig. 4, suggesting that the system A is associated with interaction with the topography. The precipitation systems B and C, on the other hand, are simulated even in the experiment in which the mountain effect is removed. The precipitation patterns of the systems are similar to those produced in the control simulation with topography. The results indicate that the effect of topography on the system B and C is much less than that on the system A.

Sensitivity of the initial field is also investigated using 5-km NHM. Five initial data are used: 2100 JST on 27 September, 0300, 0900, 1500, and 2100 JST on 28 September. The heavy rainfall over the east coast of the Kii Peninsula is well simulated in two experiments, whereas rainfall amount is not so large in other three experiments. Between the two groups of the simulation, there is a crucial difference in moisture. The simulations where the heavy rainfall is well reproduced have relatively large amount of precipitable water compared with that obtained from the other group simulations. The results suggest that moisture play a critical role in the occurrence of the heavy rainfall in both real and model atmosphere.

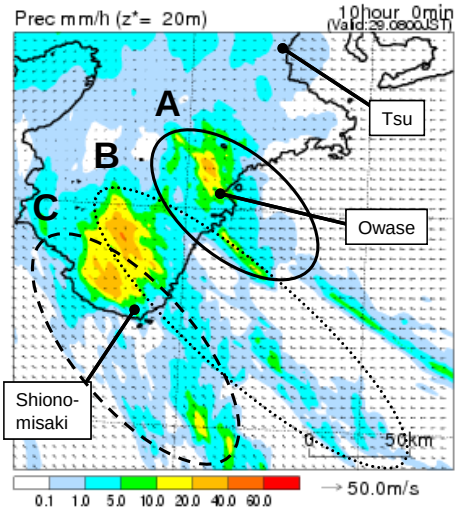

Fig. 3 Horizontal distribution of 1-hour accumulated rainfall amount at 0800 JST on 29 September simulated by JMANHM. The indexes of A, B, and C denote the precipitation systems. The location of each station in Fig. 2 is also shown.

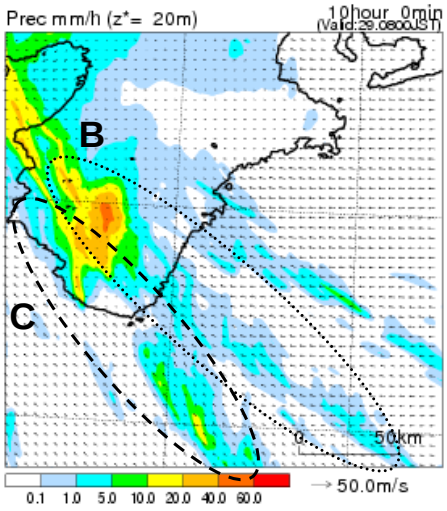

Fig. 4 Same as in Fig.3, but simulated by JMANHM without topography over the Kii Peninsula.

Reference

Saito, K., T. Fujita, Y. Yamada, J. Ishida, Y. Kumagai, K. Aranami, S. Ohmori, R. Nagasawa, S. Kumagai, C. Muroi, T. Kato, H. Eito and Y. Yamazaki, 2006: The operational JMA Nonhydrostatic Mesoscale Model. Mon. Wea. Rev. (in press)

Evaluation and validation of the hydrological cycle simulated by the Canadian Regional Climate Model (CRCM) using an integrative approach

Biljana Music[1] and Daniel Caya[2,1]

[1]Canadian Network for Regional Climate Modeling, UQÀM, Montréal, Québec, Canada.
[2]Ouranos Consortium, Montréal, Québec, Canada.

Evaluation and validation of the hydrological cycle simulated by the Canadian Regional Climate Model (CRCM) (Caya and Laprise, 1999) are important aspects of model development. Usually, at the regional scale, only precipitation and river streamflow observations are available. We, therefore, need to develop a methodology for validation of water cycle components that makes use of available observations.

In this contribution, an integrative analysis approach is presented. This approach links both the terrestrial and atmospheric branches and involves a long-term time means of the hydrological cycle components, spatially averaged over a given river basin.

The water budget equations for the atmospheric and terrestrial branches can be expressed as:

$$\frac{\partial W}{\partial t} = C - (P - E) \qquad (1)$$

$$\frac{\partial (M + S)}{\partial t} = (P - E) - R \qquad (2)$$

where W (kg m^{-2}) is the column storage of the atmospheric water, C is the vertically integrated horizontal moisture flux convergence, E (kg m^{-2} s^{-1}) is evapotranspiration, and P (kg m^{-2} s^{-1}) is precipitation. The quantity $M + S$ (kg m^{-2}) represents the storage of soil moisture (M) and the accumulated snowpack (S), and R (kg m^{-2} s^{-1}) is the total runoff.

The following approach can be used to perform the analysis of the annual means of the water cycle components. Taking time and spatial averages of the atmospheric and terrestrial water budget equations (1) and (2) over a multiyear period and over a given river basin leads to the following equations:

$$\left[\overline{C}\right] = \left[\overline{P}\right] - \left[\overline{E}\right] \qquad (3)$$

$$\left[\overline{R}\right] = \left[\overline{P}\right] - \left[\overline{E}\right] \qquad (4)$$

where $\overline{X}$ presents the time average of component X, and $\left[X\right]$ is the spatial average. Annual mean tendencies of atmospheric and terrestrial water storage can safely be neglected because they tend toward zero when averaged over long period of time.

In order to validate the various components of equations (3) and (4) simulated by the model, the corresponding observed values have to be known. An estimation of annual mean precipitation for a given basin ($\left[\overline{P}\right]_{OBS}$) can be obtained from the existing gridded precipitation analysis data sets. These datasets are not free from errors (for various reasons), but presently they constitute the best estimate of the real precipitation at the regional scale. The river streamflows observed at gauging stations are available for many river basins, so fairly good accuracy can be obtained for the value of annual mean runoff for a given basin $\left[\overline{R}\right]_{OBS}$. Evapotranspiration observations are seldom available at the regional scale and evapotranspiration must be estimated as a residual using the water budget analysis. We used the time- and space- averaged terrestrial water budget equation (4) to obtain the quasi-observed evapotranspiration:

$$\left[\overline{E}\right]_{QOBS} = \left[\overline{P}\right]_{OBS} - \left[\overline{R}\right]_{OBS} \qquad (5).$$

The model-simulated atmospheric water vapor convergence over the basin can be compared with the convergence computed from reanalysis data ($\left[\overline{C}\right]_{REAN}$). It must be emphasized that the characteristics of reanalysis data, such as spatial and temporal sampling, vertical resolution, and treatment of the lower boundary layer in the computation, limit the accuracy of estimated water vapor convergence.

The validation of the annual cycle of water budget components is more complex and involves larger uncertainties. While terrestrial and atmospheric water storage components can be neglected for multi-year means, they cannot for monthly means; these terms can be particularly large during spring and fall. For the

annual cycle analysis, the averaged water budget equations become:

$$\left[\frac{\partial \overline{W}_i}{\partial t}\right] = \left[\overline{C}_i\right] + \left[\overline{E}_i\right] - \left[\overline{P}_i\right] \quad (6)$$

$$\left[\frac{\partial (\overline{M} + \overline{S})_i}{\partial t}\right] = \left[\overline{P}_i\right] - \left[\overline{E}_i\right] - \left[\overline{R}_i\right] \quad (7)$$

where $\overline{X}_i = \frac{1}{J}\sum_{j=1}^{J} X_{i,j}$ is the climatological monthly mean, based on J years, with $X_{i,j}$ the monthly mean for month "i" and year "j". Quasi-observed evapotranspiration is now obtained as a residual of the atmospheric water balance as:

$$\left[\overline{E}_i\right]_{QOBS} = \left[\frac{\partial \overline{W}_i}{\partial t}\right]_{REAN} - \left[\overline{C}_i\right]_{REAN} + \left[\overline{P}_i\right]_{OBS} \quad (8).$$

The terms $\left[\overline{P}_i\right]_{OBS}$, $\left[\overline{R}_i\right]_{OBS}$, $\left[\frac{\partial \overline{W}_i}{\partial t}\right]_{REAN}$ and $\left[\overline{C}_i\right]_{REAN}$ can be obtained from one of the existing datasets based on in situ observations (first two terms) and from reanalysis (last two terms). Finally, monthly values of quasi-observed terrestrial water storage tendencies can be computed as residuals from averaged combined water budget equation:

$$\left[\frac{\partial (\overline{M} + \overline{S})_i}{\partial t}\right]_{QOBS} = \left[\overline{C}_i\right]_{REAN} - \left[\frac{\partial \overline{W}_i}{\partial t}\right]_{REAN} - \left[\overline{R}_i\right]_{OBS} \quad (9).$$

The hydrological cycle simulated by the CRCM (V. 3.6.3) over the Mississippi River basin for the period 1988-99 is evaluated using the above-presented approach. Gridded precipitation dataset from the Climate Research Unit (CRU TS2.02, Mitchell and Jones, 2005) and "undepleted" (water management effects removed) basin mean runoff (Maurer and Lettenmaier, 2001) are used as observations. The vertically integrated horizontal moisture flux convergence and atmospheric water storage tendencies are obtained from NCEP/NCAR reanalysis data.

Results of the analysis (see Fig. 1 and Figs. 2) suggest that this model version suffers from inadequate representation of land surface processes. The single-layer surface scheme used in the CRCM (V. 3.6.3) cannot accurately represent many of the effects of vegetative control of evapotranspiration as well as runoff generation. The prescribed water holding capacity, made to account crudely for the effects of a vegetative canopy, appears to be excessively high and results in too low runoff as well as too large evapotranspiration. The evapotranspiration overestimation then generates excessive precipitation. The bias in the atmospheric moisture flux convergence could be related to the biases of the CRCM evapotranspiration and precipitation, but the model dynamics should be also investigated for an evaluation of the moisture transport over the basin.

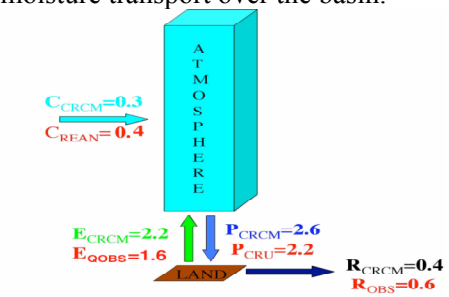

Fig. 1. Annual means (1988-1999) of the atmospheric and terrestrial water budget components, in mm/day, over the Mississippi River basin.

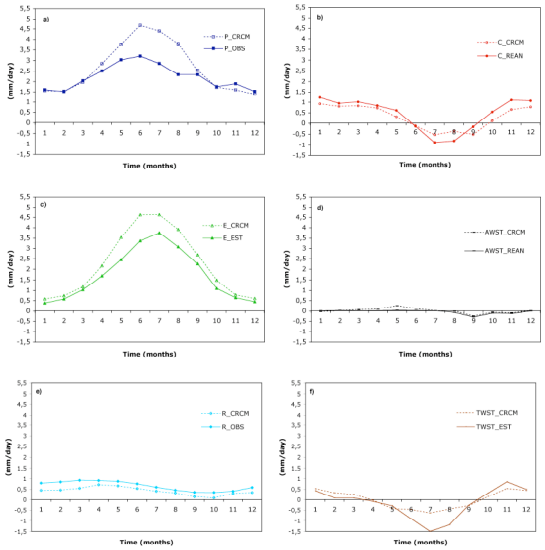

Figs. 2. Annual cycles of the atmospheric and terrestrial water budget components averaged over Mississippi River basin for the period 1988-1999: (a) precipitation, *P*; (b) vertically integrated horizontal moisture flux convergence, *C*; (c) evapotranspiration, *E*. (d) atmospheric water storage tendency, *AWST*; (e) runoff; (f) terrestrial water storage tendency, TWST.

References

Caya, D., and R. Laprise, 1999: A semi-implicit semi-Lagrangian regional climate model: The Canadian RCM. *Mon. Wea. Rev.*, **127**, 341-362.

Maurer, E.P. and D.P. Lettenmaier, 2001: Calculation of Undepleted Runoff for the GCIP Region, 1988-2000 (http://www.ce.washington.edu/pub/HYDRO/edm/WEBS_runoff/)

Mitchell, T.D., P.D. Jones, 2005: An improved method of constructing a database of monthly climate observations and associated high-resolution grids. Int. J. Climatol., 25(6), 693-712.

Sensitivity of cloud microphysical processes on hurricane intensity

S.Pattnaik and T.N.Krishnamurti
Department of Meteorology, Florida State University, Tallahassee, Fl, 32306
Email: spt@met.fsu.edu, tnk@io.met.fsu.edu

In this study we have conducted seven cloud microphysics sensitivity experiments and a control run (CTRL) to elucidate the impact of different microphysical processes (e.g. melting, evaporation) and parameters (e.g. fall speed, intercept parameter) of hydrometeors (e.g. cloud ice, snow, graupel) on the intensity of the hurricane Charley, 2004. We have used a high resolution (3km) triply nested (27/9/3) state of art mesoscale model (MM5) with NASA Goddard Space Flight Center (GSFC) microphysical parameterization Scheme (Tao and Simpson 1993) for carrying out these experiments. The seven different microphysical sensitivity experiments are as follows: NMLT3: where melting of ice, graupel and snow were suppressed, NMLT2: melting of ice and graupel were not allowed, QR_NEVP: evaporation of falling rain were eliminated, G_FALL: fall speed of graupel hydrometeor doubled, NOG: intercept parameter for graupel hydrometeors doubled, S_FALL: fall speed of snow hydrometeors were doubled and NOS: where intercept parameter of snow were doubled.

We noticed profound impact of the different cloud microphysical processes (i.e. melting, evaporation, fall speed and intercept parameter) on the intensity of hurricane Charley. The sensitivity experiments where physical processes such as melting of graupel and snow (i.e. NMLT2), melting of graupel, snow and cloud ice (i.e. NMLT3) and evaporation of rainwater (i.e. QR_NEVP) were eliminated from the model explicit parameterization scheme produced the most intense storms (Fig 1a). The reason of this intensification in NMLT2 and NMLT3 experiments can be attributed mainly due to the absence of melting processes in sub cloud layer which results in enhanced production and rapid fallout of graupel hydrometeors and a positive feedback to the latent heat release. The intensification of the storm generated from the sensitivity experiment where we have eliminated the rainwater evaporation from the model (i.e. QR_NEVP) can be explained as, lack of evaporation results in the reduction of the cooling tendencies within the storm eye wall which inhibit the generation of penetrative downdraft in the inner core and hence preventing the flow of cooler and drier equivalent temperature (θe) from mid troposphere to boundary layer thus maintaining the warming within the inner core of the hurricane (Fig 1b). We also noted that the variations made in the formulations which determines the fall speed and intercept parameter of graupel and snow hydrometeors did affect the intensity of the hurricane but not as much as in comparison to the suppression of inter conversion processes such as melting and evaporation of (i.e. graupel, snow and rain water). All intense storms (i.e. NMLT2, NMLT3 and QR_NEVP) exhibited stronger upward motion (Fig 1c) in the vicinity of eye wall and these called for the large scale influx of sensible and latent heat from marine boundary layer to the storm inner core, which facilitated the intensification rate. In (Fig 1d) we showed that the magnitudes of inner core warming (vertical structure of zonal temperature deviation) for the most intense storms (i.e. NMLT2, NMLT3 and QR_NEVP) are larger than those generated from the other sensitivity experiments, which reconfirms the profound influence of different microphysical processes in modulating the inner core of the hurricane and so also its intensity.

References:

Tao, W.-K., and J. Simpson, 1993: Goddard Cumulus Ensemble Model. Part I: Model description. Terrestrial, Atmospheric, and Oceanic Sciences, 4, 35-72.

(a)

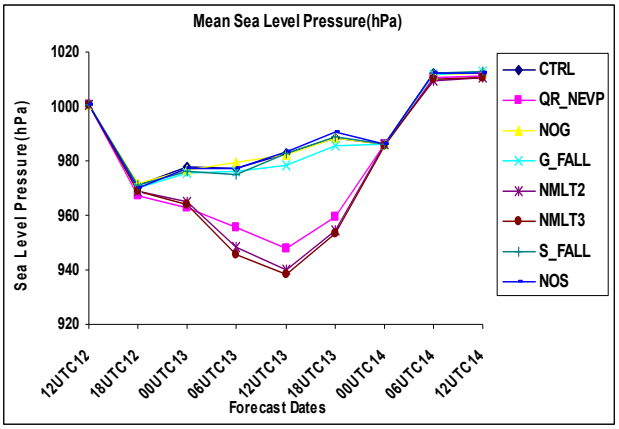

(b)

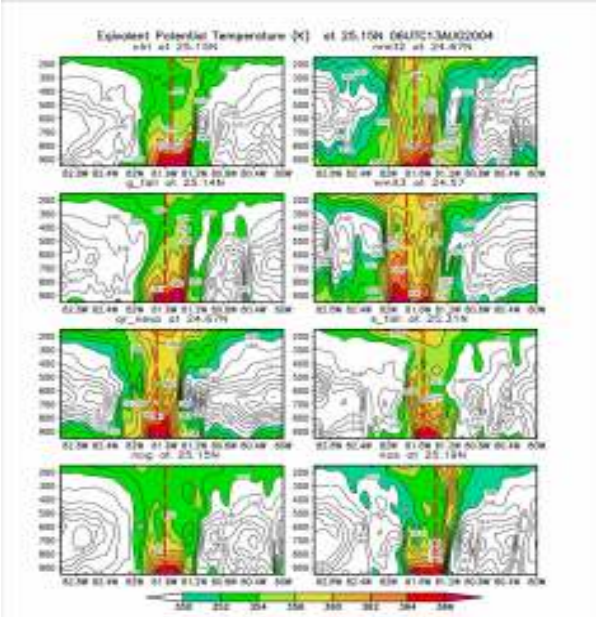

(c)

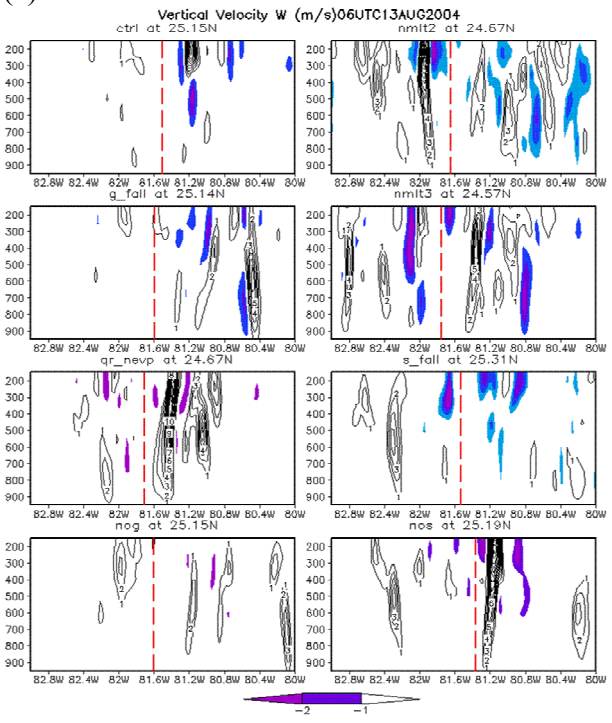

(d)

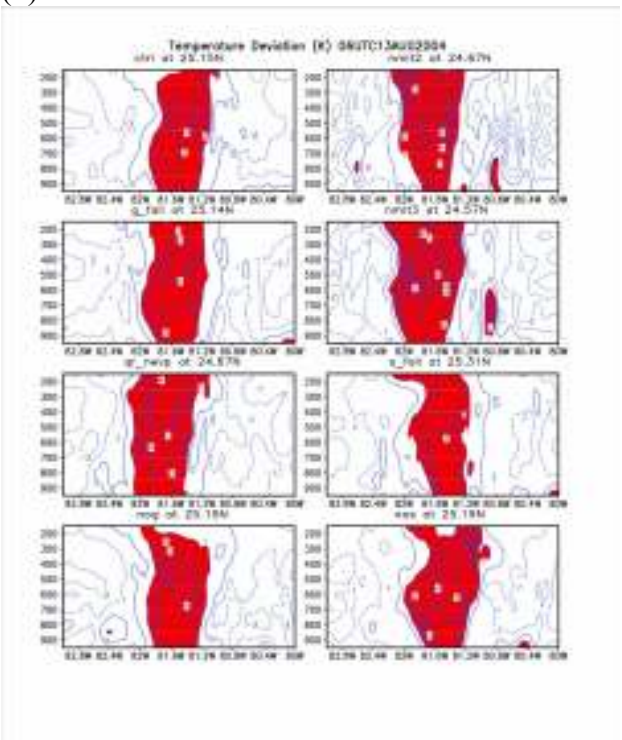

Figure 1 (a through d): (a) 48hour forecast of minimum sea level pressure (hPa) for microphysics sensitivity experiments; (b through d) Vertical structure snap shots for different microphysics sensitivity experiments at 0600 UTC 13 August 2004 (b) Equivalent potential temperature (K), (c)Vertical velocity (m/s) and (d) Deviation of temperature (K) with respect to zonal mean between 83.0W and 80W.

HYDRODYNAMIC - STATISTICAL MODEL OF OPERATIVE FORECAST TO 12-36H AHEAD OF STORM WINDS INCLUDING SQUALLS AND TORNADOES AT THE TERRITORY OF SIBERIA

E.V.Perekhodtseva

(Hydrometeorological Center of Russia, B.Predtechenskii 9-13, 123242, Moscow, Russia, e-mail: perekhod@mecom.ru)

The territory of Siberia is more great then territory of European part of Russia. Development of successful method of forecast of storm summer winds, including squalls and tornadoes, that often result in human and material losses, could allow one to take proper measures against destruction of buildings and to protect people. Well-in-advance successful forecast (from 12 hours to 36 hour) makes possible to reduce the losses. Prediction of the phenomena involved is a very difficult problem for synoptic of Siberia till nowdays. The existing graphic and calculation methods still depend on subjective decision of an operator.

At the present time in Russia there is no hydrodynamic model for forecast of the maximal speed of wind over then 25m|c, hence the main tools of objective forecast are statistical methods using the dependence of the phenomena involved on a number of atmospheric parameters (predictors). We have adapted for the territory of Siberia our statistical operative method of forecast of storm wind for Europe /1/.

. Statistical decisive rule of the alternative and probability forecast of these events was obtained in accordance with the concept of “perfect prognosis” using the data of objective analysis. For this purpose the teaching samples of present and absent of this storm wind at the territory of Siberia were automatically arranged that include the values of forty physically substantiated potential predictors.

Then the empirical statistical method was used that involved diagonalization of the mean correlation matrix of the predictors and extraction of diagonal blocks of strongly correlated predictors. Thus for this phenomenon the most informative predictors were selected without loosing information, those predictors being either a representative of each block or an independent informative predictors. The statistical decisive rules for diagnosis and prognosis of the phenomena involved were calculated for the most informative vector-predictor that includes the most informative (we used the criterion of distance of Mahalanobis and criterion of minimum of entropy by Vapnik-Chervonenkis) and slightly dependent predictors. Successful development of hydrodynamic models for short-term forecast and improvement of 36h forecasts of pressure, temperature and others parameters allow us to use the prognostic fields of those models for calculations of the discriminant functions and the values of probabilities of dangerous wind in the nodes thus to get fully automated forecasts.

For prognosis of the phenomenon of the wind with velocity over 25m|c involved with the given advance period 12,24,36 hours the values of the discriminant function and the probabilities of this phenomenon were calculated using the prognostic values of operative hemispherical model of Hydrometeorological Center of Russia in the nodes of the rectangular mesh 150x150 km over the territory of Siberia. In order to change to the alternative forecast the author proposes the empirical threshold values specific for this territory and for phenomenon of two classes (the first class - the wind with velocity V more then 18m/s and the second class – the wind with velocity V more than 24m/s) advance periods 12, 24,36 hours.

According the values of prognostic production (to12-36h ahead) of hemispheric model calculate we the values of prognostic discriminant functions and the prognostic probability values in the nodes of greed for shot-term forecast up to 36h. We carried out the verification

of this hydrodynamic-statistical method for the territory of Siberia. This method turned out successful enough.

The prediction even 36h advance of the summer storm wind (velocity more 24m/s) was so exact:

-V=25m/s in the south of Krasnoyarskiy areal on 18.06.05;

-V=27m/s in Novosibirsk on 24.06.05;

-V=37m/s in Altay on 24.06.05 too;

-V=25m/s in the North Siberia (Turukhansk) on 4.07.05;

-V=26v/s in the South of Teimyr peninsula on 20.07.05.

-V=28m/s in the Chita areal on 24.05.05;

One case of the storm wind V=26m/s in Chita wasn't warned. The value of estimate of the warning is 86%. The error of "false alarm" is not very high, and so the value of Pirsy-Obukhov criterion is T=0,78. We are going to apply this method to the forecast of storm wind at cold season as in European part of Russia /2/. This problem is very actually for Siberia.

For the recognizing of tornadoes at the territory of Siberia we suppose new method of forecast of tornadoes by expert system. Our expert system is developed for any territory and can be applied in other countries /3/.

The territory of Siberia has not very many meteorological stations and so hydrodynamic forecast of storm wind is not successful, but this new statistical method is successful, objective and automated.

The forecast of summer storm wind calculate every day two times per day for day and for night to 12, 24, 36 hours advance. This method is included into operative system of Hydrometeorological Centre of Russia.

Besides we developed the statistical method of forecast of the velocity values of storm wind in separate points by calculation prognostic regression equation. This method isn't operative at our Centre, but all of synoptic of Russia can to use it at your regional meteorological departments.

References

1. Operative automated forecast for short-term of 12-36 ahead of dangerous precipitation, squalls and tornadoes. European Conference on applications of meteorology (ECAM-03). 15-19 September, 2003, Rome. Proceedings.
2. Stochastic model of forecast of dangerous wind and precipitation of cold season at the territory of North Caucasus. .Russian symposium on stochastic methods. Sochi.1-7 October. Abstracts.
3. On develop of the expert system model of tornadoes at the European Part of Russia. Conference "Modern methods of function theory and problems of its application", Voronezh, 26.01.03.-01.02.03. Abstracts.

High-resolution simulation for the Alpine climate since 1958 – validation on monthly and daily timescales

K. Prömmel, M. Widmann, J. M. Jones and B. Geyer

GKSS Research Centre, Max-Planck-Str. 1, 21502 Geesthacht, GERMANY

E-Mail: kerstin.proemmel@gkss.de

A high-resolution regional simulation for Europe performed with REMO (REgional MOdel, Jacob and Podzun, 1997) for the period 1958 to 1998 has been analyzed with focus on the Greater Alpine Region (GAR) with its complex topography.

The dynamical core of REMO is based on the numerical weather prediction model EM (Europa Modell) of the German Weather Service and the parameterizations are taken from the ECHAM4 climate model of the Max-Planck-Institute for Meteorology. The simulation discussed here has a very high horizontal resolution of 1/6 deg on 20 vertical levels in the troposphere and lower stratosphere. It is driven by the 1.12 deg resolution ERA40 reanalysis through prescribing the values at the lateral boundaries and through forcing the large-scale wind field within the model domain by the spectral nudging technique (von Storch et al., 2000).

To validate the REMO simulation on different timescales, first, it is compared to the HISTALP monthly mean temperature station dataset for the GAR consisting of 131 long temperature series with a maximum length of nearly 250 years (Auer et al., 2005). Second, the simulation is compared to a daily mean temperature station dataset for Austria and Switzerland. To analyze whether the high resolution of the simulation leads to an added value in comparison to the ERA40 reanalysis, the reanalysis is also compared to both station datasets. The complex topography of the Alps can not be fully captured by REMO and ERA, which leads to large differences in altitude between the stations and the corresponding grid points. Therefore, a mean altitude correction of 0.65K/100m was applied to the model data.

The comparison is done by calculating correlation, bias and root mean squared error between the stations and the corresponding model grid points. The resulting values are averaged over six subregions defined by Böhm et al. (2001), namely West (Maritime), East (Continental), South (Adriatic), Po Plain, Central Alpine Low Level (CALL) and High Level (CAHL) (Fig. 2).

On the monthly timescale the correlations between the simulations and the HISTALP stations are generally high with lowest values in December and January of 0.63 to 0.91 and highest values in spring and autumn of 0.92 to 0.97. For West, East, South and Po Plain ERA has slightly higher monthly mean temperature correlations than REMO during nearly the whole year whereas for CAHL the opposite is true. For subregion CALL ERA and REMO have the same correlations.

The correlations between the simulations and the daily mean temperature dataset, which is limited to subregions West, East, CALL and CAHL (Fig. 4), are generally high with lowest values in winter and highest values in spring and summer. Except for East REMO has higher correlations than ERA during the whole year.

The monthly bias is positive (0 to 3 K) for both simulations and all subregions except CAHL during the whole year. REMO has for all subregions largest bias in late summer and smallest bias in winter and spring except for CAHL where temperature simulated by REMO is too warm in summer and too cold in winter. The ERA bias for West, East, South and Po Plain is in summer smaller and in winter larger than the REMO bias. For CAHL the opposite is true and for CALL the ERA bias is smaller only in autumn. The daily bias shows no differences to the bias on a monthly timescale.

As an indicator of the skill of REMO relative to ERA, the reduction of error has been calculated. Positive values indicate the magnitude of improvement of REMO in comparison to

ERA. On the monthly timescale REMO shows a slight improvement for all subregions except CAHL in winter and early spring (Fig. 1). In CALL this improvement ranges even from November to July. In CAHL REMO shows no improvement in winter due to the larger bias whereas the improvement from April to November is due to the smaller bias. REMO performs worst in East, South and Po Plain in summer.

The reduction of error on the daily timescale shows an improvement of REMO in comparison to ERA for subregions West, CALL and especially CAHL during nearly the whole year which is most pronounced in summer (Fig. 3). For subregion East REMO shows no improvement at all.

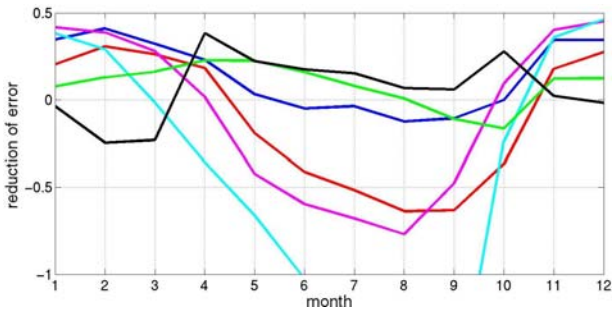

Fig 1: Reduction of error based on monthly mean temperature data averaged over six subregions.

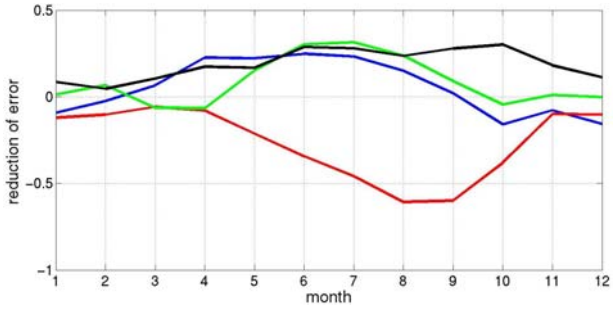

Fig 3: Reduction of error based on daily mean temperature data averaged over four subregions.

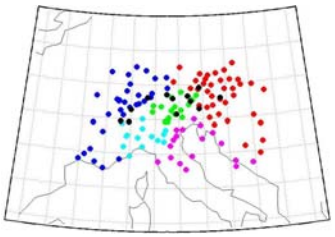

Fig 2: Monthly mean station dataset.

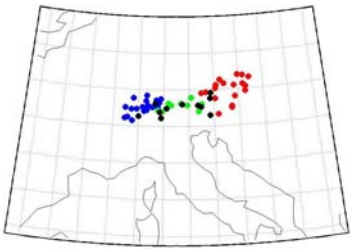

Fig 4: Daily mean station dataset.

To conclude, on the monthly timescale the higher resolution of REMO leads to an added value in comparison to ERA in winter and early spring and for the inner Alpine low and high level stations with more complex topography also in early summer. On the daily timescale REMO performs better than ERA during nearly the whole year for the inner Alpine regions and subregion West. The good performance of ERA can be explained by the fact that the observed temperature is an input variable for the reanalysis whereas REMO has to calculate the temperature.

References:

Auer, I. et al., 2005: HISTALP – Historical Instrumental Climatological Surface Time Series of the Greater Alpine Region 1760-2003, submitted to *International Journal of Climatology*.

Böhm, R. et al., 2001: Regional Temperature Variability in the European Alps: 1760-1998 from Homogenized Instrumental Time Series, *International Journal of Climatology*, **21**, 1779-1801.

Jacob, D. and R. Podzun, 1997: Sensitivity Studies with the Regional Climate Model REMO, *Meteorology and Atmospheric Physics*, **63**, 119-129.

von Storch, H. et al., 2000: A Spectral Nudging Technique for Dynamical Downscaling Purposes, *Monthly Weather Review*, **128**, 3664-3673.

Quantitative Precipitation Forecast Verification over Southeastern South America using CMORPH and CPC Data.

Juan Ruiz and Celeste Saulo
Centro de Investigaciones del Mar y la Atmósfera, Dpto de Cs. de la Atmósfera y los Océanos
Buenos Aires, Argentina.
jruiz@cima.fcen.uba.ar

1. Introduction:

The WRF (Weather Research and Forecasting) model has been implemented at CIMA (Centro de Investigaciones del Mar y la Atmósfera) since November 2005, to provide operative short range, mesoscale weather forecasts over South America (http://wrf.cima.fcen.uba.ar). One of the most important aspects related to the utility of a forecast is the skill of the Quantitative Precipitation Forecast (QPF). QPF verification over South America is particularly difficult because of the lack of raingauge observations and the in-homogeneity of their location (Saulo and Ferreira, 2003). As stated by these authors, precipitation gridded data sets obtained through any kind of interpolation over this region, are crude representations of actual rain, since they generally tend to smooth the field and enlarge the area with precipitation. For these reasons, we decided to use two different gridded data sets to assess the skill of WRF QPF using two alternative convective schemes.

2. Methodology:

Two different configurations of the WRF model have been tested for the period October 22nd - November 27th 2005: the first one uses Grell cumulus parameterization (Grell 1993) (WRF-G) and the second one uses the Kain Fritsch scheme (Kain and Fritsch, 1990) (WRF-KF), while all other settings were kept identical. The model was run in non-hydrostatic mode with an horizontal resolution of 50 Km and 31 vertical levels. Both configurations have been verified over the South American region using two different precipitation gridded data sets: the CPC Daily precipitation analysis, which is based on raingauge data and is available with a 1º horizontal resolution (http://www.cpc.ncep.noaa.gov/products/precip/realtime/) and the CMORPH precipitation estimates (Joyce et. al. 2004). This particular data set provides precipitation estimates based on passive microwave sensing at a maximum resolution of near 0.1 degree and a temporal resolution of 30 minutes. In this study 24 hourly accumulated precipitation at 1º degree spatial resolution has been used. QPF has been evaluated through the calculation of the Equitable Threat Score (ETS) and the Bias Score (BIAS) as in Saulo and Ferreira (2003). The QPF has been verified over two distinct areas, one encompassing the northern portion of South America (25º to 0º S and 80º to 50º W) and the other, the southern one (45º to 25º S and 80º to 50º W). This partition of model domain roughly accounts for the large differences found in precipitation regimes between tropical and midlatitude areas.

3. Results:

Figure 1 shows the ETS as a function of precipitation thresholds for both regions calculated using the CMORPH precipitation estimates. ETS are higher over the southern region than over the northen region, as expected. Over the northern region the model scores are nearer to persistence, indicating that the model forecast provides less useful information about QPF. This result is similar to that reported by Ebert et. al. (2003) in an intercomparison of global forecasts over northern Australia. Over the Southern region (Figure 1 b) WRF skill is far above persistence and scores are higher than over the tropical region. Differences between both parameterizations seem to be small but indicate a better performance of the WRF-G for higher thresholds and 24-hour forecast (Figure 1 b). For 48-hours forecast WRF-KF has better scores, what may be due to an underestimation of precipitation in the WRF-G (Figure 3 b).
Figure 2 shows the ETS scores computed using the CPC dataset. These scores are better than when comparing against CMORPH data for both configurations at higher thresholds and WRF-KF performs slightly better than WRF-G at 24 hours. The difference in the scores computed from different precipitation estimates may be due to the lack of a dense and homogeneous raingauge network. CMORPH data provides precipitation estimates with higher spatial and temporal resolution allowing the verification of QPF at higher resolutions and with a more homogeneous spatial coverage. The accumulated precipitation for the whole period (not shown) and a day by day subjective inspection of precipitation fields, reveals that accumulated precipitation is less in CPC than in CMORPH. WRF-G shows BIAS near 1 when compared to CMORPH data, but has large positive BIAS when compared against CPC data (not shown). Although differences between verifying dataset don't allow to conclude which configuration attains better scores, there are significant BIAS differences for the WRF-G between the 24 and 48 hours forecast which produces faster forecast degradation with increasing forecast length (Figure 3).

Acknowledgments: *This research is sponsored by the Research Grants UBACyT X155 and PIP (CONICET) 5417.*

References

Grell G. A., 1993: **Prognostic Evaluation of Assumptions Used by Cumulus Parameterizations.** *Monthly Weather Review*., 121, 764–787.
Ebert E. E., Ulrich Damrath, Werner Wergen and Michael E. Baldwin, 2003: **Supplement to The WGNE Assessment of Short-term Quantitative Precipitation Forecasts.** *Bulletin of the American Meteorological Society*., 84, 492–492.
Joyce J. R., J. E. Janowiak, Phillip A. Arkin and Pingping Xie, 2004: **CMORPH: A Method that Produces Global Precipitation Estimates from Passive Microwave and Infrared Data at High Spatial and Temporal Resolution**. *Journal of Hydrometeorology*., 5, 487–503.
Kain, J. S., and J. M. Fritsch, 1990: **A one-dimensional entraining/ detraining plume model and its application in convective parameterization**. *J. Atmos. Sci.*, **47**, 2784–2802.
Saulo A. C. and Lorena Ferreira, 2003: **Evaluation of quantitative precipitation forecasts over southern South America.** *Australian Meteorological Magazine*., 52, 81-93.

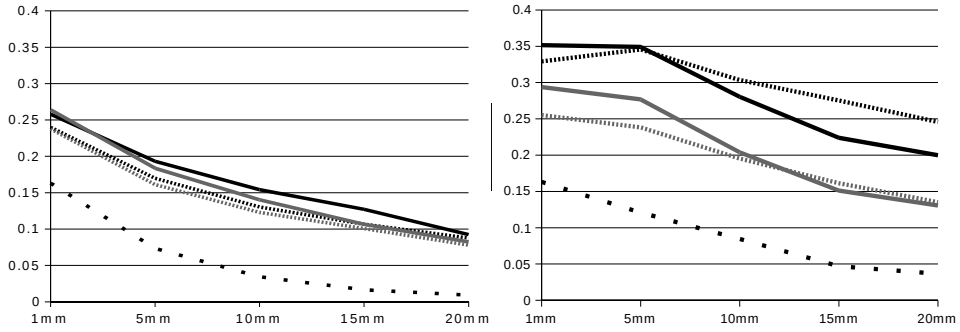

Figure 1: ETS (against CMORPH data) for 12-hour accumulated precipitation as a function of precipitation thresholds. (a) North and (b) South. WRF-Grell (fine dotted line), WRF-KF (continuous line) and persistence (dotted line). 24-hr forecast in black and 48-hr forecast in grey.

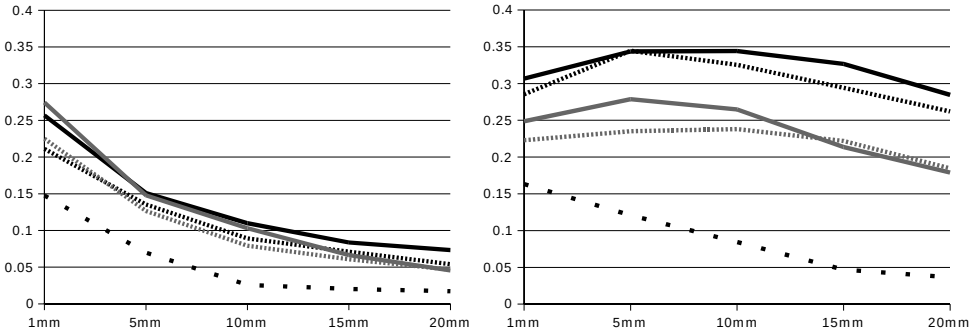

Figure 2: As in Figure 1, but compared against CPC raingauge interpolated data.

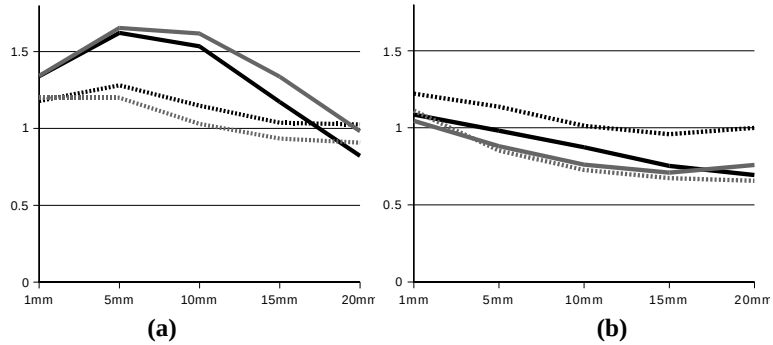

Figure 3: BIAS for 24-hour accumulated precipitation as a function of precipitation thresholds for the northern region. (a) Northern region and (b) Southern region. WRF-G (fine dotted line), WRF-KF (continuous line). 24-hour forecast (black), 48-hour forecast (grey). In both cases, BIAS are calculated with respect to CMORPH data.

Mesoscale ensemble prediction experiment of a heavy rain event with the JMA mesoscale model

Kazuo Saito* Masayuki Kyouda and Munehiko Yamaguchi****
** Meteorological Research Institute, Tsukuba, Ibaraki 305-0052, Japan; ksaito@mri-jma.go.jp*
*** Numerical Prediction Division, Japan Meteorological Agency*

Performance of mesoscale NWP has been improved by the recent progress of high resolution models and data assimilation methods. However, several difficulties have remained in prediction of severe mesoscale meteorological phenomena such as the heavy rainfall, especially when the environmental forcing is weak. One of the reasons is that mesoscale severe events are often very sensitive to the initial condition, and small errors in the analysis sometimes yield large differences in the prediction of rainfall. Idea of the ensemble prediction should be introduced into the mesoscale NWP to overcome such the problem. In recent years, several national forecast centers started their trials of mesoscale/regional ensemble predictions, but no general methods have been established yet for the prediction of heavy rains. In this study, we performed a preliminary ensemble prediction experiment for a heavy rainfall event in Japan with the JMA nonhydrostatic mesoscale model (JMANHM; Saito et al., 2006). Influences of the initial and lateral boundary conditions on the rainfall prediction are investigated.

A torrential rain occurred in northern Japan on 13 July 2004. The operational JMA hydrostatic mesoscale model (MSM) failed to predict observed concentration of the heavy rain. Predictions by JMANHM with a horizontal resolution of 10 km and operational JMA regional model (RSM) were also insufficient (Fig. 1). Kato and Aranami (2005) studied this case and showed that a high-resolution (1.5 km) version JMANHM can reproduce a band-shaped rainfall concentration, but the predicted precipitation intensity was weaker than the observation.

A downscale experiment is conducted using the JMA global ensemble prediction system (Global EPS) as the initial and boundary conditions of JMANHM. Same specification as in the operational version is employed (horizontal resolution 10 km, 361 x 289 grid points and 40 vertical levels). Figure 2c shows the averaged 6 hour accumulated rains over northern Japan (rectangle in Fig. 3a) predicted by JMANHM. These are similar to those by the Global EPS (Fig. 2a). Control runs (blue diamonds) underestimate the rain in both the initial stage (FT=00-06) and the period of the heavy rainfall (FT=12-18). Most members that the bred perturbations are added (red squares) further underestimate the rain in the initial stage (FT=00-06). On the other hand, members that the bred perturbations are subtracted (yellow triangles) tend to further underestimate the rain in the period of the heavy rainfall. These tendencies may be attributed by that the initial perturbations of the Global EPS are bred vectors by the BGM method, and they tend to reduce the moisture in the rainfall areas because the change of the moisture is limited by the saturation. The maximum rainfall values also have similar tendencies, but are quantitatively different. The global EPS (Fig. 2b) significantly underestimate the maximum rainfall amount compared with the observation (76 mm and 180 mm in the initial and heavy rainfall stages, respectively; not shown). On the other hand, JMANHM (Fig. 2d) predicts larger maximum rainfall, though most members still underestimate the rain. Affects of the lateral boundary condition (LBC) on the rainfall prediction are investigated by adding sensitivity experiments whose LBCs are changed (cross marks in Figs. 2c and 2d). The rainfall amounts were almost unchanged in both averaged and maximum values until FT=06, and the changes were small even in FT=12-18.

Figures 2e and 2f show the result of an ensemble prediction with JMANHM, where the initial conditions are given by the Meso 4D-Var analysis with perturbations by the Global EPS. In this experiment, the lateral boundary condition is given by RSM as in the operational NWP, while the Global EPS perturbations are added to the analysis after a normalization considering the errors of the Meso 4D-Var analysis. Significant quantitative improvement is seen in both the averaged and maximum values of predicted rainfall. Many perturbed members predict larger maximum rainfall than the control run. Figure 3 shows 3 hour accumulated rainfall by four members 'M03p', 'M04p', M06p' and 'M08p'. Intense band-shaped rainfall areas similar to observation (Fig. 1a) are predicted.

References

Kato, T. and K. Aranami, 2005: Prediction of localized heavy rainfall using a cloud-resolving nonhydrostatic model and its problem. *CAS/JSC WGNE Research Activities in Atmospheric and Oceanic Modelling*, **35**, 5.11-5.12.

Saito, K., T. Fujita, Y. Yamada, J. Ishida, Y. Kumagai, K. Aranami, S. Ohmori, R. Nagasawa, S. Tanaka, C. Muroi, T. Kato and H. Eito, 2006: The operational JMA nonhydrostatic mesoscale model. *Mon. Wea. Rev.* (in press)

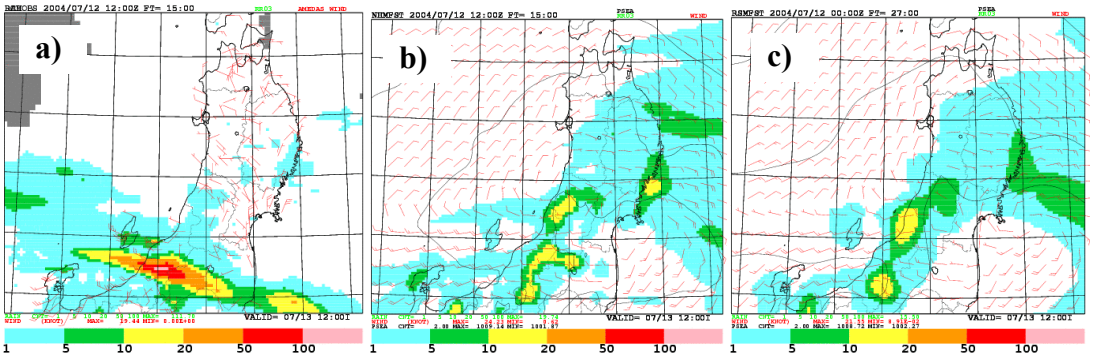

Fig. 1. a) Observed rainfall from 00 to 03 UTC 13 July 2004. **b)** Corresponding 3 hour rainfall from FT=12 to FT=15 by JMA mesoscale model. Initial time is 12 UTC 12 July 2004. **c)** Same as in b) but prediction by JMA regional model whose initial time is 00 UTC 12 July 2004.

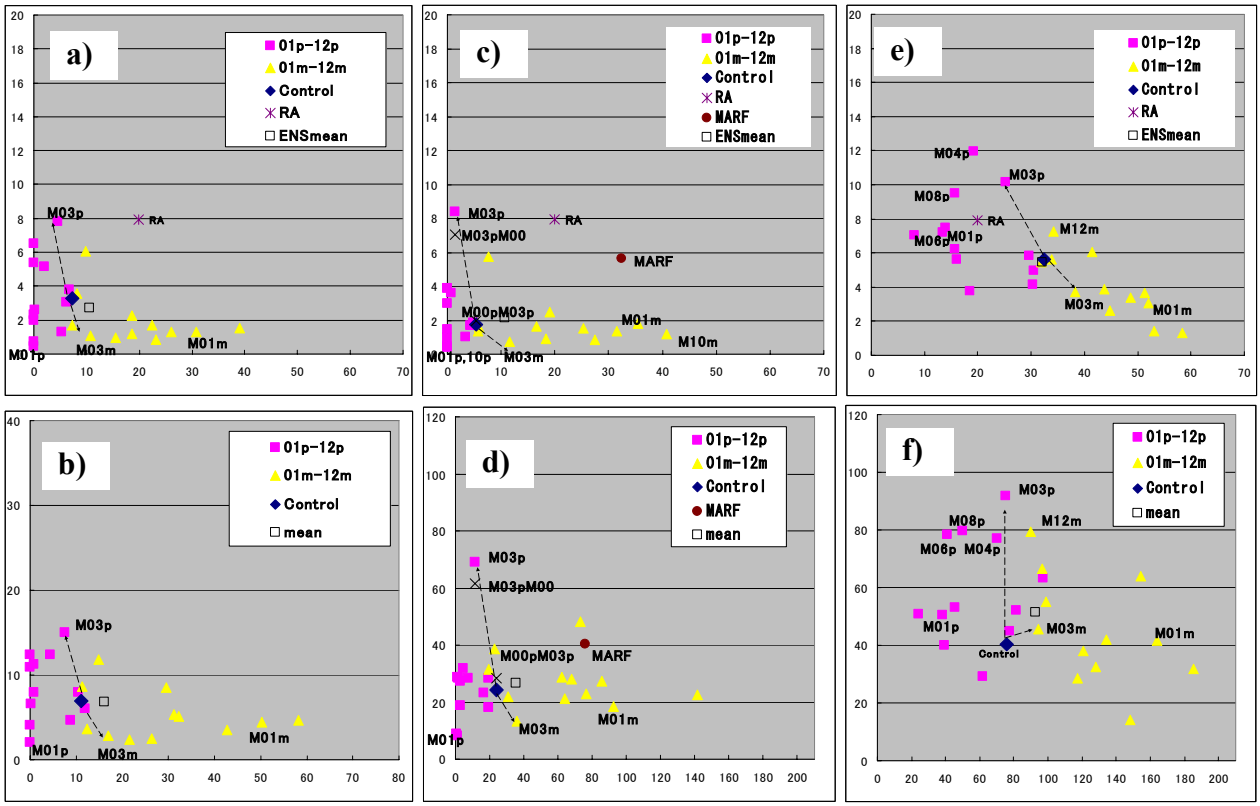

Fig. 2. a) Averaged 6 hour accumulated rain over northern Japan (rectangle in Fig. 3a) by Global EPS. Horizontal axis is for FT=00-06, while vertical axis is for FT=12-18. **b)** Same as in a), but for maximum rainfall amount. **c), d)** Same as in a), b) but 10 km JMANHM. Initial and lateral boundary conditions are given by Global EPS. Scale of hte horizontal axis is changed. **e), f)** Same as in c) d) but initial conditions are given by Meso 4D-Var with normalized perturbations by the Global EPS, and lateral boundary condition is by RSM.

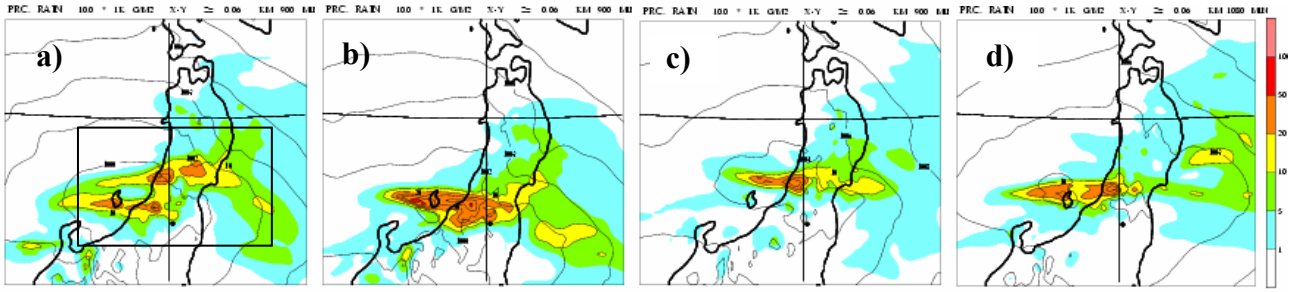

Fig. 3. Simulated 3 hour rainfall from FT=12 to FT=15 by JMANHM. Initial time is 12 UTC 12 July 2004. Initial conditions are given by Meso 4D-Var with perturbations by Global EPS, and lateral boundary condition is RSM. **a)** Member 'M03p' **b)** Member 'M04p' **c)** Member 'M06p' **d)** Member 'M08p' for FT=15 to FT=18.

The new Lokal-Modell LME of the German Weather Service

Jan-Peter Schulz

Deutscher Wetterdienst, Offenbach am Main, Germany
E-mail: jan-peter.schulz@dwd.de

1 Introduction

In order to fulfill new requirements of both external and internal customers, for instance in aviation, sea traffic or air pollution modelling, the German Weather Service (DWD) decided to expand the model domain of the operational limited area model, the Lokal-Modell (LM, Doms and Schättler 2002). The new version has successfully been introduced in the operational numerical weather prediction system of DWD on 28 September 2005.

2 The model LME

The former version covered basically Central Europe, including Germany and its neighbouring countries. The new version covers almost entire Europe and therefore got the name LM Europe (LME). The integration domain of LME is shown in Fig. 1.

The number of grid points per layer is enhanced from 325 $\times$ 325 to 665 $\times$ 657, while the mesh size is kept unchanged at 7 km $\times$ 7 km. The number of vertical layers is increased from 35 to 40. The additional layers are mainly located in the lower troposphere, the height of the lowest layer is reduced from 33 m to 10 m. This is in accordance with the new 40-km version of the driving global model GME which started operation at DWD in September 2004. The poles of the rotated LME coordinate system are different from the LM system. The LME system is rotated in a way that the equator is located within the center of the model domain. This has the advantage that the grid cells have a similar size and shape throughout the entire domain or, in other words, the divergence of the longitude rows is minimal. The main non-technical model change is the introduction of a new multi-layer soil model, the same that was incorporated into GME in 2004.

3 Results

The introduction of LME at DWD was done in several steps. First of all, two experiments were set up in 2004, namely LME and LM, running daily forecasts initialized and driven by GME. Here, the influence of the domain size or the distance between the boundaries and the region of interest, respectively, can be tested. It turns out that in most weather situations there is very little influence. But, there are sporadic cases where for example the development of a cyclone evolves significantly differently. The results of an objective verification show some advantage for LME forecasts for precipitation and gusts and some disadvantage for mean sea level pressure.

In January 2005 a full LME data assimilation cycle was set up in an operational parallel suite at DWD. This parallel suite also includes two 78h-forecasts (00 and 12 UTC) per day. Hence, LME could be tested in operational mode against LM and GME during spring and summer 2005. All postprocessing procedures had to be adjusted. A verification showed similar results as the earlier experiments in 2004.

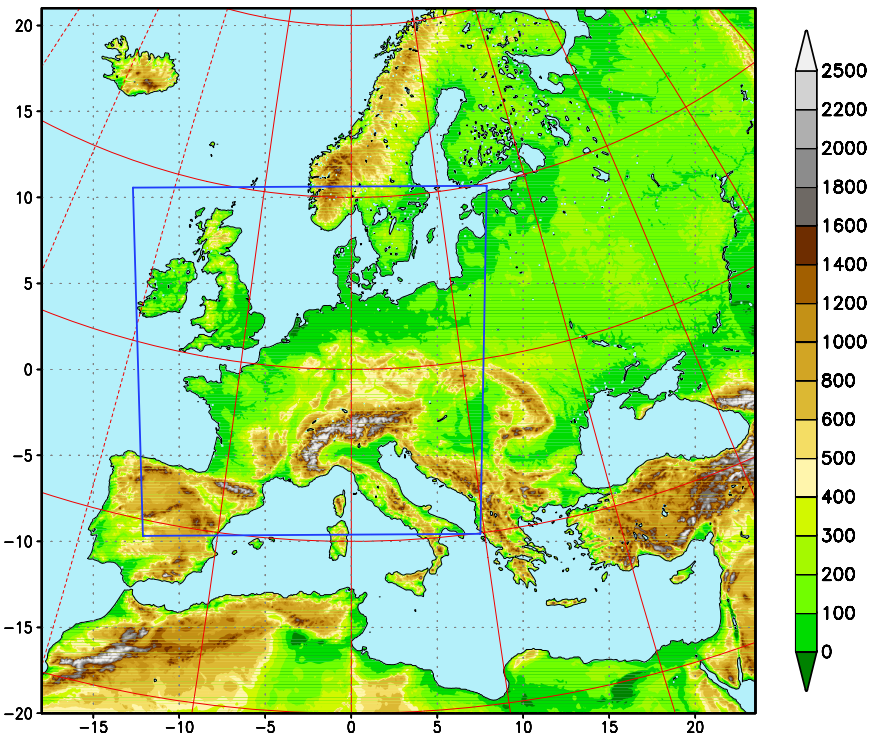

Figure 1: Model domain of LME. Topographical height (m) for land fractions > 50% (for the operationally used filtered orography). The frame in the figure depicts the integration domain of the former LM.

More detailed comparison revealed that the evaporation over sea in LME is up to 30% higher than in GME. Furthermore, precipitation in LME tends to show a systematic positive trend during the forecasts, even on a monthly mean basis, while precipitation in observations and also in GME is balanced. This behaviour indicates that evaporation over sea in LME is likely to be overestimated. Some sensitivity tests were carried out at DWD and a parameter tuning led to a LME version with reduced evaporation over sea. A verification of this version showed an improvement in the simulated moisture budget and also the mean sea level pressure.

4 Conclusions

In order to fulfill the requirements of several customers the German Weather Service (DWD) decided to expand the model domain of its operational limited area model, the Lokal-Modell (LM). The new LME, covering almost entire Europe, has successfully been introduced in the operational numerical weather prediction system of DWD on 28 September 2005. Current verification results look reasonable, further subjective and objective verification is carried out.

Reference

Doms, G. and U. Schättler, 2002: A description of the nonhydrostatic regional model LM. Part I: Dynamics and Numerics. *Deutscher Wetterdienst*, Offenbach, 134 pp. (Available at: www.cosmo-model.org).

Line-shaped Convective Band Developed Over the Osaka Plain

Hiromu SEKO[*1], Yoshimasa, KUMAHARA[2], Kazuo SAITO[1]
[1] Meteorological Research Institute, Japan Meteorological Agency, Tsukuba, Japan
[2] Osaka District Meteorological Observatory, Japan Meteorological Agency, Osaka, Japan

1. Introduction

Heavy rainfalls are often caused by line-shaped bands when the moving speed of the bands is slow. Therefore, the study on the structure and evolution of the line-shaped bands is important for the disaster prevention.

The line-shaped band, which is referred to as 'Yodogawa-Channel' (YC), frequently occurs over the Osaka plain. Although the line-shaped bands at Kyushu and Sea of Japan have been investigated by using the Radar data and outputs of the numerical model, the structure and evolution of the YC was not fully investigated so far. In this study, the precipitation distribution is compared with the observed one, and then the structure and moving speed of the band is investigated using the outputs of the numerical models.

2. Evolution of the line-shaped band

Left panels of fig. 1 show the precipitation distributions observed by conventional radars. On 4 April 2003, the low pressure was located at the Sea of Japan and the cold front extended southward from the low pressure (not shown). The large precipitation area **A** extended from north-northeast to south-southwest in fig. 1 was associated with the cold front. Along **A**, the southerly flow from the south of the band was converged with the southwesterly flow from the west (not shown). After the precipitation band **A** moved eastward, the short convective band **B**, which is 'Yodogawa-Channel' band, was generated at 12JST (Japan Standard tome, 9JST corresponds to 0UTC). This convective band **B** stayed until 14JST, and then began to decay and bend southeastward. Another convective band **C** was generated on the west of **B** at 12JST. The band **C** was generated on the convergence line of aforementioned southwesterly flow and westerly flow on the west of **C**. The surface temperature behind **B** was cold, while the temperature between **A** and **C** was similar to that on the east of **A** (not shown). The local low- and high-pressures were observed at front of and in the intense precipitation regions in **A** (not shown).

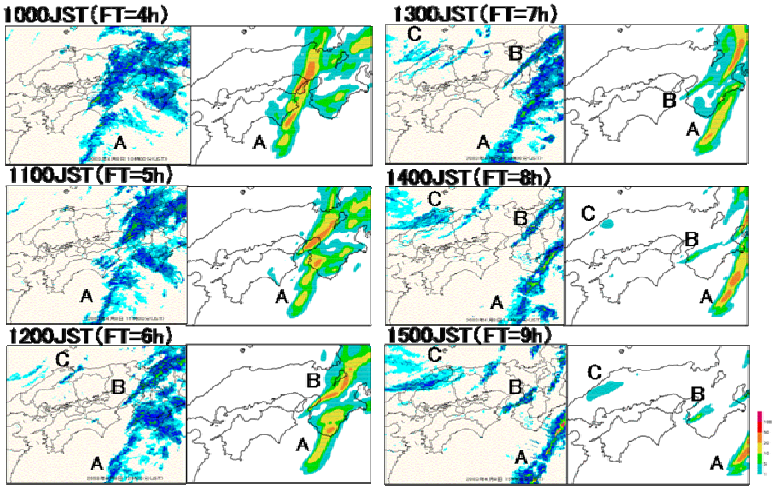

Fig.1 Observed precipitation regions from 10JST to 15JST on 8 April, 2003 and the precipitation simulated by JMANHM.

These convective bands were simulated by JMANHM (Saito et al, 2001) with the horizontal grid interval of 5 km. The simulated distribution of the precipitation was similar to the observed one, although the bending of the band **B** was earlier and **C** was weaker (right panels of fig. 1). Because the aforementioned features of the temperature and pressure distribution were also well reproduced (not shown), the structure of the convective band is explained in the next section.

3. Structure of the YC band

The convective band was simulated by JMANHM with a grid interval of 2 km. The initial and boundary data were produced by spatial and temporal interpolations. The evolution of the convective band **B** from 1150JST to 1310JST and the 3-dimensional structure at 1230JST are shown in figs. 2 and 3, respectively. The line-shaped band was bended southeastward at 1230JST, and then split into the southern part (**BS**) and northern part (**BN**) at 1310JST. The reason of the difference of the speed is explained in the section 4.

Along **BS**, the low-level southerly flow between **A** and **BS** was warm and humid (figs. 3a and 3c). This low-level inflow was converged with the westerly flow and ascended (fig. 3d). The westerly flow originated from the Sea of Setonai-kai on the west of **B** (fig.2). This westerly flow also intruded into the eastern edge of **BN** and lifted up the southerly flow on the east of **A** (fig. 3d). The temperature under **BN** was cold, because of the evaporation of the rain water (fig. 3c). In front of **BN**, a low pressure area existed (fig. 3e). Because the low pressure area moved with **BN**, this low-pressure is deduced to be produced by the release of the latent heat at the middle level. On the other hand, a high pressure area was produced in the precipitation area **BN** due to the evaporation of the rain water. At the height of 3 km, southwesterly flow, whose direction was parallel to the band, was dominant (fig. 3b). It is noted that there were no large descending areas near the band (fig. 2d). Namely, the

[*] hseko@mri-jma.go.jp, phone +81-29-853-8640; fax +81-29-853-8649

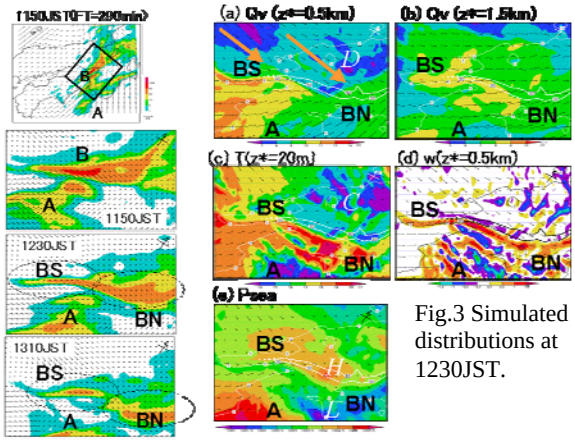

Fig.2 Simulated precipitation at 1150-1310JST.

Fig.3 Simulated distributions at 1230JST.

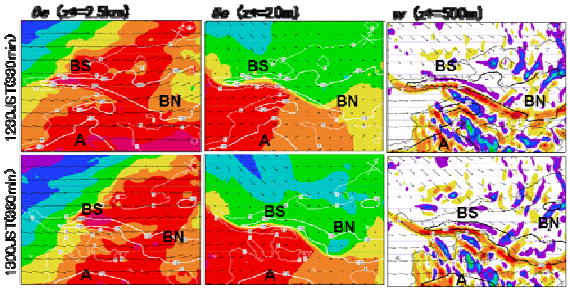

Fig.4 θe and vertical velocity distribution at 1230JST and 1300JST. Counter lines indicates the precipitation regions.

surface cold pool was generated by the low-level westerly flow and the mechanism that the middle-level dry air enhances convection did not work in this case. These features indicate that this band was back-and-side-building type (Seko and Nakamura, 2002).

4. Development of decay of the YC band

Next, the development and decay of **B** is explained. As mentioned before, the southerly flow between **A** and **B** generated **B**. When the time variation of wind speed of southerly flow was monitored, the wind speed was increased due to the low-pressure at the front of the intense precipitation region, and then decreased after **B** was generated (not shown). The convective band **B** did not increase the wind speed of the southerly flow. Therefore, the monitoring of the southerly flow before the generation of **B** is important for the prediction of YC band. Figure 4 shows the equivalent potential temperature (θe) distribution when the band **B** was decaying. At 1300JST, the low-θe air expanded over the southern tip of **B** (right panels in fig. 3) and the updraft there was weakened, although the southerly inflow changed slightly. This evolution indicates that the middle-level dry air weakened the convective band **B**.

4. Moving speed of YC band

As mentioned in section 2, the moving speed of **BN** was faster than that of **BS**. In this section, the difference of the moving speeds is discussed. Firstly, the surface horizontal wind and pressure within the rectangle in fig.5 were averaged, and then averaged value was substituted into eq.(2),

$$-(v-V)\frac{\partial(v-V)}{\partial y}-\frac{1}{\rho}\frac{\partial p}{\partial y}+F_y=\frac{\partial v}{\partial t}\ (=0:\ assumption)\quad (1),\qquad \int_a^b F_y dy=\tfrac{1}{2}v^2\Big|_a^b-V v\Big|_a^b+\frac{1}{\rho}p\Big|_a^b\quad (2),\qquad V=\left(\frac{1}{2}v^2\Big|_a^b+\frac{1}{\rho}p\Big|_a^b-\int_a^b F_y dy\right)\Big/v\Big|_a^b\quad (3)$$

where V is the moving speed of the band and F is the residual terms. It is expected that F was composed of the friction and Colrolis force terms; the function of the wind velocity. Thus, F was estimated as a function of horizontal wind velocity and substituted to (3). Because the estimated speed was roughly close to the simulated one (fig. 7), the contributions of the advection term, pressure gradient force term and residual term were plotted in fig. 8. In **BN**, the pressure gradient force moved the band eastward and other terms disturbed the movement. On the contrary in **BS**, F moved the band eastward.

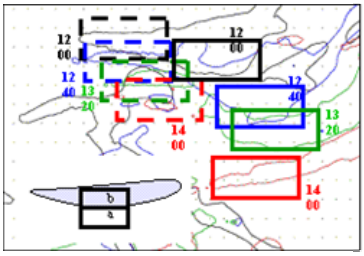

Fig. 6 Movement of the northern and southern parts of the line-shaped band.

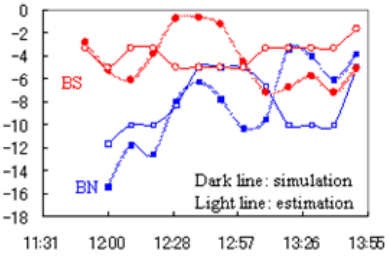

Fig.7 Simulated and estimated moving speed of the northern and southern parts of the line-shaped band.

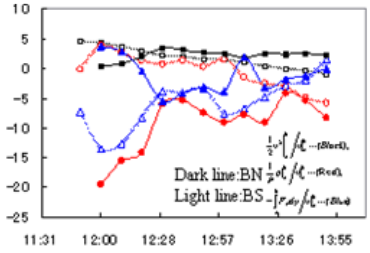

Fig. 8 Contributions of advection, pressure gradient and other terms on the moving speed of the line-shaped band.

References

Saito, K. T. Kato, H. Eito, and C. Muroi, 2001: Documentation of the Meteorological Research Institute/Numerical Prediction Division Unified Nonhydrostatic Model. *Tech, Rep. of the MRI*, **42**, p133.

Seko, H., and H. Nakamura, 2002: Numerical study of the shape and maintenance mechanisms of meso-β scale line shaped precipitation system in the middle-latitude, *CAS/JSC WGNE Research Activities in Atmospheric and Oceanic Models*,**33**,5-30.

Stochastic and Deterministic Component in Limited Area Model Downscaling

Leo Separovic, Ramon de Elia* and René Laprise
Département des Sciences de la Terre et de l'Atmosphère, Université du Quebec à Montréal
and *Consortium Ouranos

1. Introduction

Limited Area Models (LAMs) have been shown capable to create small-scale features despite the fact of being nested and initialized with coarse resolution Global Circulation Models (GCM) or global analyses. Based on an ensemble of LAM integrations, which differ only in atmospheric and land-surface Initial Conditions (IC), it has been shown that simulations generated by the same set of Lateral Boundary Conditions (LBC) stay partially correlated, regardless of the integration time, unlike the case for global models. The scale analysis of mean square difference between members of an ensemble, performed by de Elia et al. (2002), suggests that the correlation asymptotes to values greater or equal than zero, varying with length scale. For small scales, the asymptotic value is close to zero, while for large scales, driven by LBC, the asymptotic value is close to 1.

In this context, the ability of LAMs to serve as 'intelligent' interpolators of the driving fields is determined by the LAM's capacity to provide not only meaningful information regarding small-scale structures, but, also, that this information be independent of small perturbations in IC. In this study we perform a scale analysis of the ensemble mean of an ensemble of LAM simulations. We will consider the ensemble average as the part of the LAM's solution that is insensitive to small perturbations in IC and thus determined only by LBC. As this part is not affected by internal variability it will be thought of as a deterministic component. The part dependent on IC will be thought of as a stochastic component.

2. Experimental Set-up

The Canadian Regional Climate Model (CRCM), described by Caya & Laprise, (1999) - with 45km horizontal grid spacing (true at 60°N), 18 levels in the vertical, 120x120 domain, centered over Montréal, Canada - was employed to produce 20 three-month simulations for June, July & August 1993 (for further details see Alexandru et al., 2006). The CRCM was nested within regridded coarse (T62) NCEP reanalyses, with updating frequency of 1 per 6hrs. All 20 simulations were generated using identical LBC and ocean surface, differing only in the IC used for the atmospheric and land-surface fields. Each simulation was initialized with a 24hrs time lag, the first one starting on the 1st May 1993 at 00GMT, and the last one on the 20th May at 00GMT – allowing at least 10 days spin-up to assure that internal variability is fully developed during the period of interest. The nesting technique employed here was derived from that proposed by Davis (1977). The domain size was chosen to be neither too small, which could disable small-scale creation (Leduc and Laprise, 2006), nor too large, which could significantly deviate large scales from driving fields (Miguez-Macho et al, 2004). No large-scale nudging was applied.

The 2D spectral variances for selected pressure levels were calculated using Discrete Cosine Transform (DCT), firstly employed for NWP purposes by Denis et al. (2002). The variances were then binned into specific bands of 2D wave number intensity, and, thus, expressed as simple functions of 1D spatial scale.

3. Methodology and Results

Let $\vartheta(\psi_m)$ be the 1D spectral variance of a field ψ_m defined on the LAM grid, where $1 \le m \le M$ denotes the member of the ensemble, and let [ ] denotes the ensemble average over all M simulations. We define the average spectral variance, V, as a mean of M spectral variances computed for each of the members of the ensemble. Thus, we can write:

$$V(k,p,t) \equiv \left[\vartheta(\psi)\right]. \qquad (1)$$

The spectral variance of the ensemble mean is given by

$$V_{ENS}(k,p,t) \equiv \vartheta\left(\left[\psi\right]\right), \qquad (2)$$

and, finally, the spectral variance of regridded NCEP reanalyses by

$$V_{OBS}(k,p,t) \equiv \vartheta\left(\psi_{OBS}\right). \qquad (3)$$

Here k represents the 1D wave number, p is the pressure level, and t is integration time. If, at any length scale, individual runs have no spread among them, then the variances given by (1) and (2) become identical. Furthermore, at large-scales, where no spread is expected to appear, any difference between variances (2) and (3) is undesirable, because it indicates that the LAM does not simulate the observed amount of variance. On the contrary, at small-scales, the positive difference between V_{ENS} and V_{OBS} implies that the downscaled information contains a deterministic part. In particular, for small scales, unresolved by the driving fields, a difference between

variances (1) and (2) indicates the stochastic part of the downscaled variance, while a difference between variances (2) and (3) indicates the component independent of IC.

The variances given by equations (1), (2), and (3), for geopotential at 925hPa, sampled every 6 hrs and averaged over 3 summer months of 1993 are shown in Figure 1. It can be seen that for the largest resolved scales there is a slight excess of variance in both the individual runs and their ensemble average relative to the reanalyses. We notice that this excess was detected only under the 600hPa-level; in the upper part of the troposphere we found a slight lack of variance at those scales (not shown). For wave numbers larger then 5 (~1100km) - the effective resolution of reanalyses - the variance of reanalyses should be equal zero as those scales are not represented in the driving fields. Due to the regridding noise and Gibbs effect of the DCT this is not the case. A difference between V and V_{ENS} appears for wave numbers larger then 10 (~500km), as a consequence of spread among the runs. Furthermore, V_{ENS} has a noticeably higher value then V_{OBS}, for all wave numbers larger then 5, implying that a part of the downscaled variance is due to small-scale structures common to all members of the ensemble. It is worth noting that similar behaviour was found at all levels, with a decrease of difference between V_{ENS} and V_{OBS} with height, (not shown).

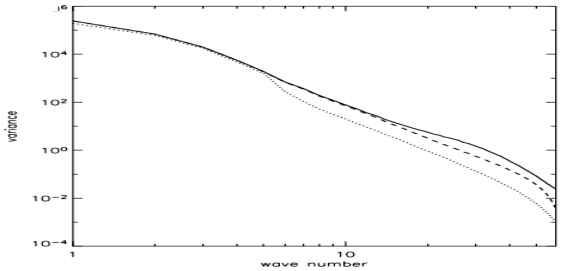

FIG. 1. Spectral variance of geopotential at 925hPa: *full line* - average spectral variance of individual runs, equation (1); *dashed line* - spectral variance of ensemble mean, equation (2); *dotted line* - spectral variance of reanalyses, equation (3). The variances were sampled every 6 hours and the sample mean for 3-month long period is presented.

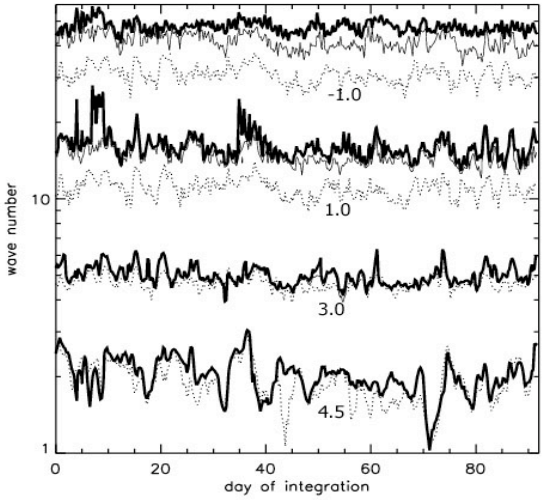

FIG. 2. Logarithm of spectral variance of geopotential field at 925hPa: *full thick line* - average spectral variance of individual run, equation (1); *full thin line* - spectral variance of ensemble mean, equation (2); *thin dotted line* - spectral variance of reanalyses, equation (3). Isolines are drawn for four different values: -1.0, 1.0, 3.0, and 4.5.

The scale distribution of the temporal evolution of variances given by equations (1), (2), and (3) is shown in Figure 2. It can be seen that, for the largest resolved scales of thousands of kms (isolines of 4.5), the excess of the simulated variance relative to the reanalyses is not systematic but intermittent during periods of few days, thus contributing to the temporal mean in Figure 1. The isolines of −1.0 and 1.0, which represent the behaviour of non-driven small-scales, show that the difference between V_{ENS} and V_{OBS} is present at all times. On the contrary, the difference between V and V_{ENS} exhibits more complicated behaviour, indicating that the intensity of spread pulsates according to weather pattern. We notice that the isolines of 3.0 exhibit little spread, except around day 48, when the internal variability seems to penetrate inside driven scales. This is clearly visible on the geopotential maps of that day.

4. Conclusion

Our results suggest that the downscaled information provided by the CRCM is partially determined by the boundary conditions and partially of stochastic nature (dependent on small, uncontrollable changes in IC). Hence, the value added by dynamical downscaling has to be sought in both components. It is worth noting that the deterministic component is stronger near the surface. The results also show that the large-scale information is sometimes modified inside the domain, and that this tends to happen in all individual runs in the same manner. This seems to suggest that the CRCM is unable to reproduce some of the large-scale weather patterns provided at the boundaries.

References:

Alexandru A., R. de Elia, and R. Laprise, 2006, Geographical distribution of internal variability in regional downscaling, the same volume.

Caya D., and R. Laprise, 1999, A semi-implicit semi-Lagrangian regional climate model: The Canadian RCM, *Mon.Wea.Rev.,* 127, 341-362.

Davies, H.C., and R.E. Turner, 1977, Updating prediction model by dynamical relaxation: An examination of the technique, *Quart.J. Roy.Meteor.Soc.,* 103,225-245.

De Elia R., and R. Laprise, 2002, Forecasting skill limits od nested, LAMs: A perfect model approach, *Mon.Wea.Rev*., 130, 2006-2023.

Denis B., J. Côté, and R. Laprise, 2002a, Spectral decomposition of two-dimensional fields on limited-area domains using the discrete cosine transform, *Mon.Wea.Rev.,* 130, 1812-1829.

Leduc M. and R.Laprise, 2006, CRCM sensitivity to domain size, the same volume.

Miguez-Macho G., G.L. Stenchikov, and A. Robock, 2004, Spectral nudging to eliminate the effects of omain position geometry in regional climate model simulations, *J.Geophys.Res.,* 109, D13104, doi: 10.1029 /2003JD004495

Atmospheric boundary layer modelling in the numerical prediction operations.

Shnaydman V.A.
State New Jersey University-Rutgers, USA, volf@envsci.rutgers.edu,
Berkovich L. V.
Hydrometeorological Research Center of Russia, berkovich@mecom.ru.

The basic conception of Hydrometeorological Research Center of Russia system for operational short-range forecasting is the reconstruction of the synoptic-scale and mesoscale weather patterns from the output product of a large-scale prediction scheme including Atmospheric Boundary Layer model and parameterization procedures./Berkovich, Tarnopolskii, Shnaydman, 1997/The results of the reconstruction of atmospheric boundary layer (ABL) internal structure from objective analysis and forecast data demonstrated the possibility of using the ABL model in operational prediction of meteorological fields and weather phenomena. Simultaneously these results showed the necessity of the improvement of the quantitative description of ABL turbulence structure. The improved model /Shnaydman,2004/ is applied for the reconstruction of the internal ABL structure for the Ukraine and European part of Russia in numerical operations. Here the turbulence parameters under different meteorological conditions obtained are given. The turbulent fluxes of the sensible heat changed from –30 to +45 Wt/m2, when the stratification varied from stable to unstable conditions. The friction velocity had mean values of 0.2-0.5m/s but get more than 1.0m/s near the areas of large roughness and the surface geostrophic wind reached 15m/s and more. The ABL heights have a substantial space and temporal variability from 100 to 1000m on average. But when the thermal stratification is unstable and the geostrophic wind on the level of 850hPa is larger than 20m/s the ABL top became 2000m and more. The vertical distribution of TKE depended on the stratification. TKE maximum was located near the surface when the stable or neutral stratification was observed. In this case TKE values were 0.4-0.6 m2/s2 when the surface geostrophic wind was less than 10m/s and the roughness was 10-20cm. The greater values of these parameters created TKE of 0.5-1.2 m2/s2. The unstable stratification led to shift TKE maximum to the levels 100-300m and the values got 0.8-2,3 m2/s. The vertical coefficient of the turbulence increased from the near-surface level reached the maximum on the heights of 50-300m and then decreased to the ABL top. The maximum of Kz changed in the wide limits from 1-56m2/s. depended on the combination of geostrophic wind, stratification, baroclinity and roughness.
As the example of the application of the developed model to the another areas of the North hemisphere the results of calculations are given for USA and Canada (20-55N,70-125W).At first it's necessary to underline that the area considered distinguishes itself by the complex topography, the high mountains on the west, flat surface in the center and the elevations on the east. Another peculiarity of the calculation domain is the oceans at the west and east bounds. The internal ABL structure was reconstructed from operational objective analysis for 00:00 UTC April 12,2005 and forecast data for 36-hour prediction period. The ABL internal structure was represented by horizontal distribution and temporal dynamics of meteorological variables and turbulence parameters on 21 levels from 10m to

2000m. We focused on analysis of horizontal distribution and temporal dynamics of the ABL turbulence parameters and organized vertical motions. Analysis of the spatial distribution of vertical turbulence coefficient (Kz) showed that Kz were less than 1.0 m2/s near surface and increased to 1-15 m2/s at the top of surface layer (about 50m). Kz were largest between the levels from 50m to 250m with the maxims near the level 100m.At this level Kz changed from 3 m2/s to 25 m2/s with pronounced areas of Kz>15 m2/s in the center and northwest corner of the domain. In the rest of territory Kz was 1-6 m2/s. Above 250m the values Kz decreased sharply and the small areas of Kz reached 17 m2/s were located in the west and east bounds at the level 500m and 5 m2/s at the level 1000m. The similar features of the temporal dynamics was traced at all levels inside ABL. The analysis of Kz temporal changes at the level 100m. showed that Kz from 7 m2/s to 28 m2/s maintained during the whole prediction period in the east part of the domain. But regions with Kz>=20 m2/s were attracted to the east and west oceanic coasts, essentially larger in the daily hours and moved towards south. In these regions the intensive vertical turbulent exchange spread to the levels 500-1000m.The horizontal distribution of TKE is characterized by zonal elongated area of largest TKE between 30N and 55N. Three vertical sublayers distinguished in this area: near- surface (below 50m), middle (50-250m) and upper (above 250m). In surface sublayer TKE range is formed from 0.5m2/s2 to 2.5m2/s2. In middle one TKE range increased to 3.0 m2/s2and in the upper sublayer TKE maximum was less than 0.5m2/s2. Beyond the area of TKE maximums made amount to 0.5m2/s2 below 200m and 0.1 m2/s2 above this level. As whole TKE temporal dynamics manifested itself the trend of TKE reduction during the given period. But larger TKE are obtained in daily hours in comparison of the night ones. The largest dissipation rates are concentrated in the surface layer. Here the dissipation rates were 0.3-5.5 m2/s3. Above the surface layer the dissipation rates were less 1 m2/s3.

The space distribution and the temporal dynamics of organized vertical motions are the integral evaluation of the influence of main forcing and interaction physical mechanisms on the ABL structure formation. The interaction between the space-temporal dynamics of the pressure and turbulent exchange led to the creation of actual wind deviation from the geostrophyc speed vector. As it came next from the continuity equation the non geostrophyc deviation promoted to organize the upward and downward currents in low and high pressure areas correspondingly. In accordance with the distribution of the pressure, intensity of the turbulence and the topography the areas the vertical flows at the ABL top are traced from east to west in following order: downward-upward-downward-upward. The first two areas of organized vertical motion made conditional upon the distribution of the pressure and intensity of turbulence. In these areas the module of the vertical speed got 0.8-1.2 cm/s. Te effect of topography played a large contribution of the next two areas of the vertical motions which reached the module values of 0.5-0.8 cm/s. The temporal dynamics of organized vertical motions at the ABL top reflected the tendency of the forcing mechanism evolution. The intensity of downward and upward currents decreased during the prediction period.

Using the model output information of the spatial distribution of the meteorological variables and turbulence characteristics can improve the existing methods of prediction of the clouds and precipitation, air pollution quantitative description.

Berkovich, L.V., Tarnopolskii, A.G., Shnaydman, V.A.: 1997, " Hydrodynamic Model of the Atmospheric and Oceanic Boundary Layers" Russian Meteorology and Hydrology 7, 30-40

.Shnaydman V.A.:2004,“ Improved hydrodynamical scheme of the turbulence description “ Research Activity in Atmospheric and Oceanic Modeling, No 34, 4.29 – 4.30.

Using dynamical downscaling to close the gap between global change scenarios and local permafrost dynamics

M. Stendel[1] (mas@dmi.dk), V.E. Romanovsky[2], J.H. Christensen[1] and T. Sazonova[2]
[1] Danish Meteorological Institute, Copenhagen, Denmark
[2] Geophysical Institute, University of Fairbanks, Alaska, USA

Even though we can estimate the zonation of present-day permafrost from deep-soil temperatures obtained from global coupled atmosphere-ocean general circulation models (GCMs) by accounting for heat conduction in the frozen soil, it is impossible to explicitly resolve soil properties, vegetation cover and ice contents in great details due to the coarse resolution of contemporary GCMs that prevents a realistic description of soil characteristics, vegetation, and topography within a model grid box. On the local scale, descriptions of the heterogeneous soil structure in the Arctic exist, but only for limited areas. We propose to narrow the gap between typical GCMs on one hand and local permafrost models on the other by introducing as an intermediate step a high resolution regional climate model (RCM) to downscale surface climate characteristics to a scale comparable to that of a detailed permafrost model. This results in a considerably more realistic depiction of present-day mean annual ground temperature and active layer depth, in particular in mountainous regions (Stendel et al., 2006). By using global climate change scenarios as driving fields, one can obtain permafrost dynamics in high temporal resolution on the order of years. For the 21st century (scenarios A2 and B2), we find an increase of mean annual ground temperature by up to 6 K and of active layer depth by up to 2 m within the East Siberian transect. According to these simulations, a significant part of the transect will suffer from permafrost degradation by the end of the century.

Many permafrost models are based on the concept of a ‘surface frost index’ or ‘deep soil frost index’ (Stendel and Christensen, 2002) even though at least surface temperatures are not directly related to permafrost properties. One can circumvent complications associated with the explicit parameterisation of snow cover, but such an approach needs information about soil properties, vegetation and snow cover which hardly are realistic on a typical GCM grid. One possibility to overcome resolution-related problems is by means of downscaling to use a regional climate model (RCM). Instead of calculating a frost index from RCM data, we use the RCM to create boundary conditions for a sophisticated permafrost model. Our approach is novel in that the spatial resolution of the RCM and the permafrost model is comparable (0.5°), so that output from the RCM can be directly used to force the permafrost model. Furthermore, problems with soil, vegetation and snow properties can be overcome, as we can either pass information to the permafrost model from RCM output, or information from digitised Geographic Information Systems (GIS), where available, can be used to create forcing fields for the permafrost model. While downscaling procedures are a well established tool, no attempts have been undertaken so far to use dynamical downscaling in permafrost modelling.

As the driving AOGCM, we have chosen the state-of-the-art coupled ocean-atmosphere model ECHAM4-OPYC3. The RCM we have used is HIRHAM4 (Christensen et al., 1998), which can be thought of as a high resolution limited area version of ECHAM4. As the final step for regional permafrost modeling we have used the GIPL model (Geophysical Institute Permafrost Lab) of the University of Alaska Fairbanks (Sazonova and Romanovsky, 2003). The model is a quasi-two-dimensional, quasi-transitional, spatially distributed, physically

based analytical model for the calculation of active layer thickness (ALT) and mean annual ground temperature at the permafrost table (MAGT) and uses the so-called modified Kudryavtsev's approach which is based on the theory of wave propagation in a medium with phase transitions. The input data are mean annual air temperature and its seasonal amplitude (calculated from monthly means), average winter snow depth and density, composition, water content and thermal properties of soils and characteristics of vegetation cover and geomorphologic features.

According to the GCM scenario simulations, an increase of 2m air temperature of 8 to 11 K for scenario A2 and 6 to 9 K for scenario B2 can be expected for the Russian Arctic, with a corresponding increase in mean annual ground temperature by 2 to 6 K. According to the GIPL simulations, the mean annual temperature at the bottom of the active layer will rise above the freezing point in roughly a third of the area of the East Siberian transect by the end of the 21st century. Accordingly, widespread permafrost degradation (Fig. 1) and an increase in active layer depth on the order of 0.5 to 2 m are simulated.

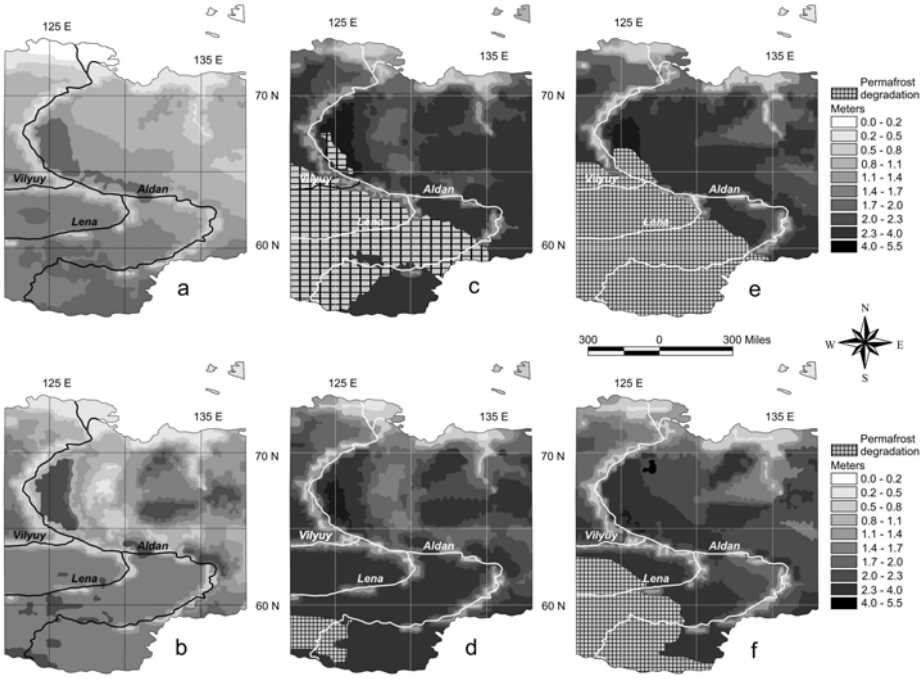

Fig. 1: Temporal evolution of ALT [m] (a) GIPL forced with observed climate data, (b) GIPL forced with HIRHAM control run, (c) GIPL forced with HIRHAM, scenario A2, average 2071-2100, (d) as (c), for scenario B2, (e) and (f) as (c) and (d), for ECHAM. Dark hatched areas denote permafrost degradation.

References

Christensen, O.B. et al., 1998: *J. Clim.* **11**, 3204–3229.
Sazonova, T.S. and Romanovsky, V.E., 2003: *Permafrost Periglacial Processes* **14**, 125-139.
Stefan, J., 1891: *Ann. Phys*. **42**, 269-286.
Stendel, M. and Christensen, J.H., 2002: *Geophys. Res. Lett.* **29**, doi: 10.1029/2001GL014345.
Stendel, M. et al., 2006: *Glob. Plan. Change* (submitted).

Investigation of QPF Produced by LM-z, the Z-Coordinate Version of the Non-Hydrostatic Model LM

J. Steppeler*, H. W. Bitzer**, Z. Janjic***, U. Schättler*, L. Torrisi****, U. Gjertsen*****, E. Avgoustoglou*******, P. Prohl*, J. Parfinievicz******, U.Damrath*

*DWD, **AW Geophys, ***NCEP,**** CNMCA, *****met.no, ******IMGW, *******HNMS
juergen.Steppeler@dwd.de

1. Introduction

Improvements of Quantitative Precipitation Forecasts (QPF) achieved by the non-hydrostatic model LM-z were investigated. LM-z (see Steppeler et al. 2002b for the 2-d version) is the z-co-ordinate version of the non-hydrostatic model LM (Steppeler et al., 2002a). The numerical approach used in LM-z differs from that of Mesinger et al. (1988) by correcting a numerical error which has been pointed out by Gallus and Klemp (2000).

A total of 39 forecasts using LM-z in different model configurations were done to investigate the precipitation forecast. For each of these model runs LM-z produced better precipitation forecasts than LM, which differs from LM-z only by the use of the terrain following co-ordinate. Fig. 1 (top) gives the threat scores for 29 cases using a model area covering most of Europe with a resolution of 7 km. The 6 hr precipitation sums in 6 hr intervals are given in Fig. 1, bottom. The precipitation verifies much better for LM-z. There is a smoother movement of the frontal rain band and a better representation of the convective rain associated with the cold front, in particular for the time interval 12hr-6hr.

Vector wind verification against radiosondes of the 24 hr forecast shows also a considerable improvement with LM-z, as shown in Fig. 1, top right.

REFERENCES.

Gallus, W., and J. Klemp, 2000: Behavior of flow over step orography. Mon. Wea. Rev., 128, 1153-1164.

Mesinger, F., Z. Janjic, S. Nicovic, D. Gavrilov and D. Deaven, 1988: The step-mountain coordinate: Model description and performance for cases of Alpine lee cyclogenesis and for a case of Appalachian redevelopment. Mon. Wea. Rev. 116, 1493-1518.

Steppeler,J., G. Doms, U. Schättler, H.W. Bitzer, A. Gassmann, U. Damrath and G. Gregoric, 2002a: Meso gamma scale forecasts by nonhydrostatic model LM. Meteor. Atmos. Phys., 82, 75-96.

Steppeler,J., H.W. Bitzer, M. Minotte, L. Bonaventura, 2002b: Nonhydrostatic atmospheric modelling using a z-coordinate representation. Mon. Wea. Rev. 130, 2143-2149.

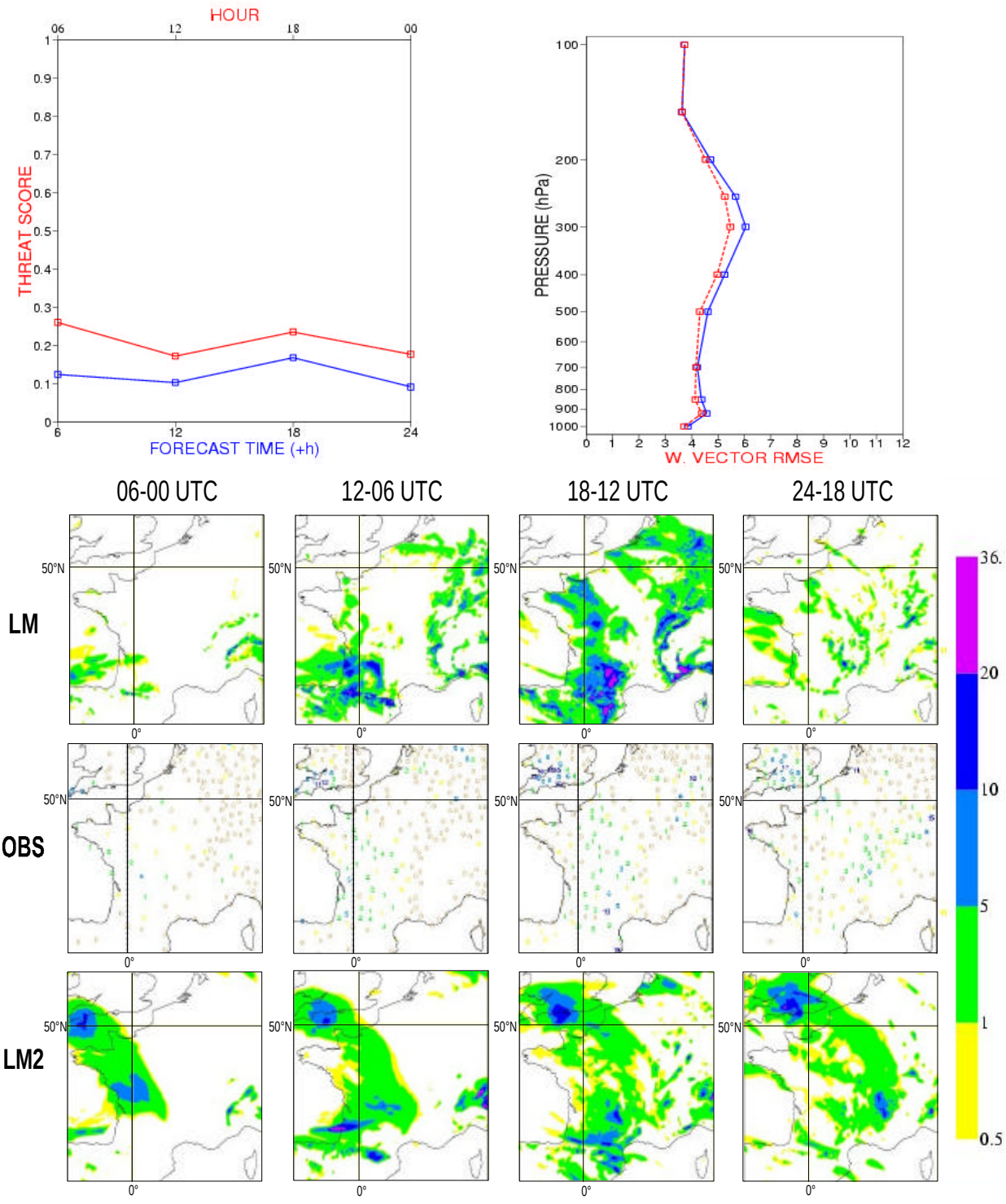

Fig 1 top left: Threat score for QPF amount 2mm/6hr for 29 cases 24 April to 22 May 2005 for LM-z (red) and LM (blue); top right: as top left, for vector wind verification against radiosondes;

bottom: 6hr accumulated precipitation for different times of a 24 hr forecast from 29 March 2005 by LM and LM-z and corresponding SYNOP observations

Progress of the limited area NWP forecasts at DMI

Xiaohua Yang (Xiaohua@dmi.dk) and Bent Hansen Sass (bhs@dmi.dk)
Danish Meteorological Institute (DMI)

DMI's operational NWP system consists of a main forecast model with a grid-spacing of 0.15 degree and 40 vertical levels. The model domain covers an extensive area of northern hemisphere (see the figure to the left). The model is run 4 times a day with 60 h lead time. In addition, two nested high resolution model runs with 0.05 degree grid-spacing, centered around Greenland and Danish territories, respectively, are performed for up to 54 h forecasts. The NWP system (DMI-HIRLAM) used in DMI's operational suite is based on the HIRLAM forecast system. HIRLAM, High Resolution Limited Area Model, is a 9-nation European research cooperation project started in 1985.

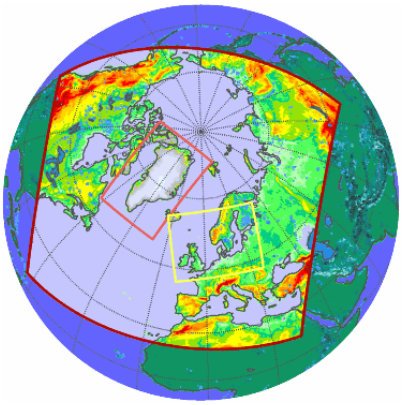

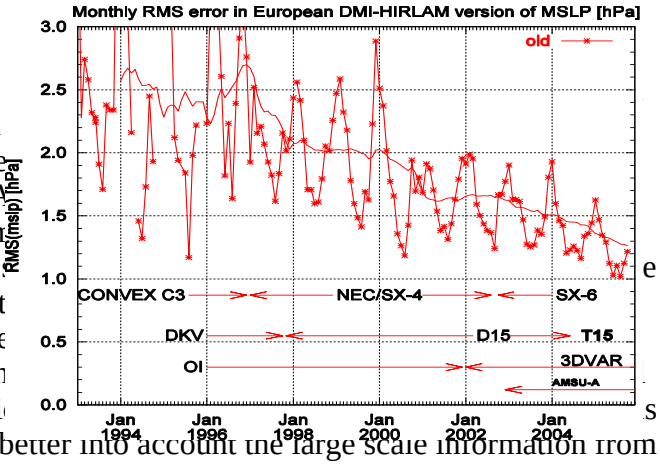

Substantial progress in short-range e
the last decade, both in terms of an
events, and in daily forecasts of the
the forecast quality in DMI-HIRLA
which the monthly averaged root-n
forecasts during the past decade is
forecast skill. Observation verificat
forecast skill of up to 48 h for scree
global model (such as ECMWF) an
model upgrades were made, in whi s
been improved with a goal to take better into account the large scale information from the global model. The DMI-HIRLAM assimilation modules have been extended to assimilate Meteosat-8 AMV wind and Ocean Sea-ice SAF data for SST. Tuning of physical parameterizations and of the background error structure function in 3D-VAR analysis contributes significantly to the overall improvement of the model skills. During 2005, the resolution of the model for Greenland area has been increased to 0.05 degree spacing, which has been appreciated greatly by duty forecasters at DMI.

Work is in progress to start pre-operational test of a NWP system based on 4D-VAR. Research and pre-operational activities have also been intensified in the area of meso-

scale forecasts. During 2005, near-real time nonhydrostatic meso-scale forecasts have been started at DMI with a horizontal grid-spacing of 0.025 degree. The efforts in the meso-scale modeling is carried out through code collaboration between HIRLAM and ALADIN consortia. The physical parameterizations developed in the HIRLAM project have recently been ported to the non-hydrostatic model environment and will be tested in daily runs for areas of interest including Denmark and selected parts of Greenland.

References:
DMI Technical reports 05-10, 05-15.
[Available from DMI]

Simulation of a Polar Low Case in the North Atlantic with different regional numerical models

Matthias Zahn, Hans von Storch
University of Hamburg/ GKSS, Matthias.Zahn@gkss.de

ABSTRACT
In this paper it is shown that regional scale models are able to simulate maritime mesoscale features in general, but there is space for improvement in detail.

INTRODUCTION
From the 14th until the 16th of October 1993 an intense mesoscale cyclone occurred in the North Atlantic fulfilling the requirements of being classified as Polar Low according to Rasmussen and Turner (2003). During its lifetime it moved southward from its developing area in the Norwegian Sea on a track approximately parallel to the Norwegian coastline passing the Shetland Islands and hitting the Norwegian coast in the south on the 16th of October (Nielsen, 1997). In this study the ability of two different numerical regional atmospheric models (grid size about 50 km $\times$ 50 km) to reproduce this Polar Low occurrence was investigated and compared to observational analyses.

DATA
The data used in this study originate from extended simulations with the regional atmospheric model REMO (REgional MOdel) and CLM (CLimate Model) simulations performed at the GKSS with spectral nudging (Feser et al., 2001) and driven by NCEP/NCAR reanalyses data (Kalnay et al., 1996) at the boundaries. Two analyses have been used to evaluate the performance of the two models – the EM3AN analysis prepared by the DWD (German Weather Service) by means of their forecast model HRM (High Resolution Model) and another analysis that has been constructed by the FU Berlin and is commonly known as „Berliner Wetterkarte“.

RESULTS
For comparison in this paper a point in time (Oct. 15th 1993, approx. 6.00 a.m.) is chosen when the Polar Low entered its mature state and output data from all sources is available (fig. 1). All of the figures show a depression in mean sea level pressure and high wind speeds (when vorticity $> 10^5 s^{-1}$) in the area the Polar Low is situated. Thus, the Polar Low is in principle generated correctly, but the simulations deviate with respect to location and depth of the depression. In the analyses and REMO the center of depression is located east of the zero degrees meridian, whereas CLM depicts the center farther west. In the „Berliner Wetterkarte“ sea level pressure falls below 985 hPa, the DWD analysis shows a decrease not exceeding 990 hPa and CLM and REMO not falling below 995 hPa. At this point it cannot be decided whether this is due to a systematic error in CLM or whether there is a lack of reliability in the analyses which are locally based mostly on the the data obtained at weather ship „M“ (as marked in fig. 1(d)). A satellite image taken only seven hours later (AVHRR, Oct. 15th 1993, 13.29 p.m., not shown) suggests a depression center slightly to the west of the meridian closer to the position depicted in CLM.

References

Feser, F., R. Weisse, and H. von Storch, 2001: Multi-decadal atmospheric modeling for Europe yields multi-purpose data. *Eos Transactions*, **82**, pp. 305, 310.

Kalnay, E., M. Kanamitsu, R. Kistler, W. Collins, D. Deaven, L. Gandin, M. Iredell, S. Saha, G. White, J. Woollen, Y. Zhu, M. Chelliah, W. Ebisuzaki, W. Higgins, J. Janowiak, K. Mo, C. Ropelewski, J. Wang, A. Leetmaa, R. Reynolds, R. Jenne, and D. Joseph, 1996: The NCEP/NCAR reanalysis project. *Bull. Am. Meteorol. Soc.*, **77**, 437–471.

Nielsen, N., 1997: An early Autumn polar low formation over the Norwegian Sea. *J. Geophys. Res.*, **102**, 13955–13973.

Rasmussen, E. and J. Turner, 2003: *Polar Lows: Mesoscale Weather Systems in the Polar Regions*. Cambridge University Press, Cambridge.

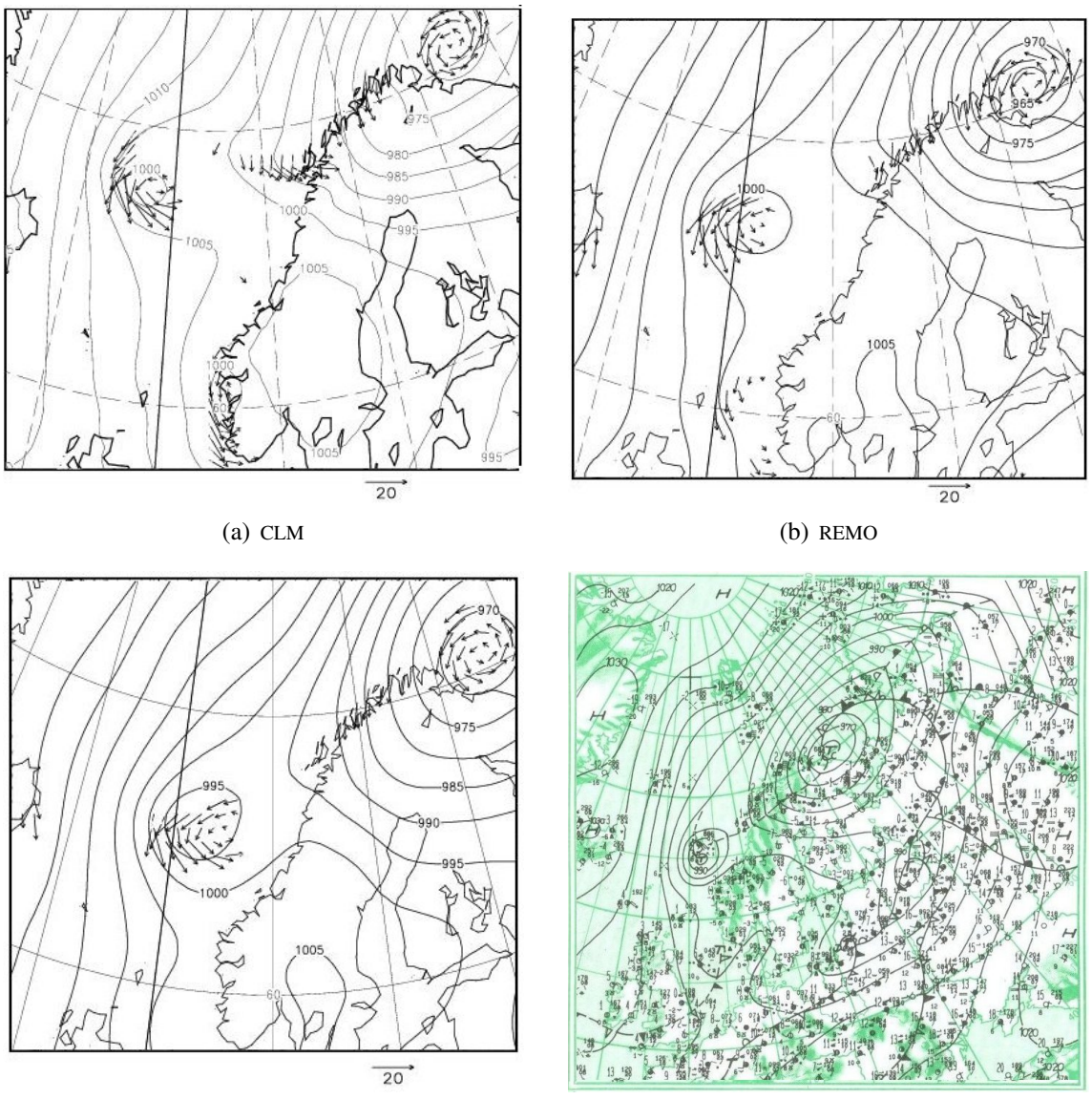

(a) CLM (b) REMO

(c) HRM, DWD (d) BWK

Figure 1: 1(a)- 1(c)10m wind velocity (length of arrows) in areas with an absolute value of relative vorticity $> 10^5 s^{-1}$ and mean sea level pressure from CLM and REMO simulations and HRM analysis, DWD, respectively, at 15/10/93, 6:00, 1(d) surface weather chart FU Berlin at 15/10/93, 7:00